Master's Thesis

# Optogenetic Dissection of Entorhinal-Hippocampal Space Circuit

Ignas Cerniauskas

Norwegian University of Science and Technology

Faculty of Medicine

Department of Laboratory Medicine, Children's and Women's Health

Master's Programme in Molecular Medicine

Supervisors:

Sheng-Jia Zhang

Jing Ye

Trondheim 2013

## ACKNOWLEDGEMENTS

This work was done at Kavli Institute for Systems Neuroscience and Centre for Neural Computation, Norwegian University of Science and Technology. I would like to acknowledge my principal supervisor Sheng-Jia Zhang, who always had time for my questions, inspired me to continue my academic pursuits in neuroscience, made things exciting, and gave me more than could be expected from any supervisor. I am also sincerely grateful to Jing Ye for "showing me the ropes" of *in vivo* electrophysiological recordings, always pointing out my mistakes and helping to correct them, never ending patience to answer all my inquiries, and invaluable suggestions and ideas during the writing period of my thesis. Thanks to Juan Wu for the help with the histology and our animal technicians – Grethe Jakobsen, Eirin Hårstad, and Merethe Andresen – for all their assistance when it comes to the wellbeing of the animals. And last but not least, my family and my girlfriend deserve a mention, because without them it would have been much more difficult to continue all of this.

# TABLE OF CONTENTS

## ABSTRACT

Spatial representation system of brain is comprised of place cells located in the hippocampus and grid cells, head-direction cells, and border cells found in the medial entorhinal cortex. There is a prominent circuitry between the hippocampus and the medial entorhinal cortex; however, exactly which entorhinal functional cell types project to hippocampus has not been determined yet. By injecting retrogradely transportable recombinant adeno-associated virus carrying channelrhodopsin-2 transgene in the hippocampus, optogenetic control over entorhinal neurons with direct projections to the hippocampus has been introduced. Using optogenetics together with electrophysiological recordings *in vivo* we were able to identify functionally defined hippocampus projecting entorhinal neurons as cell that responded with minimal latency to laser stimulations in the medial entorhinal cortex. A substantial portion of responsive cells were grid cells, but we also found other directionally or spatially modulated responsive cells, like head-direction and border cells, as well as principal unknown cells and interneurons. Our findings indicate that neural code transformation within the hippocampal-entorhinal circuit and generation of place fields may be achieved by combining broad spectrum of functionally defined inputs arising from medial entorhinal cortex.

# ABBREVATIONS

| | |
|---|---|
| AAV | Adeno-associated virus |
| AMPA | α-amino-3-hydroxy-5-methyl-4-isoxazole-propionic acid |
| AP-5 | D-2-amino-5-phosphonopentanoic acid |
| BGH | Bovine growth hormone |
| BSA | Bovine serum albumin |
| CA | *Cornu ammonis* |
| CaMKIIα | α-calcium/calmodulin-dependent protein kinase II |
| ChR | Channelrhodopsin |
| CNQX | Nitroquinoxaline-2,3-dione |
| DIO | Doublefloxed inverted open reading frame |
| EF-1α | Elongation factor 1-alpha |
| ER | Endoplasmic reticulum |
| GFAP | Glial fibrillary acidic protein |
| HR | Halorhodopsin |
| HSV | Herpes-simplex virus |
| ITR | Inverted terminal repeat |
| LEC | Lateral entorhinal cortex |
| LED | Light emitting diode |
| MEC | Medial entorhinal cortex |
| NGS | Natural goat serum |
| NMDA | *N*-methyl-D-aspartate |
| PBS | Phosphate buffered saline solution |
| SDC | Sodium dodecylcholate |
| SFO | Step function opsin |
| TRIS | Tris(hydroxymethyl)aminomethane |
| VGLUT2 | Vesicular glutamate transporter 2 |
| WPRE | Virus posttranscriptional regulatory element |

# 1. INTRODUCTION

The parahippocampal-hippocampal space network contains four distinctive cells types that play an essential role in shaping spatial representation in mammalian brain. In hippocampus place cells are located (*1*), whereas grid (*2*), head-direction (*3*), and borders cells (*4*) are found in medial entorhinal cortex (MEC). Place cells fire when an animal is passing a specific single location in the environment (*5*); grid cells, in contrast to place cells, have multiple firing fields forming a striking hexagonal structure over the environment available to the animal (*6*). Head-direction cells fire whenever the animal is facing a particular direction, irrespective of its location or behavior at that moment (*7*), and border cells demonstrate border-associated firing fields (*4*). What is more, cells in MEC with conjunctive properties, such as combined grid × head-direction or border × head-direction firing, have been also described (*3, 4*).

The aforementioned observations imply that both hippocampus and entorhinal cortex provide neural information that allows the animal to navigate in local environment. Even though spatial representations of these two regions are probably closely dependent on each other, they also retain some fundamental differences. Entorhinal cortex has access to various spatial factors, such as position, distance, speed, direction, and boundaries, and cells that provide this information retain their spatial and directional firing in different environments (*6, 8*). On the other hand, hippocampal place cells seem not to have a universal code for metric representation as their firing fields differ with every novel space experience (*9*). This data led to the proposal that entorhinal cortex may drive path integration – an ability to navigate based on the integration of angular and linear motions according to idiothetic cues (*10*). However, a cornerstone component of path integrator would be a grid cell whose firing also depends on allothetic cues (*6*). To account for grid cells anchoring to environmental cues O'Keefe and Burgess proposed a model where allothetic information to grid cells is provided by place cells in hippocampus (*11*) and it can also be used to reset path integrator if computational errors occur (*12*). Therefore, entorhinal cortex could be understood as being part of the network that combines self-motion and environmental information to produce self-awareness in the environment.

Furthermore, entorhinal-hippocampal network was hypothesized to be involved in the formation of place fields. There are several models trying to explain how place fields could be extracted from grid fields. McNaughton et al. suggested that single place fields could be derived by linear transformation of several grid fields at variable scales (*10*). A different

approach uses a competitive Hebbian learning mechanism which could drive place fields formation when input from grid cells with overlapping spatial phases is available (*13*). Recently emerged model combines fixed grid-to-place cell connectivity with feedback inhibition within place cell population to simulate the appearance of place fields (*14*). Additional insight into spatial information processing between entorhinal cortex and hippocampus comes from studies dealing with the development of spatial representation system. It has been shown that when rat pups explore an open environment outside the nest for the first time stable place cells firing emerges earlier than grid cells firing does (*15, 16*). This could mean that the role of grid cells in place fields formation is expendable, which challenges initial expectations and proposed models.

Whichever type of spatial computation is being considered, be it path integration or grid-to-place field transformation, it requires an exchange of spatial information between entorhinal cortex and hippocampus. Extensive network of neural connections among hippocampal and parahippocampal cortices may facilitate the transfer of information leading to the realization of spatial cognitive functions. According to available anatomical data, neurons in layer II and III of entorhinal cortex project to dentate gyrus / CA3 and CA1 of hippocampus, respectively, whereas CA1 projections mainly target layer V of entorhinal cortex. There also exists intrinsic connectivity within the entorhinal cortex and hippocampus themselves (*17*). Nonetheless, the actual functional cell types of entorhinal cortex projecting to hippocampus have not yet been described but some implications and hints have been provided over the last ten years. From anatomical point of view, CA1 and CA3 regions receive projections from layer II and III in MEC, both of which contain grid, head-direction and border cells (*3, 4, 6*). Various lesion studies also imply direct functional connectivity between the two cortices. It has been demonstrated that after the removal of intrahippocampal inputs from CA3 area, place cell firing in CA1 persisted, raising the possibility that firing of place cells is driven by direct projections from entorhinal cortex (*18*). In a similar manner, when inputs from MEC layer III to CA1 were disrupted, the activity of place cells in CA1 was also impaired (*19*). Furthermore, the convergence of inputs from grid cells on hippocampus is supported by the fact that lesions in ventral MEC led to decreased size of place fields in the hippocampus (*20*). What is even more striking, grid patterns were recorded both in CA1 and dentate gyrus – areas where putative axons projecting from MEC should be found (*21*). Still, functional projections to hippocampus from entorhinal cortex remain to be unidentified.

It is evident that there exists high interest in neural computations happening within entorhinal-hippocampal space circuit and the actual knowledge of functional cell types projecting from entorhinal cortex to hippocampus is lacking. Consequently, this master's thesis aims to decipher functional interactions between the two mapping systems, which in turn would lead to the understanding of one of the first non-sensory cognitive functions of self-location in a microcircuit level. To satisfy the purpose of the thesis, combined optogenetic-electrophysiological approach will be applied. Virus carrying opsin transgene will be injected in the hippocampus area holding MEC projections. Viral payload should be retrogradely transported to MEC neurons with axons terminating in the hippocampus and in turn introduce optogenetic control over distinct MEC neuron population. To determine the functional identity of infected MEC neurons, *in vivo* tetrode electrophysiological records will be carried out in the dorsal-ventral axis of MEC while the animals will be running in a square enclosure. The aforementioned strategy of combining optogenetics with electrophysiological recordings *in vivo* will be used to answer these questions:

i. Is it possible to tag neurons projecting from entorhinal cortex and terminating on hippocampus using retrograde gene delivery approach?

ii. Can we determine the functional identity of hippocampus projecting entorhinal cells by combining optogenetics with electrophysiological recordings in vivo?

## 1.1 Hippocampal-Entorhinal Spatial Map

### 1.1.1 The Anatomy of the Hippocampal-Parahippocampal Region

#### Overview of the Hippocampal-Parahippocampal Region

Hippocampal-parahippocampal region of rats is comprised of two cortical structures: hippocampal formation and parahippocampal region (Fig. 1). General characteristic used to distinguish the aforementioned cortical structures is a number of cortical layers comprising them. The hippocampal formation has three-layered appearance and holds three distinct subregions: the dentate gyrus, the hippocampus proper (also known as the hippocampus) with its three CA (*cornu ammonis*) regions – CA1, CA2 and CA3, and the subiculum. The parahippocampal region, on the other hand, is generally described as possessing more than three layers (no more than six layers). It borders the subiculum of the hippocampal formation and is comprised of five subregions: the presubiculum, the parasubiculum, the entorhinal cortex (divided to medial (MEC) and lateral (LEC) entorhinal cortices), the perirhinal cortex (comprised of Brodmann areas 35 and 36) and the postrhinal cortex (*17*, *22*, *23*).

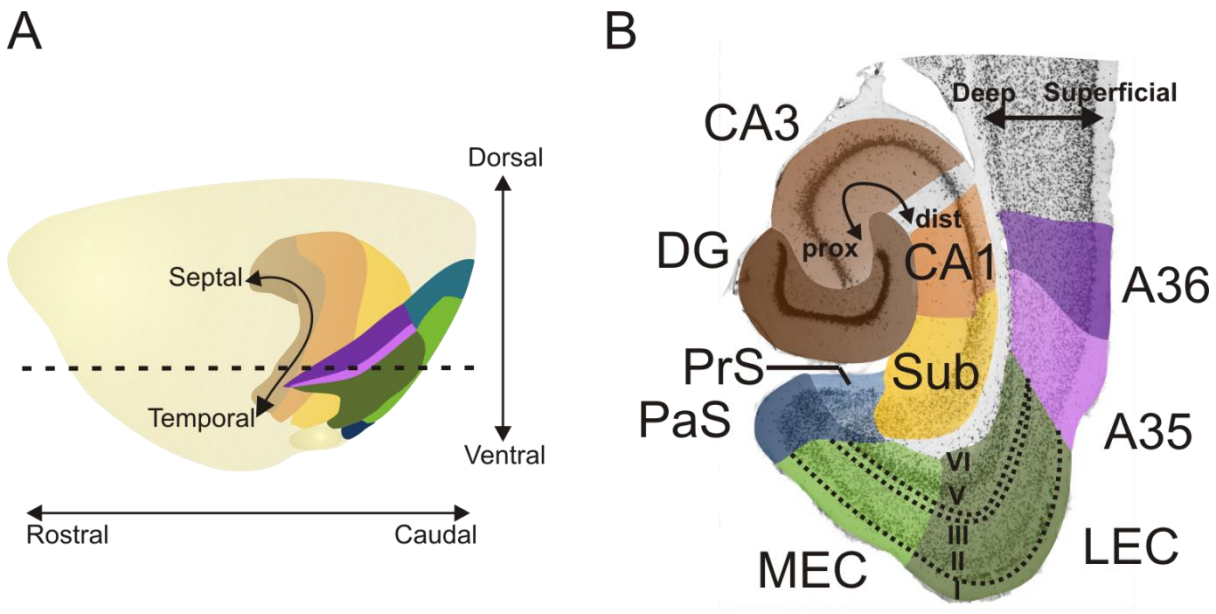


**Fig. 1.** Schematic representation of the hippocampal-parahippocampal region. **(A)** Lateral view. Septotemporal axis is indicated. The dashed line indicates the level of horizontal section, which is shown in (B). Colors represent various subregions in hippocampal formation and parahippocampal region, which are shown in detail in (B). **(B)** A Nissl-stained horizontal cross section. The two axes are shown: the proximodistal axis (prox-dist), starting at the dentate gyrus (DG) and running along the cell layer, and the superficial-to-deep axis. The hippocampal and parahippocampal subregions are color coded: dentate gyrus (DG, dark brown), CA3 (light brown), CA1 (orange), subiculum (Sub, yellow), presubiculum (PrS, light blue), parasubiculum (PaS, dark blue), MEC (light green), LEC (dark green) and the Brodmann areas 35 (A35, pink) and 36 (A36, violet). CA2 and the postrhinal cortex are

not indicated. Dashed lines and roman numbers indicate cortical layers in MEC and LEC. Adapted from (*17*).

## The Anatomy of the Hippocampal Formation

Hippocampal formation is divided into three subregions: the dentate gyrus, the hippocampus (comprised of CA1, CA2, CA3 fields), and the subiculum, all of them being characterized by three cytoarchitectonically distinct layers. In dentate gyrus these layers are termed hilus, granule cell layer, and molecular layer. Hilus (also known as polymorph layer) is the deepest layer (please refer to the deep-superficial axis in Fig. 1) and it holds various afferent and efferent fibers, GABAergic interneurons, and glutamatergic mossy cells – most common cell type in hilus. Hilus is enveloped by a "U" shaped granule cell layer. Granule cell is the principal cell type of dentate gyrus and its prominent feature is the lack of basal dendrites whereas apical dendrites ascend and branch within the molecular layer of dentate gyrus. In granule cell layer as in hilus prominent proportion of cells is interneurons. The most superficial layer of dentate gyrus is a molecular layer; it is mainly cell free and only occupied by the dendritic trees of granule cells (*17, 23*).

According to an extrinsic and intrinsic connectivity and the exclusive gene profiles, hippocampus is divided into three subfields – CA1, CA2, and CA3. Laminar organization follows closely the one seen in the dentate gyrus. The deepest layer is called stratum oriens, which is also mostly cell-free except from occasional interneurons. Superficial to the stratum oriens is the cell layer, which in hippocampus is composed of pyramidal neurons (it also holds basket cells). Basal dendritic tree of pyramidal cells extends into stratum oriens and apical dendritic tree – to hippocampal fissure. The most superficial layer (molecular layer) in hippocampus is divided into three sublayers which can be defined by the connectivity patters. The closest sublayer to the cell layer is referred to as stratum lucidum. It contains mossy fiber axons incoming from dentate gyrus and it can only be distinguished in CA3 but not in CA1 or CA2. Above stratum lucidum stratum radiatum is located, containing CA3-to-CA1 Schaffer collaterals and CA3-to-CA3 associational fibers. The most superficial layer is stratum lacunosum and here perforant pathway axons from entorhinal cortex terminate (*17, 23*). Furthermore, there exists a great variety of interneurons spread throughout stratum oriens, pyramidal cell layer, stratum radiatum, and stratum lacunosum (*24*). The subiculum retains the three-layered appearance of other hippocampal subregions. The most obvious property of the subiculum is a wider pyramidal cell layer. Together with the pyramidal cells, interneurons can be observed in the cell layer (*23*).

## The Anatomy of the Entorhinal Cortex

Based on its connectivity patterns and cytoarchitecture, entorhinal cortex is divided into medial entorhinal cortex (MEC) and lateral entorhinal cortex (LEC). MEC is defined by its inputs from presubiculum, dorsal thalamus, visual, and retrosplenial cortices. On the other hand, LEC receives input from piriform and insular cortices, amygdala, and olfactory structures (*25*). Entorhinal cortex is generally described as having six layers typically observed in neocortex and laminar organization between MEC and LEC shows a lot of similarities (*22, 26*).

The most superficial layer in the entorhinal cortex, layer I, is sparsely populated by two types of GABAergic interneurons, horizontal and multipolar neurons. These neurons are thought to project to layers II and III to provide inhibition to principal cells located there (*22, 26*). Layer II in MEC is mainly populated by stellate cells whose characteristic feature is a spiny dendritic tree (*27*). In LEC stellate cells are replaced by fan cells with morphology being similar to the one of stellate cells; however, with different electrophysiological properties (*28*). Another cell type located in layer II is pyramidal-like cells, which have triangular or ovoid shaped soma and are usually found in the deeper part of layer II. Principal cell population in layer II send axons towards the angular bundle and is a major constituent part of perforant pathway targeting dentate gyrus and CA3 / CA2 regions (*22, 26*). The principal cells in both MEC and LEC layer III are pyramidal cells with axons projecting through angular bundle to subiculum and CA1 region (*22, 26, 28*). Layers II and III also hold various types of interneurons, most of them providing local inhibition, whereas horizontal and multipolar cells also project to hippocampus (*26*). Layer IV (also known as *lamina dissecans*) is mostly cell-free layer, with occasional pyramidal-like cells and interneurons located there; however, those principal cells have morphological and physiological properties of either layer III or layer V neurons (*22*). Principal neurons in layer V of MEC and LEC show high similarity in their morphology and electrophysiological properties. The most abundant principal cell type is pyramidal cells which are mainly localized in more superficial parts of layer V. Smaller cells, like horizontal or multipolar neurons, are located deeper into layer V (*29, 30*). The deepest layer of entorhinal cortex, layer VI, is populated by multipolar neurons (*22*).

### 1.1.2 Hippocampal Map

In late 1940s, Tolman was the first to postulate a hypothesis of an internal cognitive map. He described the cognitive map as a neural network reflecting spatial relationships in the animal's environment (*31*). However, it took another 25 years until a neural basis for the hypothesis of cognitive map was laid with the discovery of place cells in the rat hippocampus. Place cells are hippocampal pyramidal neurons that fire when the animal is in a particular position in the environment – the place field of the cell (Fig. 2A). Furthermore, place cells fire independently of a specific motor behavior or sensory inputs (*1, 5*). They can be found in CA1 (*5*) and CA3 (*32*) areas of the hippocampus but cells indicating comparable functional properties have been discovered in the subiculum, the septal presubiculum and the parasubiculum (*17*). The discovery of place cells led O'Keefe and Nadel to propose that the Tolmanian cognitive map is in fact located in the hippocampus (*33*). This cognitive map could be innate as it was demonstrated that place cells can be detected as early as postnatal day 15 (P15) - as preweanling rats begin to actively explore their environment (*16*).

The place field size itself is topographically graded, meaning that a place field diameter varies according to the location of the corresponding place cell in the hippocampus. The place fields of place cells recorded from CA3 area in rats varied from <1 meter at the dorsal part to ~10 meters at the ventral pole (*32*). Hippocampal place cells are able to change their firing patterns in response to various environmental manipulations – a phenomenon called remapping. A single place cell can have different place fields in the same environment if the cognitive inputs are changed (e.g. alternative position of the cue card) or it can obtain new place field when the animal is moved to a new environment (*9*). Global remapping occurs when place fields disappear, appear or move to a novel location, while changes in the firing rates of place cells are termed as rate remapping (*34*). In addition, different place cells possess different place fields in a manner that the whole environment can be described with the activity of place cell population; actually, it is feasible to establish the position of the rat from the large ensemble recordings of neurons (*35*). However, it was shown that anatomically close pyramidal neurons in hippocampus do not have correlated firing patterns, i.e. no topographical pattern can be established between their firing fields (*36*).

Not only spatial information is stored in the place cell code. Place cells were shown to be able to convey conjunctive information between olfactory and spatial inputs. What is more exciting, is that place cells can also encode time intervals relevant to the task. These findings

suggest that these hippocampal cells can play an important role in episodic memory encoding relating location and specific experiences (*37*).

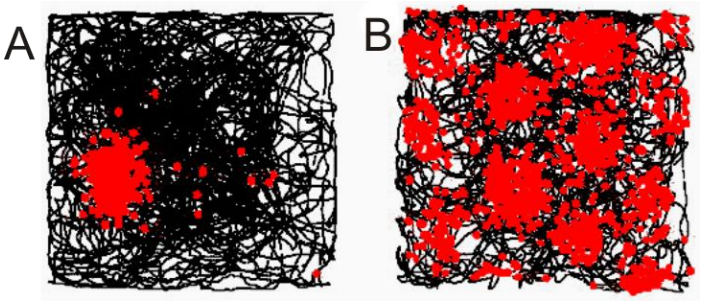


**Fig. 2.** Examples of a place and a grid cell firing. The trajectory of the animal is marked by the black line and the superimposed spike locations are marked with the red dot. **(A)** Example of the place cell firing; the cell has single firing location. **(B)** Example of the grid cell firing; multiple firing fields of the cell forms a hexagonal grid. Adapted from (*37*).

### 1.1.3 Entorhinal Map

Since the discovery of the place code in the hippocampus, it was assumed that the place cell signal was generated in accordance with the computations within the hippocampus formation itself. However, this view had been put to a test when it was demonstrated that the spatial discharge of CA1 and CA3 cells persisted even when the intrahippocampal inputs from dentate gyrus were terminated (*38*); similarly place cell discharge in CA1 area remained stable after the removal of intrahippocampal inputs from CA3 area (*18*). These findings suggested that spatial signal of place cells originated outside the hippocampus and the foremost candidate was the entorhinal cortex, considering the fact that the latter was providing most of the cortical input to the hippocampus. The initial recordings from entorhinal cortex failed to reveal cells with spatially modulated firing patterns (*39*); however, after the examination of the dorsal part of MEC a new light was shed on the spatial representation in the parahippocampal region – grid cells have been discovered (*2*).

Initially grid cells were discovered in MEC of rats, but up to now their existence has been reported also in mice, humans and bats (*40*). Grid cells can be found in MEC [layers II, III (*2*), V and VI (*3*)], pre- and parasubiculum (*41*) in the rat. A grid cell can be defined as a neuron having multiple firing fields that collectively form a hexagonal pattern across the environment available to the animal – a so-called grid (Fig. 2B). Each grid can be described by three metric properties: orientation (direction), phase (location of the grid in *xy* coordinates) and spacing (distance between firing fields). Proximate grid cells (i.e. recorded at individual recording positions) possess similar grid orientation and spacing. On the other

hand, grid spacing increases along dorsal-ventral gradient in MEC, ranging from ~30 cm in the most dorsal grid cells to several meters in the grid cells from the most ventral part of MEC (Fig. 3A); mimicking a similar trend of the place fields of hippocampus (*32*). Recently it has been shown that grid cells cluster into discrete modules, which possess distinct grid scale, orientation, and grid distortions when changes are introduced in the shape of the environment. These grid modules are overlapping anatomically and are widespread across both axes in the MEC (*42*). Also grids from a several grid cells recorded at the same electrode will cover the complete environment (Fig. 3B) (*6*).

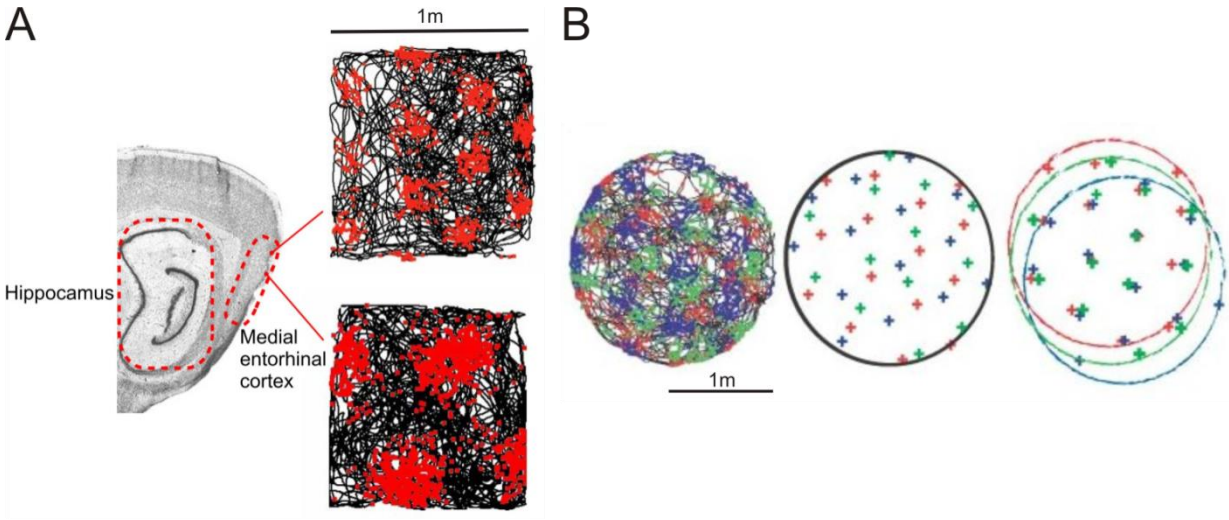


**Fig. 3.** Grid spacing and phase examples. **(A)** The trajectory maps of two grid cells recorded in 1 $m^2$ box from the same animal but at the different parts of the MEC are shown; approximate recording positions in the MEC are indicated. The grid cell (upper one) recorded in a more dorsal position possesses smaller grid spacing compared to the ventral grid cell (lower one). Adapted from (*40*). **(B)** The phases of three proximate grid cells represented by the separate colors. Left, the trajectory map of three grid cells recorded in a circular box with a radius of 1 m. Middle, peak locations of the three grid cells. Right, the visualization of similar grid spacing and orientation. Adapted from (*6*).

Another class of cells involved in navigation and located in the same parahippocampal region as grid cells are termed head-direction (HD) cells. In fact, HD cells were first discovered in the presubiculum (*7*, *43*) and only later discovered in other brain regions (*44*), one of them being MEC (*3*). HD cells fire when animal is facing a particular direction, irrespective of animal's behavior or location, and all directional headings are represented equally within HD cells' population. Each HD cell can be described by two parameters – its preferred firing direction and peak firing rates. Preferred firing direction usually has a range of ~90° and peak firing rates vary from 5 Hz to >120 Hz (*7*, *44*). Furthermore, HD cells located in medial entorhinal cortex (in layers III-VI) possess conjunctive grid × head-direction

properties. Those HD cells fire only when the animal is crossing a grid field in a certain direction and it has been postulated that HD cells may control grid field orientation (*3*).

Recently, novel spatial cells have been described in MEC. Cells demonstrated border-associated firing fields, and therefore have been called “border cells”. Border cells can be found in all layers of MEC but are relatively sparse compared to HD cells or grid cells, comprising less than 10% of the principal cell population. It has been suggested that border cells can play a role in anchoring both place and grid fields to a geometric reference frame (*4*).

### 1.1.4 Hippocampal-Parahippocampal Network

It is a well-established fact that there exists an extensive network of neural connections within and among hippocampal and parahippocampal cortices. Anatomical knowledge of this network is of a fundamental importance if we want to decipher both functional roles and relations of these two regions. The basic view of parahippocampal-hippocampal network presents entorhinal cortex as a major input region of cortical information which in turn is transmitted to hippocampal structures, from where hippocampal output reaches entorhinal cortex again to be relayed back to the cortex (Fig. 4). Let us take a closer look into the aforementioned circuitry.

To begin with, a major cortical input to entorhinal cortex is provided by perirhinal and postrhinal cortices. The perirhinal cortex preferably projects to LEC and the postrhinal cortex projects to MEC. Both perirhinal and postrhinal projections terminate in layers II and III of entorhinal cortex. Based on the types of inputs that are received by perirhinal and postrhinal cortices, it is believed that perirhinal cortex-LEC and postrhinal cortex-MEC pathways transmit nonspatial and spatial information to hippocampus, respectively. The entorhinal cortex itself provides reciprocal projections to perirhinal and postrhinal cortices (*45-47*). While connections projecting from presubiculum and parasubiculum and terminating on MEC and LEC, as well as reciprocal connectivity, exist, they are modest compared to the connectivity between entorhinal cortex and hippocampus or perirhinal and postrhinal cortices (*17, 25*). As expected, there also exists an extensive network of intrinsic connectivity within the deep and superficial layers of LEC and MEC (*48*).

A prominent input to hippocampus, dentate gyrus and subiculum originate in entorhinal cortex and this circuitry is known as a perforant pathway. The perforant pathway can be viewed as composed of two components. One component is projections mainly from MEC

and LEC layer II principal cells terminating on dentate gyrus and hippocampal CA3/CA2 layers. The overlap of MEC and LEC terminal zones is not observed. LEC projections terminate on outer parts of the molecular layer of dentate gyrus, whereas MEC neurons terminate on the remaining parts of the layer. A similar pattern is observed in CA3, where LEC projects to the outer part of the molecular layer and MEC neural projections terminate on deeper part of the stratum. The other component is a circuitry originating in MEC and LEC layer III neurons and terminating on subiculum and hippocampal CA1 layer. It is worth mentioning that LEC layer III neurons project to the proximal subiculum and distal part of CA1, whereas MEC layer III projections terminate on the distal subiculum and proximal part of CA1 – projections show a transverse topography (*17, 22, 23, 26*).

The circuitry within the hippocampus formation is referred to as polysynaptic pathway and traditionally is viewed as a unidirectional route. Dentate gyrus granule cells give rise to mossy fibers that terminate on CA3. CA3 pyramidal cells give rise to Schaffer collaterals that project to CA1 which in turn projects to the subiculum completing the polysynaptic pathway (*17, 23*). There are exciting features concerning a topology of CA3-to-CA1 and CA1-to-subiculum connections. Proximal part of CA3 projects to distal CA1, whereas proximal CA1 is targeted by distal CA3 (*49*). Regarding the CA1-to-subiculum circuitry, a similar topographical pattern is observed – proximally located CA1 cells project to distal subiculum and distal CA1 area projects to proximal part of the subiculum (*50*). Furthermore, CA3 pyramidal cells possess an extensive network of collateral axons that interconnect CA3 neurons; these projections are known as associational fibers (*49, 51*). Lastly, the unidirectional nature of the intrahippocampal connectivity is widely accepted; however, all the components of the polysynaptic loop have backprojections – subiculum-to-CA1, CA1-to-CA3 and CA3-to-dentate gyrus (*17*).

To complete parahippocampal-hippocampal network, there exist projections arising from the subiculum and CA1 and terminating on entorhinal cortex, mainly on the layer V of the MEC and LEC. More interestingly, projections from the subiculum / CA1 to entorhinal cortex are in register with the projections entorhinal cortex to subiculum / CA1, i.e. completely reciprocal. Distal part of the subiculum and the proximal part of CA1 projects to MEC, whereas projections from neurons in proximal part of the subiculum and the distal part of CA1 target LEC (*23, 52*).

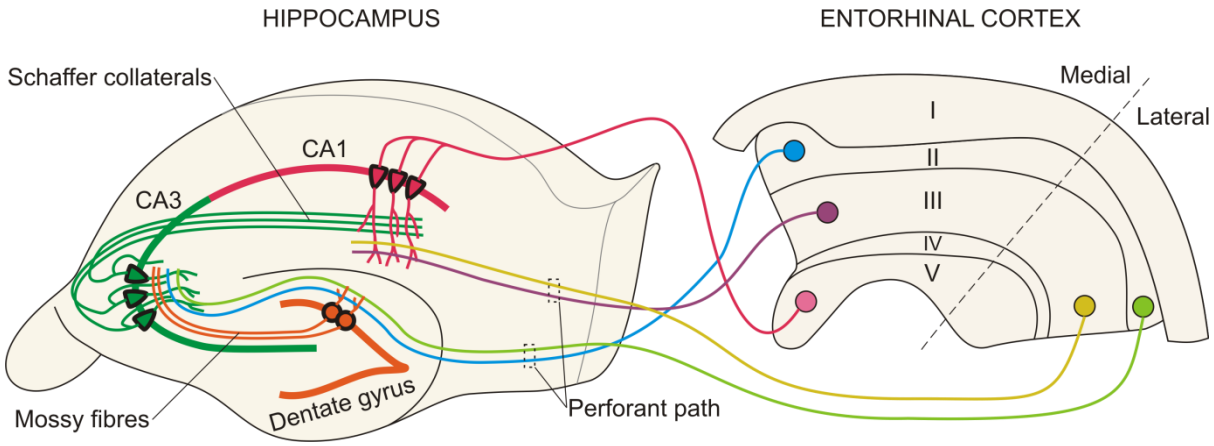


**Fig. 4.** Basic hippocampal-entorhinal cortex network. The standard hippocampal-entorhinal cortex circuitry is viewed as a trisynaptic loop. Projections from entorhinal cortex to the hippocampus are termed as a perforant path: the neurons in layer II of MEC and LEC target dentate gyrus and CA3, whereas the layer III projections end up in CA1. Intrahippocampal network is presented here as composed of two components: mossy fibers, connecting dentate gyrus with CA3, and Schaffer collaterals, connecting CA3 with CA1. Lastly, CA1 projects back mainly to entorhinal cortex layer V (both in MEC and LEC, which is not shown in the figure). The roman numbers indicate cortical layers, circular cells represent granule cells in dentate gyrus, whereas the triangular cells represent pyramidal cells in CA3 and CA1. Based on (*53*).

### 1.1.5 Path Integration

Navigation, in its plain form, is the ability to find the location of the goal without using any external landmarks. This is brilliantly demonstrated by the desert ant, *Cataglyphis fortis*, which is able to find its way back to the nest after a journey of hundreds of meters over featureless terrain (*54*). The aforementioned process now is known as a path integration and can be defined as the animal's ability to pinpoint specific location by integrating angular and linear motion according to idiothetic cues (*55*). Before the discovery of grid cells, hippocampus was a possible candidate for a path integrator. However, hippocampal place cells received some criticism for their role in the path integration. Essentially, place fields are strongly dependent on the landmarks of the environment, meaning they are "tied" to a particular environment and do not provide a universal code for metric representation (*9*, *12*). Also it has been suggested that place cells only express the output of the path integration system located outside of the hippocampus (*10*).

The recent studies suggest that MEC could carry the role of the path integrator with its grid and head-direction cells. First of all, according to study done with rats, lesions in MEC deprived the rats of the ability to integrate return path only depending on idiothetic cues (*56*). Second, grid fields are formed rapidly in a novel environment, updated in the absence of visual input (e.g. completely dark room) and persist after the removal of external sensory cues

(*6, 57*). Third, spacing of the grid fields remains stable across different environments – a property which is not seen with place fields (*6, 57*). Fourth, MEC also contains head-directions cells which not only provide a sense of directionality to the path integrator but also have constant directional tuning across environments (*54*). Last but not least, the co-localization of grid and head-direction cells and existence of conjunctive grid × head-direction cells puts all the needed components for the path integrator in the local circuit (*3*).

However, the grid map (grid phase and orientation, in particular) can be anchored to landmarks and geometrical boundaries which raise a question how somewhat contradictory processes of path integration, based on idiothetic cues, and anchoring to environmental cues are combined within the circuitry. To begin with, there is a strong empirical foundation showing that grid maps can be anchored to environmental cues. Since the first behavioral investigations of grid cells' firing, it has been noticed that grids rotate together with the rotation of landmarks in a circular environment (*6*). What is more, it has been reported that grid fields show deformation in response to deformation of the available environment, a phenomenon known as rescaling (*58*). The mechanism of grid fields anchoring to specific environmental landmarks has not yet been delineated, but O'Keefe and Burgess proposed an interesting model (*11*). Entorhinal cortex is connected to hippocampal formation through backprojections from hippocampus terminating mainly on deep layers of MEC (*52*). They suggested that through this circuitry information about environmental cues and boundaries come from hippocampus and reach grid cells located in MEC. Furthermore, it has also been postulated that information from hippocampal place cells can reset entorhinal path integrator to eliminate errors that are accumulating during movement (*12*). In accordance with this theory, it has been shown that hippocampal inactivation leads to grid fields' destabilization (*59*). Alternatively, association of grid fields with environmental landmarks can happen with the MEC itself, when sensory inputs from postrhinal cortex are combined with firing patterns of grid cells (*10*). Whatever might be the mechanism, it seems that entorhinal cortex plays a major role in enabling the combination of idiothetic and allothetic cues which in turn lead to self-awareness in the environment.

### 1.1.6 From Grid Fields to Place Fields

Strong entorhinal input originating in MEC layers II and III and terminating at hippocampus CA1 and CA3 suggests that the formation of the place fields arises from some kind of transformation between the activities of grid and place cells (*17*). Currently there are several proposed models that try to explain how grid fields are employed to generate place fields.

According to the first model, which is inspired by Fourier analysis, place fields are generated when signals of grid cells are combined linearly. It can be expected that place signal generated this way would be periodic, i.e. a peak would appear where contributing grid cells would be in a phase; however, the period would be large because it would represent the least common multiple of the grid spacings, hence in normal experimental settings only one place field would be observed (*10*). Solstad et al. (*60*) showed with a computational model that the combination of the inputs from 10-50 grid cells with random grid orientations, similar phases and spacing is enough to form a single place field (Fig. 5). In favor of the aforementioned model is an observation that lesions in ventral MEC led to decreased size of the place field in the hippocampus (*20*); this can be expected as convergence of inputs from smaller grid fields located in dorsal MEC (the ones left after the lesions in ventral MEC) would lead to the small place fields. According to another model, place fields could be generated by random connectivity between place and grid cells, whereas latter ones should have variable grid orientation, phase and spacing (*13*). This model is based on competitive Hebbian learning process (involves synaptic plasticity) and it received only a partial support because it has been shown that place fields develop in the presence of NMDA receptor blockers (*61*), meaning that synaptic plasticity may

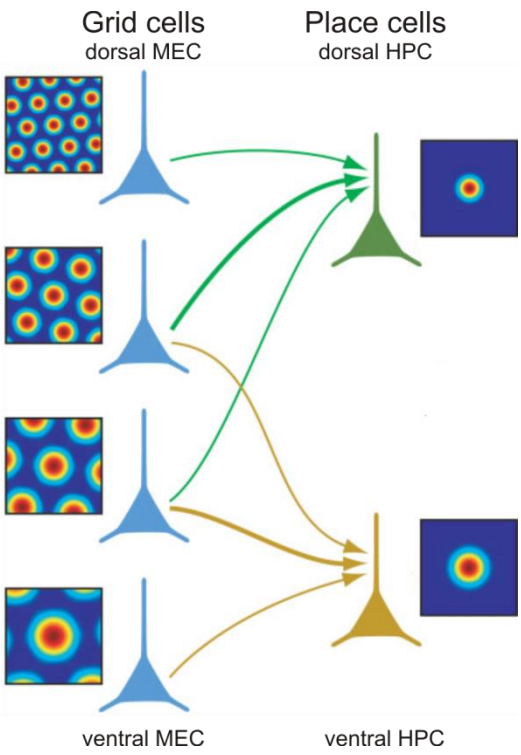


**Fig. 5.** Model for place field formation. The hypothetical connectivity between the grid (blue) cells in the medial entorhinal cortex (MEC) and the place cells (green / yellow) in the hippocampus (HPC) is shown. Dorsal grid and place (green) cells have small grid spacing and small place fields, accordingly, whereas the ventral grid and place (yellow) cells have big grid spacing and big place fields, accordingly. The lines represent input from grid to place cells which is used to generate place fields.

not be critical to LTP based grid-to-place field transformation. Taking into account the phenomenon of place fields remapping, Monaco and Abbott suggested that grid-to-place cell transformation can be achieved by network competition, which is based on feedback inhibition within the place cell population (*14*). Even though current computational models suggest different approaches for solving the same problem, it does not mean that one of them should be looked upon as the "correct" one. With the advances in the field it may turn out that spatial representation in the hippocampus relies on the convergence of various aspects outlined in all of the different approaches.

Recently it has been shown that when the rat pups explore their environment for the first time, place cell firing is already present, whereas grid cell firing develops later (*15, 16*). Furthermore, is was also demonstrated that place cell firing persists under condition where grid cell firing is reduced (*62*). These findings imply that grid cells may be not that critical in place cell formation as it was expected initially. Another MEC located spatially regulated cells – border cells - can provide the necessary component for the spatial code formation in the hippocampus. This was speculated even before grid cells and border cells were discovered (*63*), nonetheless, border related information is yet to be included in the computational models dealing with the subject. For that matter, do head-direction cells in MEC also have their say in the place field formation and what about combined output from grid cells, border cells and head-direction cells? These are intriguing questions which will hopefully be addressed as in the coming years.

## 1.2 Optogenetics

### 1.2.1 The Evolution of Optogenetics

In the article "Thinking about the Brain" published in 1979 by Francis Crick, it is stated that in order for neuroscience to move forward we need a method that would enable scientists to manipulate one type of neurons while others are left unaltered (*64*). Later in the paper dealing with molecular biology within neuroscience field he speculated that light could be employed to manipulate neurons: "This seems rather farfetched but it is conceivable that molecular biologists could engineer a particular cell type to be sensitive to light <…>" (*65*). In an unrelated line of research (at least how it seemed at the beginning) bacteriorhodopsin was discovered, which acted as a microbial light-activated ion pump (*66, 67*). Following years saw an expansion in the field of microbial opsins, both in the deeper understanding of bacteriorhodopsin and the identification of the new members of the microbial opsin family:

halorhodopsin (*68*) and channelrhodopsin (*69*). However, it took a couple of decades for these two separate concepts to be combined into a new field which is known today as optogenetics. Main reason why the birth of optogenetics was so delayed is several hypothetical drawbacks for employing opsin proteins to control activity of specific neurons. It was assumed that opsin proteins would be poorly expressed or toxic to mammalian neurons, their generated photocurrents would be too weak or too slow to elicit the desired response and most importantly that additional injections of cofactors, such as retinal, would be needed for the activity of light-activated ion channels (*70*). Yet all the aforementioned potential obstacles have been abolished when it was demonstrated that it is actually feasible to evoke action potentials on mammalian neurons after introducing microbial opsin gene (*71*). This marked both birth and start of remarkable expansion of optogenetics, which can be defined as "<…> the combination of genetic and optical methods to achieve gain or loss of function of well-defined events in the specific cells of living tissue" (*70*).

### 1.2.2 Structure and General Properties of Opsin Proteins

A general feature of opsin proteins is seven transmembrane $\alpha$-helices that form an internal pocket where cofactor retinal (vitamin A aldehyde) is bound. Retinal is a chromophore which is covalently bound via a protonated Schiff base linkage to $\varepsilon$-amino group of a lysine in the seventh helix; the opsin-retinal complex is referred to as rhodopsin (Fig. 6). After absorption of photon, retinal isomerizes, leading to conformational changes within the rhodopsin itself, which drive various functions, from ion transport to interaction with signaling proteins, depending on the rhodopsin in action. Opsin genes can be split into two distinct families: microbial opsins (type I) and animal opsins (type II) (*72*). There is no sequence homology between the two families, however, within the families homology is high (25% - 80% sequence similarity) (*73*).

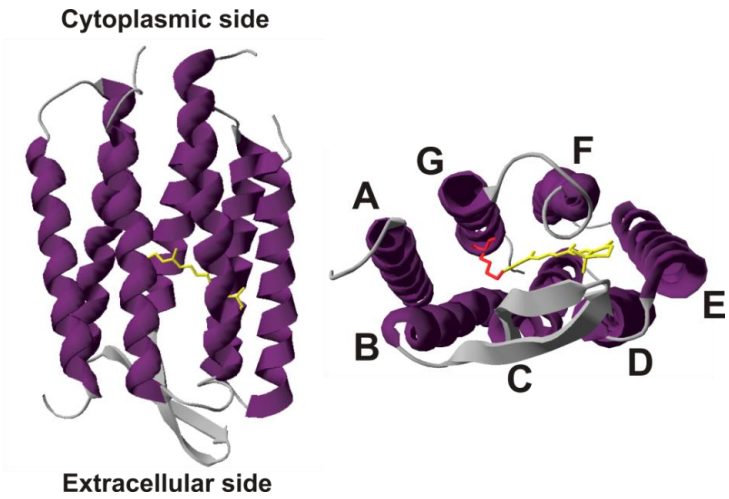


**Fig. 6.** Crystal structure of archaeon *H. salinarum* bacteriorhodopsin (PDB code: 1C3W). The protein is shown viewed along the cell membrane plane (left structure) and from the extracellular side (right structure). The color used for representation is the approximate color of the pigment. The helixes names are given and the retinal (yellow color) is shown bound to Lys216 (red color) on helix G.

Type I opsin genes are found in prokaryotes, algae and fungi and are responsible for phototaxis, retinal synthesis and energy storage (*74*). Type one rhodopsins use all-*trans* retinal as their cofactor which, following the absorption of a photon, isomerizes to 13-*cis* configuration. Retinal remains covalently bound to the protein and thermally converts back to all-*trans* state with the completion of a photocycle (*75*). On the other hand, type II opsin genes have been only detected in higher eukaryotes and are mainly responsible for vision; type II rhodopsins function as G protein-coupled receptors, whereas type I rhodopsins mainly act as ion transporters (*74*). In contrast with type I opsin proteins, type II utilize 11-*cis* retinal which isomerizes to all-*trans* form. What is more, all-trans retinal is then hydrolyzed and removed to be able to transform back to 11-cis configuration; later a new 11-cis retinal is recruited to the chromophore binding pocket (*75*). Due to aforementioned differences in retinal rotation and biological functions, type I opsins are being employed for manipulating electrical activity of neurons (Fig. 6) and show faster kinetics, whereas type II opsins have slower kinetics and are being applied to modulate biochemical events in cells (*73*). Only optogenetic tools for neuronal inhibition / excitation will be discussed in the following chapters, whereas area of optogenetic tools for biochemical control will not be touched as it is not involved in my project.

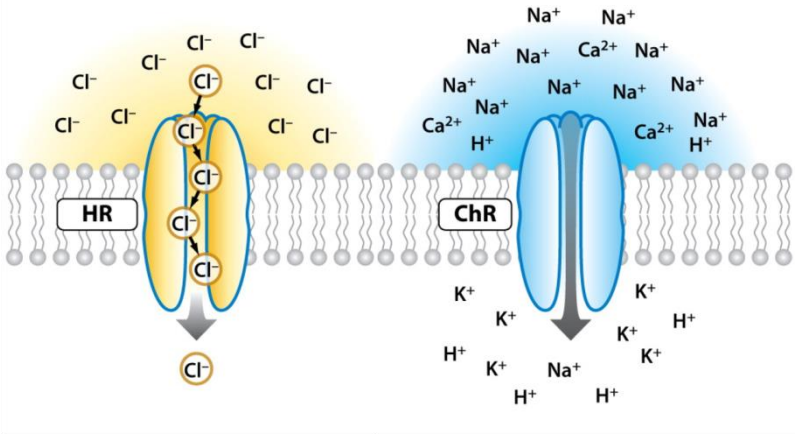


**Fig. 7.** Optogenetic toolbox for neural inhibition / excitation. Halorhodopsin is being applied to hyperpolarize neurons when upon the yellow illumination it conducts chloride ions into the cell (left). Channelrhodopsin (ChR) is being applied to depolarize neurons when upon the blue light illumination it conducts cations down their electrochemical gradient (right). Adapted from (*76*).

### 1.2.3 Optogenetic Tools for Neural Inhibition

As of today one ion pump is being used widely for inhibiting neurons, namely halorhodopsin (HR), however, new opsin genes are being surveyed to expand optogenetic toolbox for neuronal inhibition. HR acts as a chloride pump and transports chloride ion from extracellular medium into the cell (*75*). During initial screenings, HR from *Natronomonas pharaonis* (NpHR) was chosen as a suitable candidate for inhibiting neurons, due to higher extracellular $Cl^-$ affinity and stability compared with HR from *Halobacterium salinarum* (HsHR). It is worth noting that HR absorption maximum is at ~580 nm, meaning that it could be used together with another opsin protein – channelrhodopsin-2 (Chr2), which shows no response at that wavelength and is employed for neuronal activation (*77*). Furthermore, NpHR acts as true pump and requires constant illumination to maintain its activity (*78*). It has been demonstrated that NpHR can deliver loss-of-function optogenetic control to mammalian brain slices, cultured neurons and muscles of nematode *Caenorhabditis elegans* (*77*).

However, the usage of the NpHR to induce the inhibition of the neural activity in intact mammalian brain was hindered by membrane trafficking problems (*78*). A new NpHR was engineered by adding ER export motif derived from Kir2.1 potassium channel, producing eNpHR2.0 with improved plasma membrane localization (*79*). Further addition of trafficking signal from Kir2.1 to eNpHR2.0 yielded third generation NpHR, named as eNpHR3.0. eNpHR3.0 possessed stronger inhibition of neurons, lower light power requirements for activation, as well as absorption shifted to red wavelengths (up to 680 nm) (*80*). And it was not long until new optogenetic tool found its way into *in vivo*. The first application of

eNpHR3.0 was elucidation of cholinergic interneurons of the nucleus accumbens role in cocaine conditioning in a freely moving mice (*81*).

The search for new opsin proteins that could be used to efficiently hyperpolarize neurons *in vivo* continues. Various rhodopsins are being surveyed by different groups for potential future applications, such as bacteriorhodopsin from *Halobacterium salinarum* (BR) (*80*), proton pump from the fungus *Leptosphaeria maculans* (Mac) or archaerhodopsin-3 from *Halorubrum sodomense* (Arch) (*82*). All of the aforementioned opsins show high efficiency, however further research is needed to investigate their functionality in mammalian neurons (*78*).

### 1.2.4 Optogenetic Tools for Neural Excitation

Complementing the tools for neural activity silencing, light gated ion channels – channelrhodopsins – are being employed to achieve precise neuron excitation. Channelrhodopsin-1 (ChR1) was discover in green alga *Chlamydomonas reinhardtii*, followed by the discovery channelrhodopsin-2 (Chr2) in the same organism one year later (*69, 83*). ChR1 acts as light-gated ion channel conducting $H^+$, $Na^+$, $K^+$ ions down their electrochemical gradient; ChR2 also conducts same ions, however, it is two times more permeable to $Na^+$ and $K^+$ ions than to protons (*74*). Since the initial demonstration that ChR2 can be used to evoke action potentials on mammalian neurons (*71*), ChRs gained a fair amount of attention from scientific community and optogenetic toolbox was vastly expanded due to ChRs' gene engineering.

Initial modifications of ChR2 led to the creation of now widely used version hChR2(H134R). hChR2 stands for humanized ChR2 which has higher expression levels in mammals and has been generated by exchanging algal codons with mammalian ones (*71*). Furthermore, H134R mutation introduces ~2 fold higher current with also ~2 fold slower channel-closure kinetics (*78*). Thus, as hChR2(H134R) has some benefits in comparison to a wild type ChR2 but it also brought poorer temporal control.

Another type of opsin gene mutations generated a new class of optogenetics tools, termed step-function opsins (SFOs). While the wild type ChRs deactivate with a time constant of ~10 ms, SFOs have closing time constants reaching up to ~100 s. This allows to create stable steps in membrane potential and, what is more, photocurrents can be terminated by shinning different color light compared to the one used for channel activation. This has been achieved by introducing mutation in cysteine-128 in ChR2, thus new mutants are referred to

as ChR2(C128X). For instance, mutants C128T, C128A, and C128S has closing time constants of ~2 s, ~50 s, and ~100 s, respectively. As the authors themselves suggest, SFOs could have various applications in neuroscience field, ranging from studies dealing with the role of specific cell types in neuroplasticity to mimicking oscillations of neural populations (*84*). Further research in engineering stable opsins brought an improved version of SFOs, termed stable SFOs (SSFOs). Mutant ChR2(C128S/D156A) showed remarkable stability of the activated state with the closing time constant of ~30 min. This opens up exciting opportunities as the neurons of interest can be "stepped" into a stable depolarized potential and an animal itself could be unplugged from light hardware to freely carry out its behavioral tasks (*85*).

All of the aforementioned variations of ChR2 are unable to evoke spiking in higher frequencies (i.e. >40 Hz). What is more, ChR2 activation can lead to extra spikes (e.g. doublets) in response to a single light pulse as well as plateau potentials of 10 mV or more; this can be important for neural-coding and have information-processing implications. All of these limitations of previous ChR2 mutants have been addressed by engineering new opsin gene where E123 residue is replaced either by threonine or alanine. A newly designed opsin was termed ChETA and allowed optical stimulation up to 200 Hz which highly improves the precision of optogenetics (*86*).

Different ChRs can be combined together raising the possibility of combinatorial excitation – the ability to control two separate populations of neurons within the same volume, for example in neural circuits. Initial genomic searches identified opsin from alga *Volvox carteri*, named as VChR1, with a red-shifted absorption maximum at 589 nm, which allowed it to be used together with ChR2 (absorption maximum at 480 nm) for combinatorial excitation. However, VChR1 had low expression in mammalian neurons which led to poor depolarization currents (*87*). To improve performance of VChR1, a novel opsin was constructed – a chimera between ChR1 and VChR1 – opsin C1V1. The action spectrum of C1V1 remained red-shifted, whereas generated currents were even higher than those observed with ChR2 (*85*). This, when applied together with ChR2, created a powerful tool to control two distinct groups of neurons *in vivo* simultaneously.

### 1.2.5 Delivering Optogenetic Tools

A conventional optogenetic experiment *in vivo* involves the essential step of the optogenetic tool delivery to neurons and oftentimes targeting of a selected neuronal population. To

achieve these goals, various strategies are employed: viral promoter targeting, transgenic animal targeting, and projection targeting.

**Targeting with Viruses**

Viral gene delivery is a usual method of choice for delivering opsin genes to neurons for numerous advantages. Viral gene expression systems have rapid implementation leading to stable long-term expression and high infectivity, which is a desirable feature as high opsin number in neurons is necessary for robust and optimal current generation (*76, 78, 88*). Adeno-associated virus (AAV) and lentivirus are two of the most used viral systems for opsin delivery and have been successfully exploited to introduce opsin genes into a mouse, rat, and primate's brains (*76, 78, 89*). Due to the fact that AAV vectors do not integrate into the host genome, whereas lentiviral vectors do, the former one is more preferable choice. Integration into the genome of host cells could lead to the dependence of opsin gene expression on surrounding genome as well as disruption of host genes (*90*). However, a major drawback of AAV and lentiviruses is limited genomic packaging capacity, being ~5 kb and ~8 kb, respectively. This means that only short promoter fragments can be used with these systems which can sometimes become a serious issue to overcome (*88, 90*). Optional viral systems with a greater carrying capacity include adenoviral or herpes simplex-based (HSV) vectors, however, HSV has its own shortcomings – higher toxicity as well as inconsistency between experiments (*78*).

The most widely used AAV serotype for opsin delivery is recombinant AAV2 vector (AAV2). More varied versions also exist when AAV2 is pseudotyped with viral capsids from serotypes 1, 2, and 5 (rAAV2/1, rAAV2/2, and rAAV2/5, respectively). All these serotypes vary within themselves according to viral spread in CNS. For instance, when injected into a rat hippocampus, rAAV2/1 and rAAV2/5 diffuse more profoundly, targeting CA1-CA3 regions, whereas rAAV2/2 show more restricted transduction in dentate gyrus (*91*). In comparison, lentivirus is even more restricted and can be exploited to target subfields of CA1 region (*78*). It is reasonable to believe that additional serotypes will appear which will only expand targeting strategies.

Specific neural population targeting with viral opsin delivery can be achieved using cell type specific promoters driving the expression of an opsin gene. However, due to the limiting packaging capacity of viruses only short promoter fragments can be applied; therefore, the number of available promoters to fit this criterion and also be able to drive strong and specific

opsin expression in mammalian brains is also limited at the moment. A frequently encountered promoter that ensures strong expression in neurons is elongation factor 1-alpha (EF-1α) (*92*). More specific targeting is reached when using two human promoters - human synapsin (Syn) and human thymocyte-1 (Thy-1), which drive gene expression in neurons while excluding glia (*93*), whereas promoter of glial fibrillary acidic protein (GFAP) targets astrocytes instead of neurons (*94*). Furthermore, α-calcium/calmodulin-dependent protein kinase II (CaMKIIα) promoter targets cortical excitatory neurons (*95*). To sum up, while promoter based cell-type-specific expression of genes in neural systems had some progress and the aforementioned examples had been used extensively in optogenetics' field (*78*), it is far from the stage where specific promoters are available for most neuronal subtypes.

**Transgenic Animal Targeting**

Drawback of viral payload limitations can be overcome by a transgenic animal approach, where specific transgenic animal lines can be generated, which express opsin genes stably with cell-type-specificity and without the need of gene delivery using viruses on a single animal basis. The first transgenic animal line was transgenic mice expressing ChR2 under Thy-1 promoter. Expression of ChR2 was detected in neocortical layer 5 projection neurons and some subcortical structures (*96*). More cell-type-specific expression of ChR was achieved with another transgenic mice line where opsin expression was limited to vesicular glutamate transporter 2 (VGLUT) positive cells in the spinal cord and hindbrain (*97*). As such transgenic animal lines provide a clear advantage of homogeneous opsin expression, it also comes with time and cost shortcomings associated with production and validation of these lines (*76*).

An alternative to the transgenic animal approach, where optogenetic tools are expressed directly, is to use Cre recombinase expressing animal lines. This allows to achieve a cell type specificity and high expression rates of opsins. The cell type specificity is attained by using transgenic animal lines which express Cre recombinase in cells defined by specific promoter; however, here promoter size is not limited by the genetic capacity of virus leading to a wider array of available cell type specificities. Virus payload itself is constructed using doublefloxed inverted open reading frame (DIO) strategy where opsin gene is placed in inverted orientation and flanked on both sides by two Cre recombinase recognition sequences. When such virus infects a cell expressing Cre recombinase, ORF is inverted and in turn expression of opsin gene commences. Variety of Cre expressing animal lines from such groups as Allen Brain Institute for Brain Science, Jackson Laboratory, and Gene Expression Nervous System Atlas

(GENSAT) provides the possibility to gain optogenetic control on wide range of neuron types in freely moving animals (*76, 78, 88, 90, 98*).

**Projection Targeting**

Another set of strategies for delivering optogenetic tools target neurons projecting to a particular brain area are referred to as projection targeting or circuit targeting. One way of doing this is molecular engineering of opsin genes so that they would be expressed together with specific cellular trafficking motifs, leading to targeted opsin expression in dendrites (*99*) or axons (*100*). This allows to recruit neurons according to their wiring, as light excitation / inhabitation can be achieved by delivering light to neuronal projections instead to somata. A more precise approach to target neurons based on their connectivity would be using dual-virus strategy. Synaptic target location could be defined by infecting neurons in the area with the virus carrying Cre recombinase fused with wheat germ agglutinin (WGA) tetanus toxin fragment C (TTC) which can deliver Cre recombinase transsynaptically to connected neurons. The hypothetical projection source is injected with the Cre-dependent virus and then opsin expression would be only observed if the neurons in projection area have received Cre recombinase through synaptic connectivity in the target region (*80*). An alternative to the aforementioned method could be using various viral vectors with anterograde and retrograde transport capabilities, such as rabies virus, HSV, pseudotyped lentiviruses, and even some serotypes of AAV (*76, 78, 88*). Altogether, this allows exploiting optogenetic toolbox also for deciphering neuronal circuit problems.

# 2. MATERIALS AND METHODS

## 2.1 Materials

| Material | Manufacturer |
|---|---|
| Acetic acid | Sigma, USA |
| Benzonase® nuclease | Sigma, USA |
| Bovine serum albumin (BSA) | Sigma, USA |
| Cresyl violet acetate | Sigma, USA |
| D-2-amino-5-phosphonopentanoic acid (AP5) | Bionuclear Scandinavia, Sweden |
| Disodium hydrogen phosphate ($Na_2HPO_4$) | Sigma, USA |
| Ethanol | Kemetyl, UK |
| Formaldehyde | VWR, USA |
| Gelatin | Merck, USA |
| Goat anti-mouse antibody / Alexa Fluor® 488 dye | Invitrogen, USA |
| Goat anti-rabbit antibody / Cy3 cyanine dye | Jackson ImmunoResearch, USA |
| Hydrochloric acid | Sigma, USA |
| Hoechst solution | Life Technologies, USA |
| Human embryonic kidney cell line HEK293 | ATCC, USA |
| Isoflurane | Intervet International, Netherlands |
| Mouse monoclonal NeuN antibody | Millipore, USA |
| Natural goat serum (NGS) | Invitrogen, USA |
| Nitroquinoxaline-2,3-dione disodium salt (CNQX) | Bionuclear Scandinavia, Sweden |
| pAAV-CaMKIIa-hChR2(H134R) plasmid | Provided by K. Deiseroth |
| Pentobarbital | Ås Produksjonslab, Norway |
| Rabbit polyclonal FLAG antibody | Sigma, USA |
| Sodium deoxycholate (SDC) | Sigma, USA |
| Sodium chloride | Sigma, USA |
| Tris(hydroxymethyl)aminomethane (TRIS) | VWR, USA |
| Triton X-100 | Sigma, USA |
| Tween 20 | Thermo Fisher Scientific, USA |

## 2.2 Methods

**Note**

All the procedures for virus preparation: AAV plasmid construction, serotyping, and transfection were performed by Sheng-Jia Zhang; only rAAV2/1 purification step was performed by me. Surgery was also performed by Sheng-Jia Zhang and I did not take any part in it. The aforementioned procedures are still incorporated into the methodical section, as they are essential parts and help to form a full overview of my project. However, these procedures are not explained in detail, except for rAAV2/1 purification.

### 2.2.1 AAV Plasmid Construct and AAV Serotype

ChR2 was chosen as an optogenetic tool to invoke excitation in transduced neurons. Plasmid pAAV-CaMKIIα-hChR2(H134R)-FLAG-WPRE carrying ChR2 gene was constructed. hChR2(H134R) expression is driven by CaMKIIα promoter; two trafficking signals for improved plasma membrane localization were introduced: 20 amino acid trafficking signal DYKDHDGDYKDHDIDYKDDDDK and ER export motif FCYNENEV, both of them derived from Kir2.1 potassium channel (*79, 80*). Between the two aforementioned trafficking signals FLAG tag for immunohistochemical staining was inserted. Also vector contained a woodchuck hepatitis virus posttranscriptional regulatory element (WPRE) and a bovine growth hormone (BGH) polyadenylation signal for enhanced transgene transcription and expression. All of the above-mentioned components were flanked by AAV2 inverted terminal repeats (ITRs). The plasmid was packed into AAV2 virus which was serotyped with AAV1 capsid proteins, producing AAV2/1 serotype.

### 2.2.2 rAAV2/1 Purification

Human embryonic kidney cell line HEK293 was transfected by rAAV2/1. After the transfection, cells were subjected to three freeze/thaw cycles and following the last one centrifuged for 5 min at 4°C 2200 RPM / 974 RCF (Centrifuge 5810R; Eppendorf, Germany). Standard volume of cell culture used for purification was 2 × 25 ml. 1.3 ml of 10% SDC and 6 µl of 250 u/µl benzonase® nuclease were added to each 25 ml tube; tubes were mixed thoroughly and incubated for 1 h at 37°C (mixing every 10 min). After the reaction, tubes were centrifuged for 1 h at 4°C 4000 RPM / 3220 RCF (Centrifuge 5810R; Eppendorf, Germany). Purification of rAAV2/1 was carried out using 1 ml heparin affinity columns (GE Healthcare, UK) with 1 ml/min flow rate (PHD2000 Infusion pump; Instech Laboratories,

USA). Affinity column was equilibrated by 20 ml of binding buffer A (150 mM NaCl, 20 mM Tris-HCl, pH 8.0) and 50 ml of sample supernatant was applied. To wash out impurities and unbound material column was washed with 25 ml of binding buffer B (100 mM NaCl, 20 mM Tris-HCl, pH 8.0). Virus was eluted with increasing NaCl concentrations in 5 steps with elution buffer (i. 1 ml 200 mM NaCl, ii. 1 ml 300 mM NaCl, iii. 2.5 ml 400 mM NaCl, iv. 3.5 ml 450 mM NaCl, v. 2 ml 500 mM NaCl; all buffers contained 20 mM Tris-HCl, pH 8.0); only elution fractions iii, iv, and v were collected.

### 2.2.3 Subjects

8 male Long-Evans rats (~3 months old and weighting 350-450 g at the time of surgery) were used for the experiment. Rats were housed individually in transparent plexiglass cages (45 × 30 × 35 cm) in a vivarium (with controlled temperature and humidity) established ~10 m from the recording room. A reverse 12 hour light/dark cycle was kept in the vivarium and the training or experimental recordings were carried out in the dark phase. The animals were kept at 85-90% free-feeding body weight, whereas water was available *ad libitum*; furthermore, 18-24 h before each training or recording session rats were food deprived. All experimental protocols comply with *Forsøksdyrutvalget* (http://www.mattilsynet.no/fdu/) regulations.

### 2.2.4 Stereotactic Surgery

rAAV2/1 ($1.0 \times 10^{12}$ viral genomic particles/ml) was injected at three locations within the dorsal hippocampus (4.1 mm behind bregma, 2.6 mm lateral to the midline, 3.5 / 2.8 / 2.1 mm below dura). Injection volumes at each location were 0.5-1 µl. During the same surgical procedure the animals were implanted with 125 µm wide optical fibers in the hippocampus and tetrode-optical fiber assembly (optrode) in MEC. Each tetrode bundle consisted of 4 tetrodes cut flat at the same level. Optical fibers in hippocampus were located at three positions: i. in the ipsilateral pyramidal cell layer (or stratum oriens or alveus) of dorsal CA1 (3.8 mm behind bregma, 3.0 mm lateral to the midline, 1.8 mm below dura); ii. in the perforant pathway termination zone of dorsal hippocampus (4.3 mm behind bregma, 2.4 mm lateral to the midline, ~2.6 mm below dura); iii. in the angular bundle region (7.8 mm behind bregma, 4.2 mm lateral to the midline, ~2.8 mm below dura). Tetrodes in MEC were implanted 0.1-0.5 mm in front of the transverse sinus, 4.5-4.7 mm lateral to the midline, 1.6-1.8 mm below dura, and oriented at an 8-20 degree angle in the anterior direction in the sagittal plane. Optical fiber tip was located 500 µm above the tetrode tips in MEC; what is more, 26G cannula was implanted near the optrode in MEC for drug infusion. The tetrodes

were made of 17 μm polyimide-coated platinum-iridium (9:1) wire with platinum-plated electrode tips.

### 2.2.5 Behavioral Training and *in vivo* Recordings

The rats were given 1 week of recovery after the surgery before behavioral training began. After the recovery the animals were trained one time per day to run in an electrically grounded square box (1 m × 1 m × 0.5 m) with black floor and walls. The square enclosure was polarized by a white cue card (21 cm × 30 cm) and completely surrounded by a curtain. The animals were motivated to run around in the square enclosure for 15 min by throwing in crumbs of chocolate-flavoured cereal in a way that the best possible running coverage would be achieved. Behavioral training period continued for at least 1 week or until the rat achieved acceptable running behavior.

There were two types of data collection sessions: either a 2 min session, where the rat moved around on a towel in a large flower pot on a pedestal, or 10-15 min behavioral session in the aforementioned square enclosure. The rat, while resting on the pot, was connected to the recording equipment ("dacqUSB Recording System"; Axona, UK) via the attached head stage amplifier on animal's head. The connecting cables were weight-counterbalanced which allowed unrestricted animal's movement either in the pot or the box. The tetrodes were lowered in 50 μm steps (never more than 100 μm per day) until single units could be isolated and data recording sessions followed. After the experimental procedures were carried out and units did not show any recognizable changes, the tetrodes were lowered further in the same fashion until new neuronal activity was detected.

Recorded signals were amplified 8000-16000 times and filtered using high-pass filter operating between 300 Hz and 7 kHz; triggered spikes were stored at 48 kHz. EEG was recorded from one of the electrodes, amplified 3000-10000 times and low-pass filtered (500 Hz cutoff); EEG was stored at 4.8 kHz. The position of the animal in the square enclosure was tracked by an overhead video camera which recorded the position of two head stage mounted LEDs (separated by ~5 cm); tracking information was sampled at 50 Hz.

### 2.2.6 Spike Sorting, Handling of Position Data, and Generating Firing Rate Maps

Spike sorting was carried out using cluster-cutting software (Tetrode Interface (Tint), Axona, UK). Software generates electrode-pair scatterplots which by default are characterized by

peak-to-trough amplitude. Scatterplots were separated into clusters manually by hand drawn polygons using two parameters: peak-to-trough amplitude and amplitude at user-defined time.

Animal's position was estimated by tracking the LEDs on the head stage. Collected positional data was speed-filtered - only epochs with instantaneous running speed ≥2.5 cm/s were included and position samples separated by 100 cm/s were removed as tracking artifacts; position data with a gap of <1 s was interpolated. The path of the animal was smoothed using boxcar algorithm with a boxcar width of 400 ms (corresponding to 21 × 21 window). Position data was sorted into 2.5 cm × 2.5 cm bins and only sessions with 80% coverage of the square enclosure were used for further analysis.

Firing rate maps were generated by dividing number of spikes in one bin by time spent in that bin. To acquire spike number and time maps used for rate map generation, standard spike number / time maps were smoothed using Gaussian smoothing with 5 × 5 window. The peak rate was defined as highest firing rate of one bin in the firing rate map.

### 2.2.7 Laser Stimulation Sessions

Laser stimulation sessions were executed while the rat was moving around on the towel in the large flower pot. For light delivery optical fiber was used to couple laser setup to the optical cannula mounted on the animal's head stage. Two types of optical fibers were used: either one having numerical aperture (NA) of 0.22 (AFS105/125Y; Thorlabs, USA) or 0.66 (custom made; Polymicro Technologies, USA). 473 nm laser light (473nm Blue DPSS Laser (T3); Shanghai Laser & Optics Century, P. R. China) was used for stimulation at a frequency of 1 Hz for 2 min. Light pulses were 3.5 ms long and delivered light power of ~10 mW from the fiber tip. Animals received one stimulation at MEC and three stimulations at different positions in hippocampus: CA1 area and two perforant pathway projection zones (dorsal hippocampus or angular bundle). After the laser stimulation session, animals were decoupled from laser setup and were allowed to run 10-15 min in the square enclosure for cell type identification.

An additional experiment of drug infusion was performed in several cases. This was done to validate the interpretation that neurons were directly stimulated by light, instead of being stimulated by excitatory neurotransmissions in the recording area. A cocktail of α-amino-3-hydroxy-5-methyl-4-isoxazole-propionic acid (AMPA) and kainate receptor antagonist nitroquinoxaline-2,3-dione (CNQX) and *N*-methyl-D-aspartate (NMDA) receptor antagonist D-2-amino-5-phosphonopentanoic acid (AP-5) was infused to disrupt

glutamatergic neurotransmission at the recording location. CNQX/AP-5 cocktail (3 mM CNQX, 30 mM AP-5, pH 7.2, dissolved in 0.9% saline solution) was infused using 33G cannula (C315I; Plastics One, USA) protruding 0.9 mm beyond the implanted guide cannula. Infusion was driven by a syringe pump (CMA 400 Syringe Pump; CMA Microdialysis, Sweden) at 0.1 µl/min infusion rate with the total infusion volume being 0.5-2 µl. The drug cannula was retracted after the infusion and laser stimulation and recording sessions were continued to monitor the effect of CNQX/AP-5 cocktail.

### 2.2.8 Identification of Photoresponsive Cells

A formal quantitative test was designed to identify photoresponsive cells. The test first shuffled 10000 times the spike times of particular neuron within [-100, 100] ms interval around the light stimulus moment. Then three successive 1 ms bins with the maximum number of spikes during the 100 ms period after the stimulation were identified in the shuffled data. In the same manner, three successive bins were identified in the real data. If the number of spikes in the three-bin block in the real data exceeded the $99.9^{th}$ percentile value of the distribution of spikes' number in the three-bin block in the shuffled data, the cell was counted as a photoresponsive one. The response latency was counted by finding the mean latency of all spikes contributing to this three-bin block.

### 2.2.9 Analysis of Grid Cells

To obtain a value (grid score or "gridness") that would allow us to determine if a particular cell is a grid cell or not, autocorrelogram of the firing rate map must be generated. Pearson product-moment correlation coefficient with corrections for edge effects and unvisited locations was used for the generation of autocorrelograms. The autocorrelation between two fields with spatial lags of $\tau_x$ and $\tau_y$, r ($\tau_x$, $\tau_y$), can be defined as:

$$r(\tau_x, \tau_y) = \frac{n\sum \lambda(x,y)\lambda(x-\tau_x, y-\tau_y) - \sum \lambda(x,y)\sum \lambda(x-\tau_x, y-\tau_y)}{\sqrt{n\sum \lambda(x,y)^2 - \left(\sum \lambda(x,y)\right)^2}\sqrt{n\sum \lambda(x-\tau_x, y-\tau_y)^2 - \left(\sum \lambda(x-\tau_x, y-\tau_y)\right)^2}},$$

where $\lambda$ ($x$, $y$) stands for the average rate of a cell in location ($x$, $y$) and $n$ being the number of pixels in $\lambda$ ($x$, $y$). Autocorrelations were not estimated for spatial lags $\tau_x$ and $\tau_y$ where $n < 20$.

Degree of spatial periodicity (grid score) for each cell was determined by taking a circular sample of the autocorrelogram centered on the central peak, which is later excluded, and comparing rotated versions of this sample. Actually, not only one sample is taken from

the autocorrelogram but multiple ones with the increasing circle radius of 1 bin (i.e. 2.5 cm); after the analysis of each circular sample is done, the one giving the best grid score is being used. Circular samples were rotated in two ways: 60° and 120° to one side and 30°, 90° and 150° to another side. The grid score was then calculated as the minimum correlation at 60° and 120° degrees minus the maximum correlation at 30°, 90° and 150°. Informally, grid score can be looked upon as the minimum difference between any elements in the first group and any of the elements in the second group.

Furthermore, obtained grid scores were compared to the distribution of grid scores from the entire population of MEC recorded cells. Distribution of grid scores was acquired by shuffling recording data from the MEC recorded cells. Shuffling procedure time-shifts the entire spike train fired by the cell by a random interval from 20 seconds into the session to the end of the session minus 20 seconds, with the end of the trail wrapped to the beginning. For a newly generated simulated recording data a firing rate map was constructed which was used to generate an autocorrelogram and a grid score. The shuffling procedure is then repeated 100 times for each recorded cell. This gives a grid score distribution for the shuffled data. If a grid score of a cell of interest exceeded the $99^{th}$ percentile value of the grid score distribution, a recorded cell was counted as a grid cell. Only cells with more than 100 spikes left after speed-filtering were used for this analysis.

### 2.2.10 Analysis of Head-direction Cells

To begin with, polar firing rate maps are required for the analysis of head-direction cells which are generated in a similar manner to positional firing rate maps. Animal's head direction was recorded by tracking the relative position of the two LEDs in the horizontal plane. Polar firing rate map (also known as directional tuning function) was obtained by plotting the firing rate as a function of the animal's directional heading. Map was divided into 3° directional bins smoothed using mean filter with the window size of 15° (2 bins on each side). Firing rate was defined by dividing spike number belonging to the bin by the time spent in the bin. Only the data with all directional bins covered was used for further analysis in order to avoid inhomogeneous sampling.

The degree of the directional tuning was obtained by calculating the length of the mean vector for polar firing rate map. Head-directional cells were defined as those cells with mean vector lengths exceeding mean vector lengths that would be expected by chance in MEC recorded neurons. The chance level was determined in a similar manner as for the grid cell

analysis. The same spike train time-shifting shuffling procedure was used to generate random polar firing maps which in turn were used to calculate mean vector lengths. This procedure was repeated 100 times for each MEC recorded cell to generate the distribution of mean vector length. If a mean vector length of a cell of interest exceeded the 99$^{th}$ percentile value of the mean vector length distribution, the recorded cell was counted as a head-direction cell.

### 2.2.11 Analysis of Border Cells

To evaluate putative border cells border score *b* was calculated which was defined as:

$$b = \frac{c_m - d_m}{c_m + d_m},$$

where $c_m$ stands for a coverage of any wall by a single firing field and $d_m$ being mean firing distance from the nearest wall. Firing field for the border cell was identified as a collection of neighboring pixels covering an area ≥200 cm$^2$ and each pixel having a firing rate that is higher than 0.3 times of the maximum firing rate of that cell. $c_m$ was calculated by dividing the number of the firing field's pixels along one wall by the entire number of pixels along that wall. $c_m$ for a given cell was chosen as giving the maximum coverage of any single field over any of the four walls of the environment. $d_m$ was obtained by averaging the distance of the firing field to the nearest wall; pixels of the firing field were used for this and they were weighed by the firing rate. Weighting was done by normalizing the firing field by its sum over all pixels belonging to the field.

The acquired border score has a range from -1 to +1; -1 means that a cell has central firing field, whereas +1 is obtained for fields that perfectly line up along at least one entire wall. Border cells were defined as those cells with borders scores significantly exceeding border scores that would be expected by chance in MEC recorded neurons. The chance level was determined in a similar manner as for the analyses of grid cell or head-direction cell. The same spike train time-shifting shuffling procedure was used to generate random firing maps which in turn were used to calculate border scores. This procedure was repeated 100 times for each MEC recorded cell to generate mean vector length distribution. If a border score of a cell of interest exceeded the 99$^{th}$ percentile value of the border score distribution, a recorded cell was counted as a border cell.

### 2.2.12 Perfusion

After all experimental recordings were done, food restriction regime for the rats was over and food was available *ad libitum*; electrode position remained unchanged until the perfusion. Before the perfusion rats were weighed to determine pentobarbital dosage. General anesthesia was induced in rats by exposing them to the closed environment with isoflurane gas (few drops of 100% isoflurane solution in a 15 cm × 20 cm × 20 cm gas chamber). After the rat did not show any signs of consciousness, it received an overdose of 100 mg/ml pentobarbital solution (3 ml of pentobarbital for 600 g rat) injected intraperitoneally in the abdominal area with the 25G needle (Sterican®; B. Braun Melsungen, Germany). The level of anesthesia was monitored by testing toe pinch reflexes. When the rat was in a surgical anesthesia, it was fixed to the perfusion bath by taping its limbs. Chest area was opened to gain access to the rat's heart. A 21G needle (Sterican®; B. Braun Melsungen, Germany) with a running 0.9 % saline solution was inserted to the left ventricle of a still beating heart and a small cut was made in the right atrium to let the blood run out. After ~5-15 min saline solution was replaced by 4% formaldehyde solution (pH 7.4). After another ~10-15 min the rat's head was cut off and soaked in 4% formaldehyde solution for at least 1 h. Then electrodes were turned all the way up, the brain carefully extracted by approaching it from the caudal part of the skull and removing most of the skull bones. Extracted brain was stored in 4% formaldehyde solution.

### 2.2.13 Histology and Immunohistochemistry

The brains were stored at least for 2 days in 4% formaldehyde solution before the sectioning. The brains were mounted onto the microtome holder using mounting medium (Neg -50; Richard-Allan Scientific, USA) and covered with pulverised dry ice (101 Cold Spray; Taerosol, Finland). They were stored for 20-30 min at -21°C and then cut (Microm HM505E; Midwest Lab Equipment, USA) in 30 μm sections in the sagittal plane. Sections were collected into 6-well plate containing 1 × PBS solution and every seventh section was mounted on "gelatin" glass slides (Polysine™; Gerhard Menzel, Germany) (each glass slide was manually covered in 1% gelatin).

Sections mounted on glass slides were used for Nissl (Cresyl violet) staining. Sections were soaked for 2 min in $dH_2O$ and then dehydrated by rinsing (10 dips up and down) in different ethanol concentrations in the following way: 70%, 80%, 90% and 3 times in 100% ethanol. After that, sections are stored for 2 min in 100% xylene for clearing, rehydrated (3 × 100%, 90%, 80%, 70% ethanol) and stored for 5 min in a fixing solution (70% ethanol,

0.005% acetic acid). Then sections are rinsed with water and stained for 5 min on the shaker in Cresyl violet solution (0.001% Cresyl violet in $dH_2O$). Excess color is washed away with running water and dipping in the fixing solution. The sections are dehydrated (70%, 80%, 90%, 3 × 100% ethanol) and soaked for at least 10 min in xylene once more. The sections were cover slipped using the Eukitt® mounting medium (Eukitt®; O. Kindler, Germany). Tetrode recording positions were reconstructed by taking digital pictures (AxioCam MRm, Carl Zeiss, Germany) of the Nissl stained sections. Scanning and measurements were made using MIRAX MIDI software (Carl Zeiss, Germany).

Sections collected into 6-well plate were used for immunostaining. They were washed 3 times for 10 min with 1% Triton X-100 solution (in 1 × PBS). After the washing, sections were stored overnight on the shaker at 4°C in blocking buffer (0.1% Triton X-100, 1% BSA, 5% NGS in 1 × PBS). Reactions with the primary antibodies were carried out in 2 ml of dilution buffer (0.1% Triton X-100, 1% BSA, 1% NGS in 1 × PBS) with 2 µl rabbit polyclonal FLAG antibody (1 mg/ml) and 10 µl mouse monoclonal NeuN antibody (1 mg/ml). FLAG antibody was used to estimate the location of neurons expressing ChR2, whereas NeuN reacts with most neuronal cell types and was used as a background stain. Reactions were left for 2-3 days on the shaker at 4°C. After that, sections were washed for 2 × 15 min and 2 × 30 min in PBST (0.1% Tween-20 in 1 × PBS). Reactions with secondary antibodies were carried out also in 2 ml dilution buffer with 4 µl goat anti-rabbit antibody conjugated with Cy3 cyanine dye (1 mg/ml) and 4 µl goat anti-mouse antibody conjugated with Alexa Fluor® 488 dye (2 mg/ml). Cy3 dye has an emission maximum at 570 nm giving red colour to stained sections and its conjugated antibody binds FLAG primary antibody. Alexa Fluor® 488 dye has an emission maximum at 519 nm giving green colour to stained sections and its conjugated antibody binds NeuN primary antibody. Reactions with secondary antibodies were carried on the shaker at room temperature for 2 h. This was followed with PBST washing (2 × 15 min, 2 × 30 min), mounting sections on “gelatin” glass slides and letting them dry in the dark overnight. Then the sections were soaked for 5 min in 0.002 mg/ml Hoechst stain at room temperature, washed 2 × 30 s in 1 × PBS and for 1 min in $dH_2O$. Hoechst staining was only used for the purpose of focusing when taking digital pictures. Sections were cover slipped using the Eukitt® mounting medium.

# 3. RESULTS

## 3.1 Electrophysiological *in vivo* Recordings

8 male Long-Evans rats were implanted with tetrode-optical fiber assemble in the MEC to record *in vivo* electrophysiological activity of MEC neurons. Tetrode recordings provide an advantage over stereotrode or single electrode recordings, as they allow isolating action potentials of single neurons (referred to as "units") from neuronal ensembles electrical activity. This is achieved by triangulation of distances which is based on the fact that the amplitude of the recorded action potential is a function of distance between the neuron and the electrode (*101*). Isolation of units was carried out with cluster-cutting software. Recorded neuronal activity is visualized by the program by generating electrode-pair scatterplots, where recorded action potentials are plotted in two dimensions according to their distance to two selected electrodes (giving 6 different plots for different electrode pairs in the tetrode). Scatterplots were separated into single units manually by hand drawn polygons using two parameters: peak-to-trough amplitude and amplitude at user-defined time (Fig. 8).

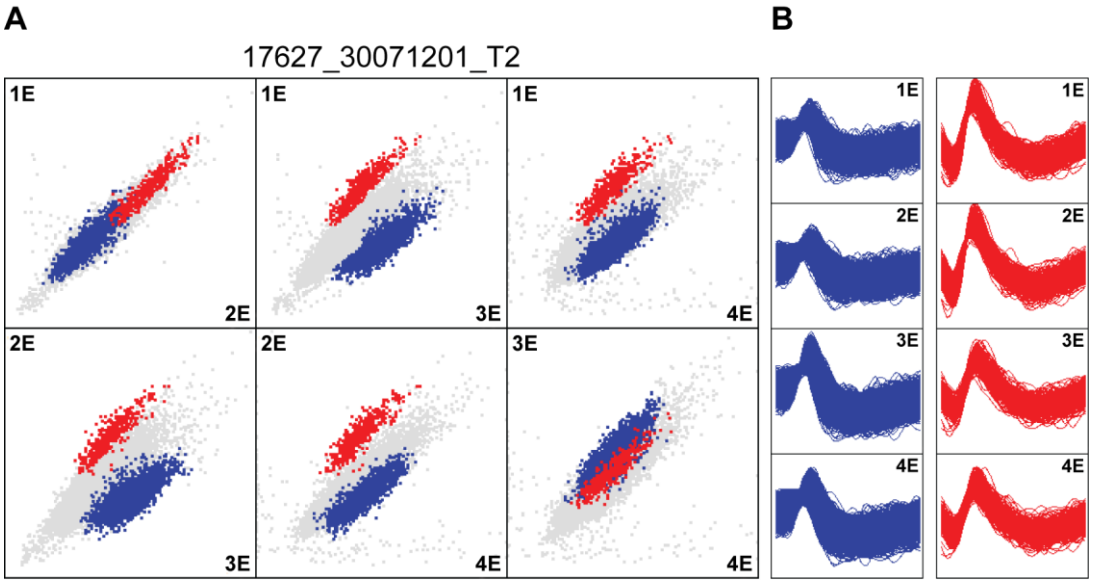


**Fig. 8**. Isolation of single units done by cluster-cutting program. **(A)** Electrode-pair scatterplots of recorded neuronal activity in MEC over 10 min time period. The identifier of the recording session is shown above the scatterplots (17627 stands for the rat number, 30071201 – date 30.07.12 and first recording session, T2 – second tetrode). Each grey dot represents one recorded signal plotted in accordance to its distance to 4 electrodes of the tetrode (1E – 4E). The two single units were identified and separated into the two clusters (blue and red colors). **(B)** The recorded action potentials that belong to the two separate clusters as defined by the two colors in (A). Each rectangle shows the recorded action potential by a single electrode.

Optrode was lowered in steps of 50 μm until neuronal activity could be observed. Then the rats were allowed to run around for 10-15 min in a 1 $m^2$ square enclosure, while the electrical activity in MEC was recorded. After all experimental procedures at particular optrode depth were carried out and neuronal activity did not show any observable changes, optrode was lowered deeper. Besides sampled action potentials, positional data and animal's directional heading were also tracked, which was later applied to identify functional identity of MEC recorded neurons. In total there were 136 cells recorded in MEC. After the experimental recordings were done, rats were transcardially perfused and Nissl staining was performed on their sagittal brain sections to evaluate the final position of tetrodes. Nissl staining confirmed that in all of 8 rats tetrodes were located in superficial layers of MEC (Fig. 9).

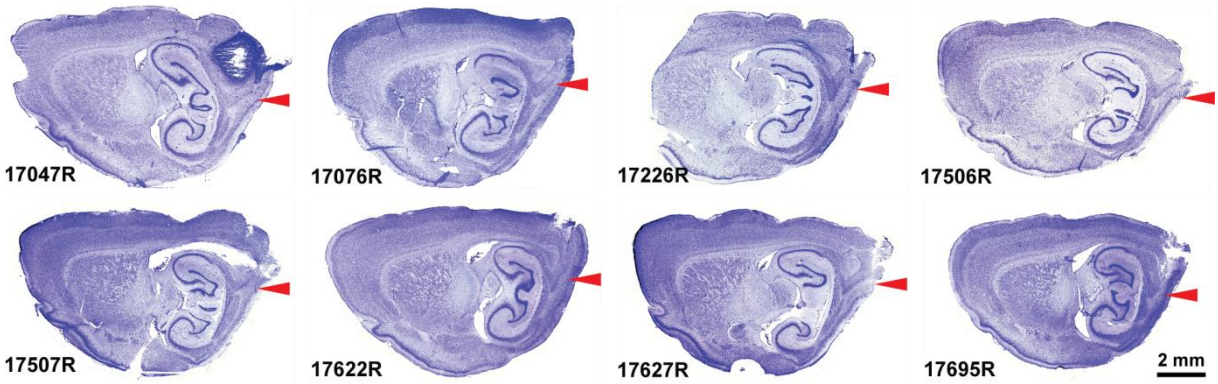


**Fig. 9**. The final locations of tetrodes in MEC. Nissl stained sagital brain sections used to determine the position of the tetrodes (deepest recording position is indicated by a red arrowhead). The number indicates the number of the rat, whereas "R" –a right brain hemisphere; 2 mm scale is indicated on the bottom right image.

### 3.2 Determining the Functional Identity of MEC Neurons

Statistical analyses were performed to confirm that a cell was a grid cell, a head-direction cell or a border cell (see methods section for detailed descriptions). For each MEC recorded neuron grid, head-direction and border scores were calculated. Those scores were compared with a distribution of respective scores from shuffled (randomized) data. If a score from actual behavioral data exceeded the 99$^{th}$ percentile of score distribution of shuffled data, a cell was defined as belonging to a respective functional group. For example, if a calculated grid score for MEC recorded cell exceeded the 99$^{th}$ percentile of the grid score distribution of shuffled data, that cell was counted as a grid cell. Cells that did not satisfy the criteria for grid cells, head-direction cells or border cells, were categorized as unknown principal cells.

## Grid Cells

To define a grid cell, grid score, which evaluates cell's positional firing, was used. Grid score was aqcuired from cell's firing rate map which was used to generate autocorrelogram (Fig. 10B, third panel from the left); essentially, autocorrelogram was applied to evaluate six-fold rotational symmetry of cell's firing during the behavioral task – higher the symmetry more likely that the cell is a grid cell. Grid score (Fig. 10A, top panel) was calculated for each MEC recorded cell. Also the behavioral data was shuffled 100 times for each of 136 recordings resulting in 13600 permutations, which were used to generate grid score distribution (Fig. 10A, bottom panel). 99$^{th}$ percentile of shuffled grid score distribution was 0.393; 34 MEC recorded cells had higher grid scores, therefore, we concluded that those neurons were grid cells. Furthermore, we observed grid spacing gradient along the dorsal-ventral axis within the same rats, with smaller grid spacing in dorsal MEC recording (Fig. 10B, second panel from the left) and bigger grid spacing in ventral MEC recordings (Fig 10C, second panel from the left).

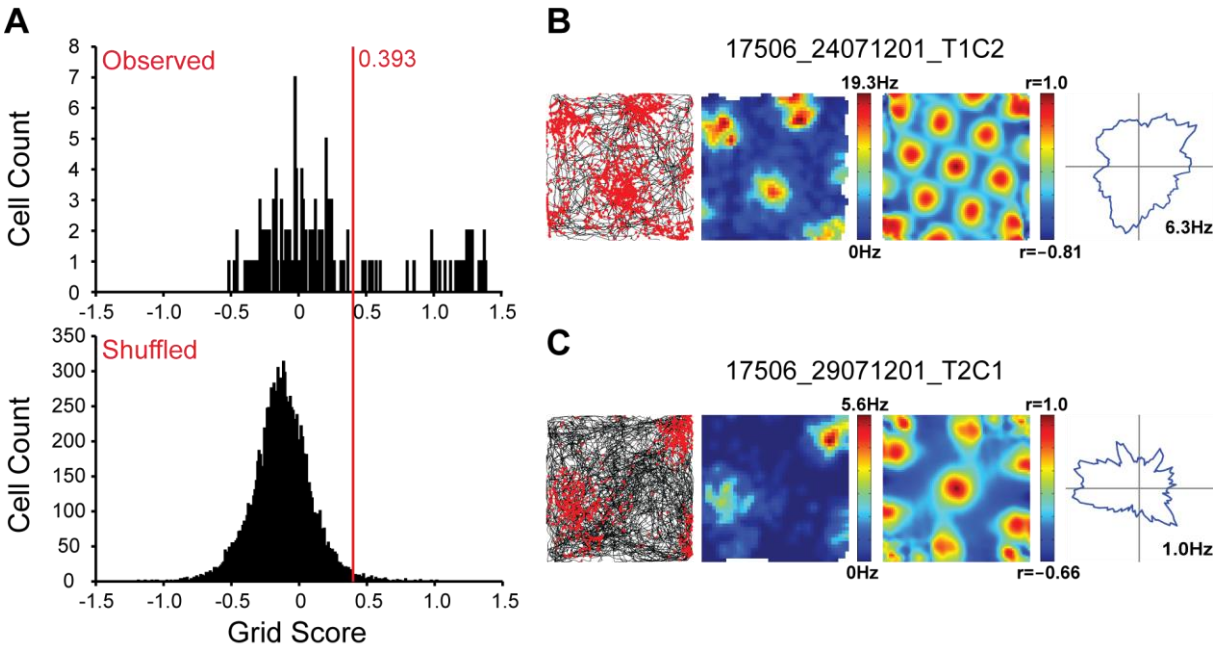


**Fig. 10.** The distributions of grid scores and examples of grid cells. **(A)** Observed (above) and shuffled (below) grid score distributions. Cell count is plotted as a function of grid score. The red line indicates 99$^{th}$ percentile value (0.393) of grid score distribution acquired by shuffling recording data from the MEC recorded cells. If a calculated grid score for a recorded neuron exceeded the 99$^{th}$ percentile value of shuffled score distribution, the cell was counted as a grid cell. **(B)** Firing pattern of a dorsally recorded grid cell with session's number identified on top ("C" stands for a unit number). From left to right: the rat's running path (black line) with the superimposed spike locations (red dot); The map or firing rate with maximum and minimum firing-rate values indicated on the color-coded bar; autocorrelogram extracted from firing rate map with maximum and minimum correlation values

indicated on the color-coded bar (the scale of the autocorrelogram is twice the scale of the firing rate map); polar map showing firing rate as the function of rat's head direction with peak rate indicated. The figure arragment in (B) is kept in (C). Please note multiple firing fields evident in the firing rate map and six-fold rotational symmetry of cell's firing seen in the autocorrelogram. **(C)** Firing pattern of a ventrally recorded grid cell. Please note bigger grid spacing compared to the one observed in (B).

### Head-direction Cells

A head-direction score was used to confirm that a cell was a head-direction cell. Head-direction score is based on polar firing rate map, from which the length of the mean vector is being calculated – cells with longer mean vectors are more likely to be head-direction cells. Observed and shuffled distributions of head-direction scores (Fig. 11A) were generated. According to the aforementioned criteria (99$^{th}$ percentile of shuffled head-direction score distribution was 0.219) we concluded that of 136 MEC recorded cells 27 were head-direction cells. Within our head-direction cell population we observed head-direction cells which were sharply tuned to a certain head orientation (Fig. 11B) as well as head-direction cells with more wider tuning (Fig. 11C).

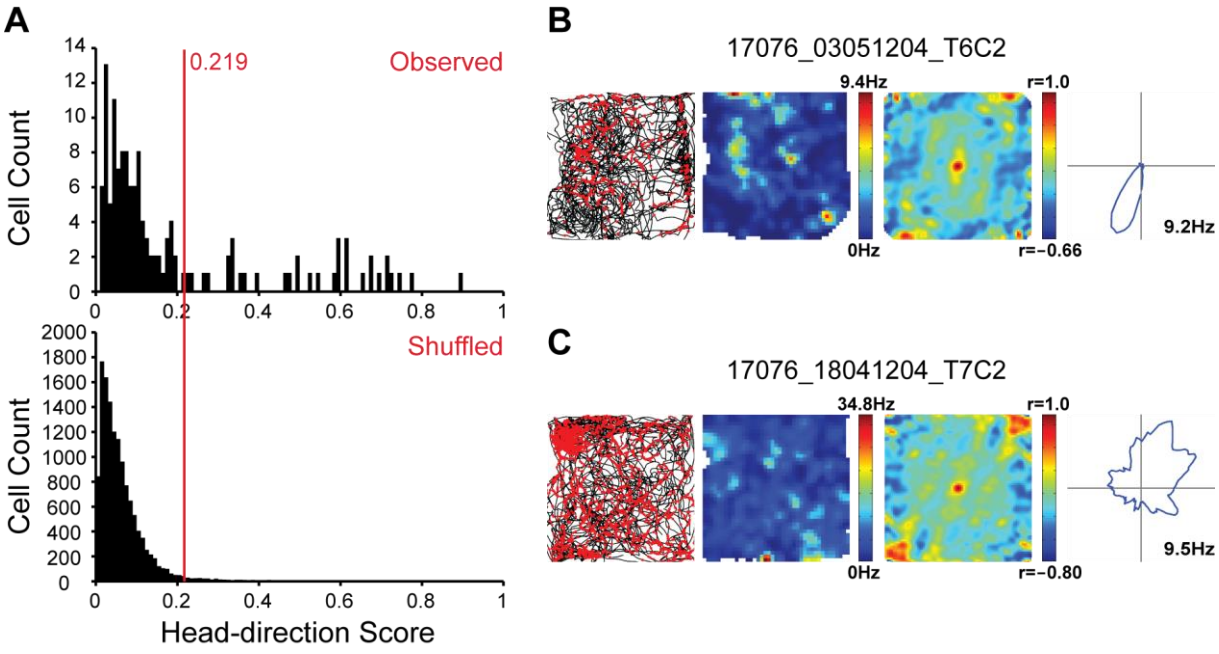


**Fig. 11.** The distributions of head-direction scores and examples of head-direction cells. **(A)** Observed (above) and shuffled (below) head-direction score distributions. The cell count is plotted as a function of head-direction score. The red line indicates 99$^{th}$ percentile value (0.219) of head-direction score distribution acquired by shuffling recording data from the MEC recorded cells. If a calculated head-direction score for a recorded neuron exceeded the 99$^{th}$ percentile value of shuffled score distribution, the cell was counted as a head-direction cell. **(B)** Firing pattern of a head-direction cell with session's number identified on top. From left to right: the rat's running path (black line) with the superimposed spike locations (red dot); firing rate map with maximum and minimum firing-rate values indicated on the color-coded bar; autocorrelogram extracted from firing rate map with

maximum and minimum correlation values indicated on the color-coded bar; polar map showing firing rate as a function of rat's head direction with peak rate indicated. The figure arragment in (B) is kept in (C). Please note the directional modulation of cell's firing seen in the polar map. **(C)** Firing pattern of a head-direction cell with more wider directional tuning (fourth panel from the left).

## Border Cells

In a similar manner, border score for a cell was calculated; basically, border score represents cell's firing pattern in regard of borders of an available environment to an animal during the behavioral task – a cell with the higher border score shows more evident border-associated firing. Observed and shuffled distributions of border scores (Fig. 12A) were generated. According to the aforementioned criteria (99$^{th}$ percentile of shuffled head-direction score distribution was 0.558) we concluded that of 136 MEC recorded cells 12 were border cells (Fig. 12B). In addition, 7 border cells also satisfied the criteria for head-direction cells, meaning they were conjunctive border × head-direction cells (Fig. 12C); however, they were only used once in the cell count and were classified as border cells.

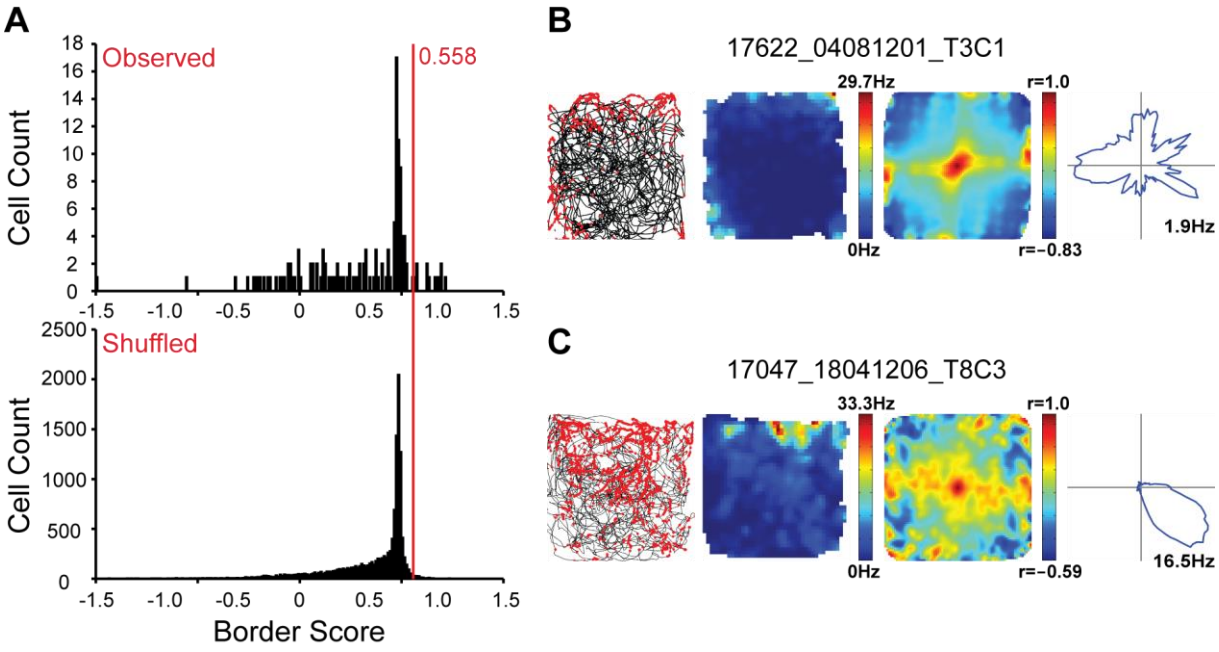


**Fig. 12.** The distributions of border scores and examples of border cells. **(A)** Observed (above) and shuffled (below) border score distributions. The cell count is plotted as a function of border score. The red line indicates 99$^{th}$ percentile value (0.558) of border score distribution acquired by shuffling recording data from the MEC recorded cells. If a calculated border score for a recorded neuron exceeded the 99$^{th}$ percentile value of shuffled score distribution, the cell was counted as a border cell. **(B)** Firing pattern of a border cell with session's number identified on top. From left to right: the rat's running path (black line) with the superimposed spike locations (red dot); firing rate map with maximum and minimum firing-rate values indicated on the color-coded bar; autocorrelogram extracted from firing rate map with maximum and minimum correlation values indicated on the color-coded bar; polar map showing firing rate as a function of rat's head direction with peak rate

indicated. The figure arragment in (B) is kept in (C). Please note border associated firing evident in firing rate map. **(C)** Firing pattern of a conjunctive border × head-direction cell. Please note border associated firing as well as directional modulation (fourth panel from the left).

### Unknown Cells

The cells that did not satisfy criteria for grid cells, head-direction cells or border cells, were categorized as unknown principal cells. We concluded that of 136 MEC recorded cells 34 were unknown cells.

### Interneurons

More subjective parameters were devised for the definition of putative interneurons. Three characteristics were required that the recorded cell would be counted as an interneuron: i. no clear directional or spatial modulation; ii. high firing rate (>5 Hz); iii. short waveform (peak-to-trough width <0.3 ms) (*102*). 29 cells recorded in the MEC met these criteria and were classified as interneurons (Fig. 13). Two cells which had peak-to-trough width of 0.34 and 0.41 ms were still counted as putative interneurons, as they possessed no obvious spatially related firing and had firing rates >10 Hz (these were the only two exceptions considering cell type classification).

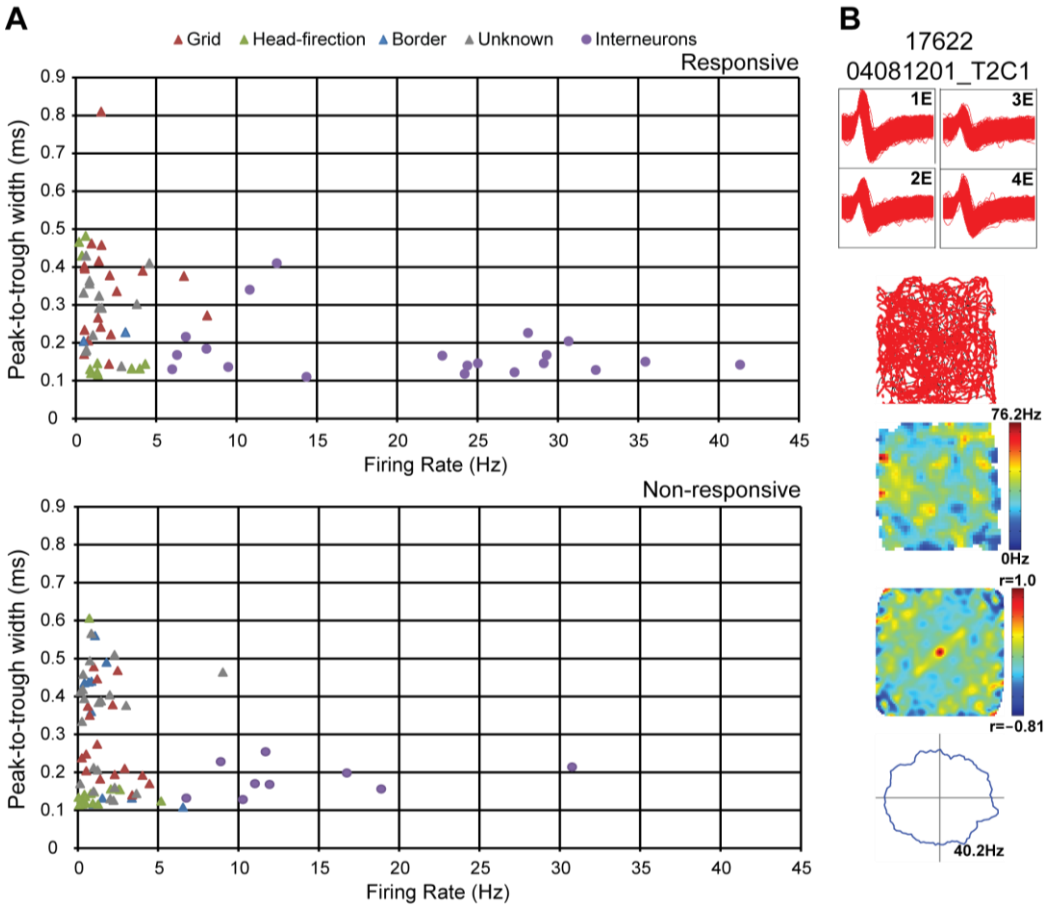


**Fig. 13**. The scatterplots showing the criteria which helped to make a distinction between putative principle cells and putative interneurons (A) and the firing patterns of an interneuron (B). **(A)** Peak-to-trough width vs. firing rate scatterplots. Each cell was plotted according to its peak-to-trough width's (ms) relation to firing rate (Hz). All the light responsive neurons were plotted in the top panel, whereas non-responsive neurons – in the bottom panel (how the cells were classified to responsive / non-responsive will be described in detail in the following chapters). Each triangle or circle represents one cell: the red triangle – a grid cell, the green triangle – a head-direction cell, the blue triangle – a border cell, the grey triangle – an unknown cell, the violet circle – an interneuron. It can be clearly seen that all interneurons fall below 0.3 ms peak-to-trough width and above 5 Hz firing rate (two exceptions are described in the text). The same pattern is valid for both responsive and non-responsive interneurons. **(B)** Firing pattern of an interneuron with session's number identified on top. From top to bottom: action potentials recorded by single electrodes (1E - 4E); the rat's running path (black line) with superimposed spike locations (red dot); the firing rate amp with maximum and minimum firing-rate values indicated on the color-coded bar; autocorrelogram extracted from firing rate map with maximum and minimum correlation values indicated on the color-coded bar; polar map showing firing rate as a function of rat's head direction with peak rate indicated. Please note short waveform and high firing rate of the cell.

## 3.3 Retrograde Transduction of Hippocampus Projecting Entorhinal Neurons

Projection neurons can be targeted by applying a retrograde gene delivery strategy. A particular brain area is being injected by a virus carrying immunohistochemical tag, which can be later exploited to identify transduced neurons in the injection area as well as

retrogradely transduced neurons projecting to the injection area. AAV viral vectors are usually being used for *in vivo* gene delivery as they show low toxicity and a provide long-term gene expression (*103*). Due to wide anatomical distribution, efficient transduction, and the high frequency of retrograde transport AAV2 serotype pseudotyped with AAV1 capsid proteins (producing AAV2/1) was chosen for our research (*91*). rAAV2/1 was packed with pAAV-ChR2-FLAG plasmid; ChR2 was used for optogenetic control (discussed later), whereas FLAG is a non-fluorescent tag. During immunohistochemical staining FLAG tag is bound by a primary antibody which in turn is bound by a secondary antibody conjugated with Cy3 fluorescent dye which is used to identify transduced neurons. ChR2-FLAG transcription was driven by CaMKIIα promoter; construct also contained potassium channel Kir2.1 derived 20 amino acid trafficking signal DYKDHDGDYKDHDIDYKDDDDK and ER export motif FCYNENEV (*79*, *80*) for improved plasma membrane localization. Furthermore, vector contained WPRE and BGH polyadenylation signal for enhanced transgene transcription and expression.

During the same stereotactic surgery when the optrode was implanted in the MEC rAAV2/1-ChR2-FLAG was injected into the dorsal hippocampus. After the experimental recordings were done, the rats were transcardially perfused and immunostaining was performed on their sagittal brain sections to evaluate the levels of transgene expression (Figs. 14, 15). Usually, it takes around 2 to 3 weeks after the hippocampal injections to reach widespread transgene expression that is detectable by immunohistochemical staining (data from our lab).

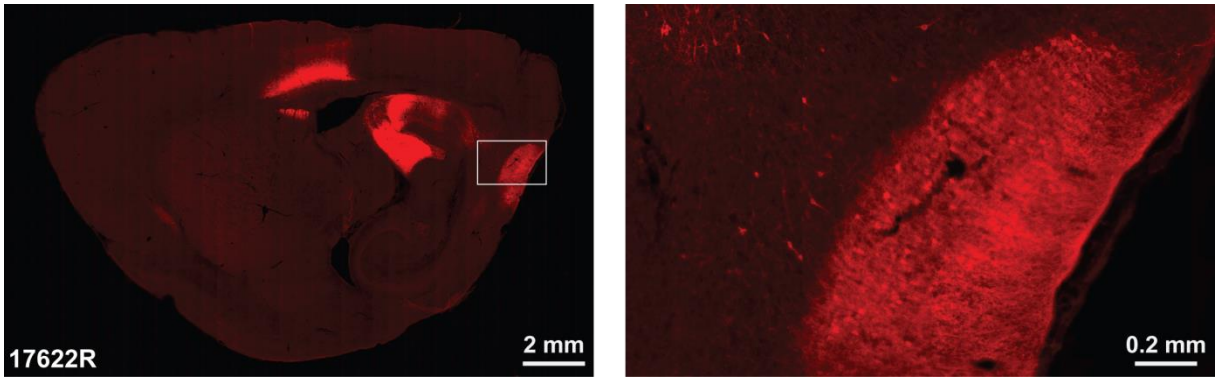


**Fig. 14**. The immunofluorescent images of sagittal brain sections where ChR2-FLAG expressing brain areas are indicated by the bright red fluorescence. During the immunohistochemical staining, FLAG tag is bound by the primary FLAG antibody, which in turn is bound by the secondary antibody conjugated with Cy3 fluorescent dye. From left to rigth, the increasing magnification with the scale indicated on the bottom row, being 2 mm and 0.2 mm, respectively (the right image shows framed area in the left image magnified).

ChR2-FLAG expression was detectable around the injection site in the hippocampus and all hippocampal subregions were transduced (CA1, CA2, CA3); also labeling was observed in dentate gyrus, where perforant path axons of hippocampus targeting MEC neurons can be found. In addition, transgene expression was detected in superficial layers of MEC, whereas FLAG-positive neurons in the deep layers of MEC were not detected or only comparable low numbers of tranduced neurons were detected. What is more, ChR2-FLAG can be seen expressed in soma or dendritic trees of MEC neurons (Figs. 14, 15). By comparing Nissl stained sagital brain sections with immunofluorescent images it can be seen that final tetrode positions were located in the ChR2-FLAG-expressing MEC layers (Fig. 15).

All in all, these results indicate that entorhinal neurons were not transduced by passive difusion of injected virus as only superficial layers of MEC were retrogradely transduced, which is expected from the anatomical data showing that only layer II / III MEC neurons provide direct input to hippocampus (*17*). Thus, the retrograde gene delivery strategy can be applied to tag entorhinal neurons projecting to hippocampus and hopefully gain optogenetic control over them.

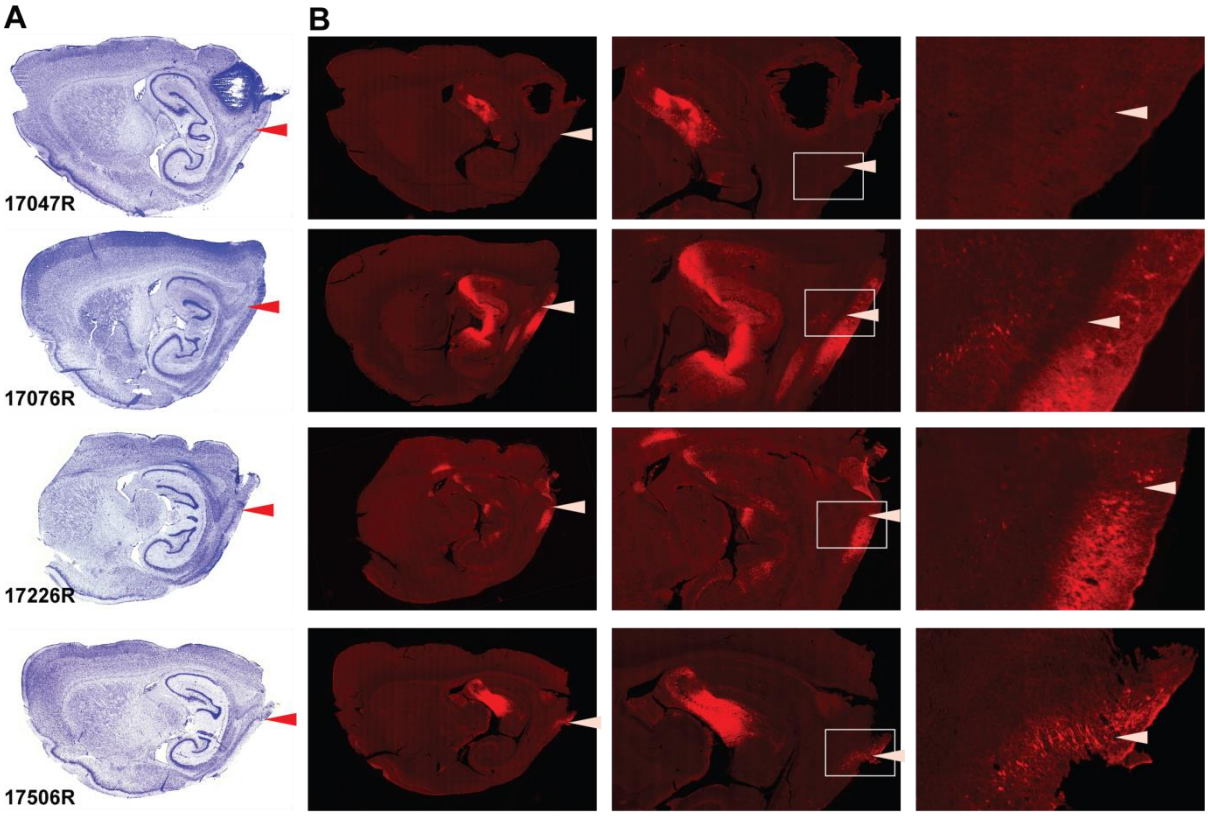

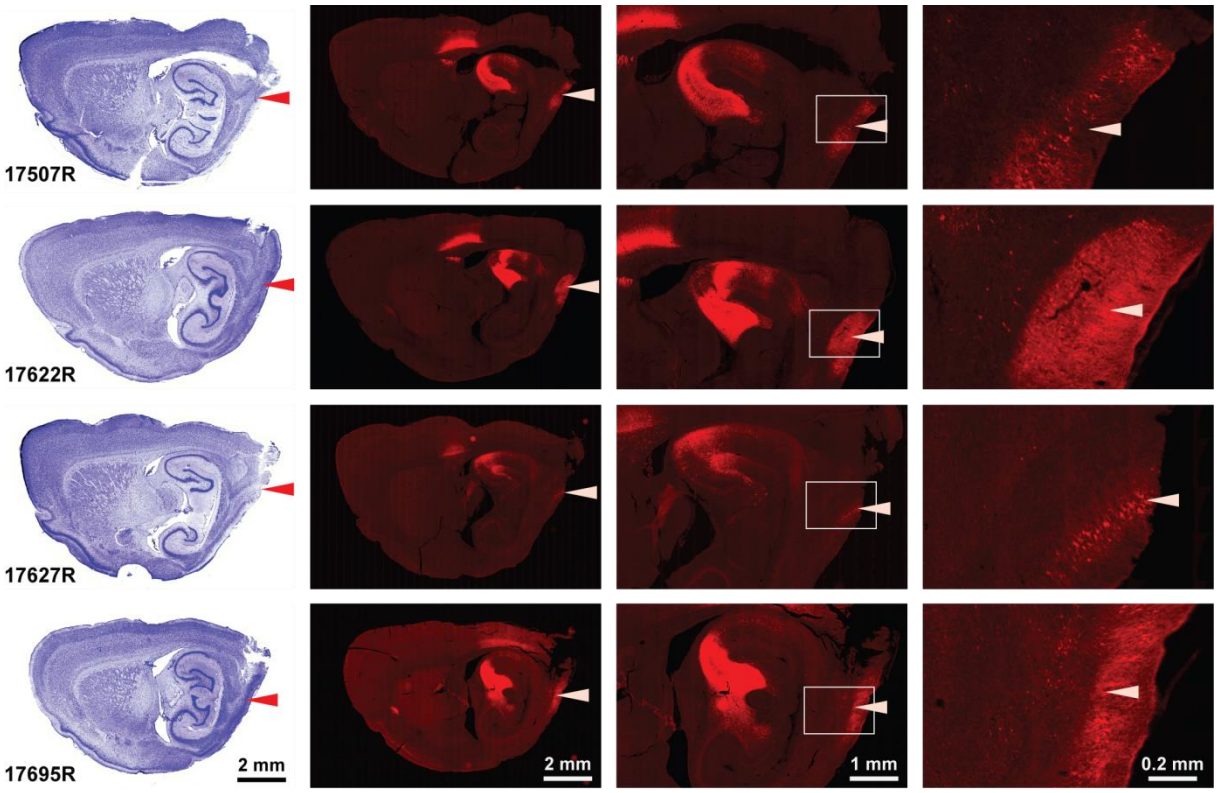


**Fig. 15**. The final locations of tetrodes and ChR2-FLAG expression in hippocampus and MEC. **(A)** Nissl stained sagital brain sections used to determine the position of the tetrodes (deepest recording position is indicated by a red arrowhead). The number indicates the number of the rat, whereas "R" –a right brain hemisphere; 2 mm scale is indicated on the bottom picture. **(B)** Immunofluorescent images of sagittal brain sections where ChR2-FLAG expressing brain areas are indicated by bright red fluorescence. Immunofluorescent images correspond to the adjacent brains in (A); deepest recording position is indicated by the white arrowhead. From left to rigth, increasing magnification with scale indicated on the bottom row, being 2 mm, 1 mm, and 0.2 mm, respectively (the most right image shows framed area in the middle image magnified). Please note that tetrodes were located in the MEC areas also expressing ChR2-FLAG.

## 3.4 Photoexcitation of Hippocampus Projecting MEC Neurons

### 3.4.1 Identifying Light-Responsive MEC Neurons

Optogenetic approach was used to identify MEC neurons with direct projections to the hippocampus. As mentioned previously, MEC neurons with projections terminating on hippocampus region have been tagged by injecting rAAV2/1-ChR2-FLAG into dorsal hippocampus. Viral payload was succesfully transported retrogradely to the superficial layers of MEC (Fig. 7), which should have introduced optogenetic control (photo-excitation) over ChR2-expressing MEC neurons. After the functional identity of MEC neurons have been determined during the behavioral task, the same MEC neurons could be tried to be stimulated by shinning ChR2-activating blue (473 nm) light (*78*). If particular cells showed statistically significant light response (i.e. depolarization leading to action potential) it could be

concluded that: i. those cells have direct projections to the hippocampus region and are being excited directly as they express ChR2, whose gene was retrogradely transported from hippocampus; ii. or neurons are being excited indirectly by ChR2-expressing MEC neurons with excitatory synaptic connections to the cell of interest.

During the same surgical procedure for hippocampal virus injection, tetrode coupled to optical fiber was impanted in the MEC. Optical fiber was 500 μm above the tip of tetrode, which should allow us to record neurons *in vivo* and at the same time deliver 473 nm light to the same recorded neurons for ChR2 activation (*78, 101*). After the behavioral task was finished and the functional identity of MEC recorded neurons was determined, the rat was put into a large flower pot and optical fibres connected to the head stage for light delivery. A 2 min recording session together with laser stimulation followed; laser stimulation consisted of 3.5 ms 473 nm light pulses delivered at 1 Hz frequency and the delivered light power from the fiber tip was ~10 mW. Whether the recorded neuron was the same neuron which was stimulated by light was judged by comparing the position of isolated clusters in electrode-pair scatterplots and spike waveforms before and during the laser stimulation session (Fig. 16A). If the position of clusters and the appearance of spike waveforms were relatively similar before and during the laser stimulation, it was assumed that the recorded neuron was also the same neuron which was stimulated by the laser. Furthermore, a statistical test was designed to evaluate in a quantative manner whether MEC recorded neurons were responsive to laser stimulation (please see the method section for further information). Recording data acquired during the 2 min laser stimulation session was used for the statistical test. Neuron's of interest spike times were shuffled around the light stimulus moment and the number of spikes in a 3 ms time window were compared between the real and shuffled data. If the number of spikes in the most-active time window in the real data exceeded the $99.9^{th}$ percentile value of the number of spikes in the most-active time window in the shuffled distribution of spike times, the cell was counted as a light responsive one. Two parameters of light responsive cells should be mentioned as they were of major importance in further analysis: number of evoked spikes and response latency (Fig. 16B). Number of evoked spikes was defined as the number of recorded action potentials in a 3 ms bin (the 3 ms bin with the highest number of recorded action potentials after the light pulse was chosen). Response latency was determined by finding the mean time which is required to evoke an action potential after the light pulse; spike times of evoked action potentials in 3 ms bin were used.

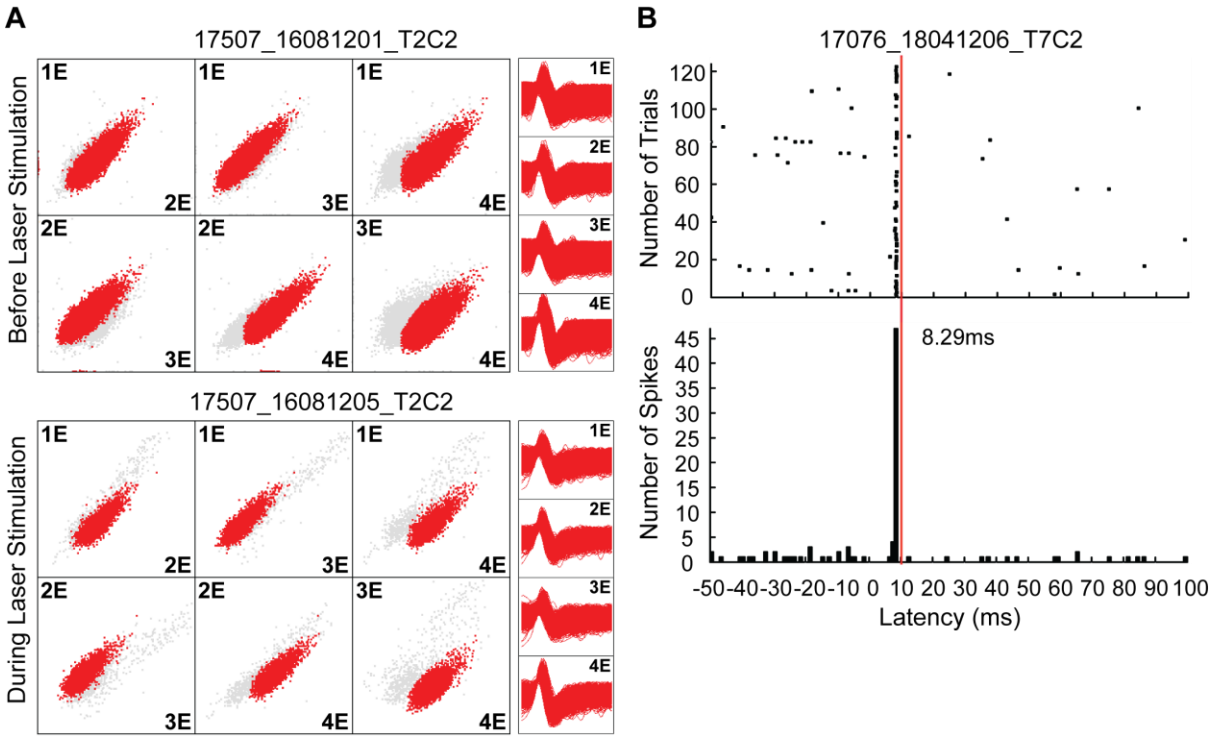


**Fig. 16.** The response of the MEC recorded neuron to laser stimulation. **(A)** Electrode-pair scatterplots of neuron before (top) and during (bottom) laser stimulation session. "Before" session was recorded over 10 min period while the rat was running in the square enclosure, whereas for the "during" session data was acquired over 2 min period with the rat being in the large flower pot. As can be seen from the bottom scatterplots and waveforms, the laser stimulation did not introduce any recognizable changes in the location of clusters or waveform compared to the "before" session and it was assumed that the same cell was recorded and stimulated by the light. **(B)** The spike raster (top) and the spike histogram (bottom) showing the distribution of spike before and after the laser stimulation. The red line indicates 10 ms time stamp shown for the convenience of comparing spike raster and spike histogram and as the reference time for all laser stimulation sessions. In the spike raster each black dot represents the recorded action potential from the cluster in (A). Two coordinates represent the position of each action potential: the number of the trial when the action potential was recorded on *y* axis (each row represents 1 s stimulation period, adding up to ~120 trials for 2 min stimulation session of 1 Hz stimulation) and the [-50, 100] s time interval around the laser stimulation moment. Laser was on from 0 to 3.5 ms. In the spike histogram, the number of spikes is ploted in accordance to their firing lattency around the laser stimulation moment. It can be clearly seen that the recorded neuron has a fixed firing latency at 8.29 ms.

After the statistical analysis it was concluded that of 136 MEC recorded neurons 64 were resposive to laser stimulation in MEC (47.1% of recorded neuron population). Of those 64 light responsive neurons 44 were putative principal cells and 20 were putative interneurons (Fig. 17D and fig. S5). Of 44 light responsive putative principal cells 18 were grid cells (Fig. 17A and fig. S1), 11 – head-direction cells (Fig. 17B and fig. S2), 2 – border cells (Fig. S3), and 13 – unknown cells (Fig. 17C and fig. S4). Altogether, these results suggest that combined optogenetic-electrophysiological approach might be applied to determine functional identity of hippocampus projecting MEC neurons. However, these results alone do not

eliminate the possibility that the obtained latencies are due to indirect stimulation of MEC neurons. As mentioned previously, observed photoresponses could be evoked by synaptic stimulation arising from other cells expressing ChR2 in the illuminated area or even it could be hippocampal axons projecting to MEC. Therefore, further experiments and analyses were required to validate the true identity of MEC neurons with direct connections to hippocampus.

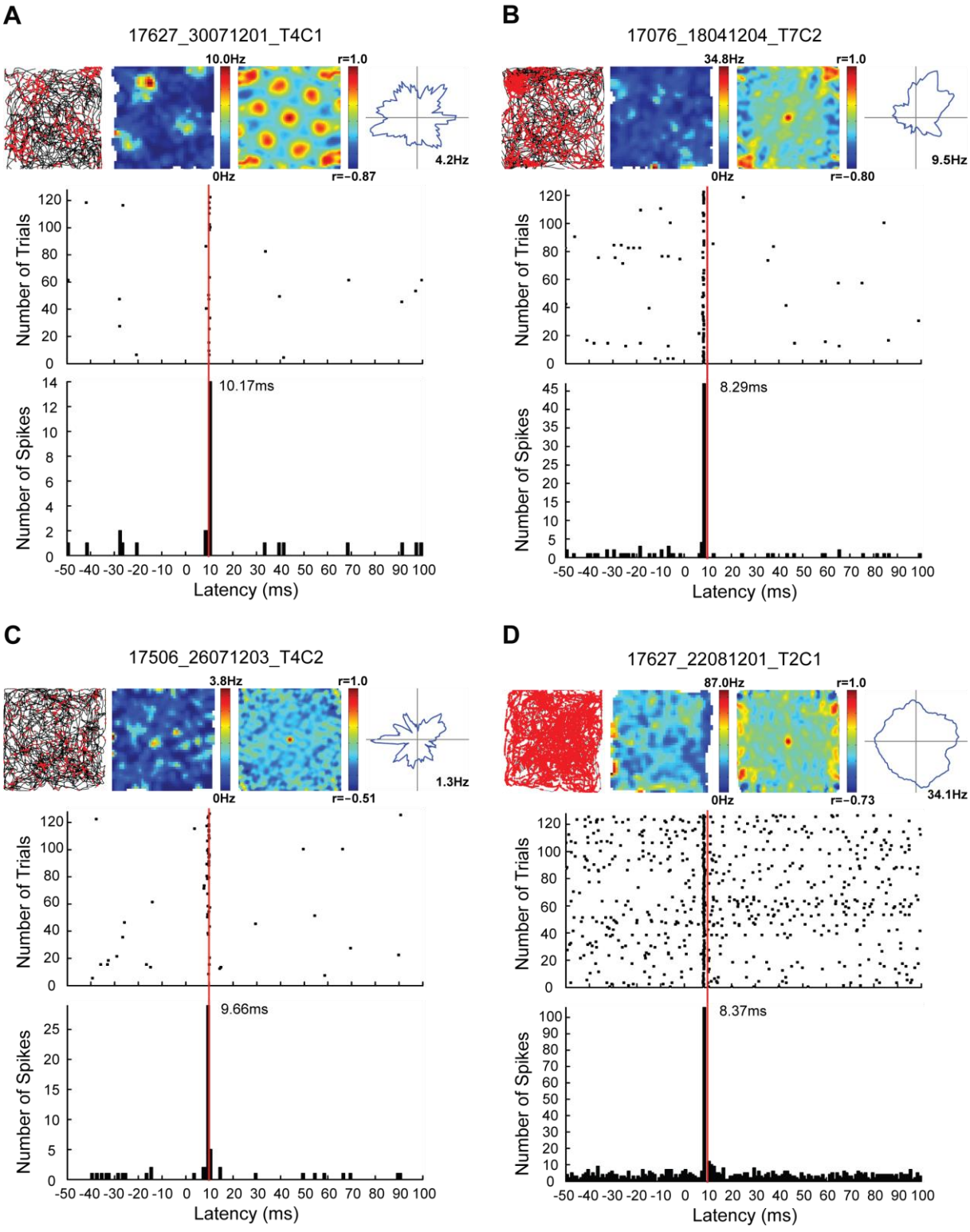

**Fig. 17.** The examples of light-responsive MEC cell types. **(A)** The firing patterns of light-responsive grid cell. The session number is identified on top. Top section, from left to right: i. the rat's running path (black line) with the superimposed spike locations (red dot); ii. firing rate map with maximum and minimum firing-rate values indicated on the color-coded bar; iii. autocorrelogram extracted from firing rate map with maximum and minimum correlation values indicated on the color-coded bar; iv. polar map showing firing rate as a function of the rat's head direction with peak rate indicated. Middle section: spike raster showing spike distribution before and after laser stimulation. Bottom section: spike histogram corresponding to the spike raster with response latency indicated (red line corresponds to 10 ms time stamp). This figure layout is kept throughout (B-D). **(B)** Firing patterns of light-responsive head-direction cell. **(C)** Firing patterns of light-responsive unknown principal cell. **(D)** Firing patterns of light-responsive interneuron.

### 3.4.2 Direct vs. Indirect Photoexcitation of Principal Cells

Differences in response latency can be used to distinguish direct and indirect photoexcitation. The cells which were stimulated directly by light should possess minimal response latencies compared to indirectly activated cells, which should demonstrate longer response times. If a neuron is already expressing ChR2 in its plasma membrane, the fastest way to evoke a light-dependent action potential in it is to activate its ChR2 channels, whereas the synaptic activation arising from neighboring light responsive cells with synaptic connections to the cell of interest would take additional time for signal transduction.

When looking at response latencies of principal cells in different sessions or animals, it can be seen that there is a minimal variation within the data acquired at different times or different subjects and for all principal cells was 10.06 ± 0.27 ms (mean ± SEM) (Figs. S1-4). Furthermore, comparing response latencies of different functional cell types, it is also obvious that they follow a similar trend (Figs. S1-4). Response latency between functional cell types also showed minimal variation (except for border cells, which is due to small sample size and putative indirect excitation): 10.30 ± 0.39 ms being for grid cells, 9.17 ± 0.22 ms – head-direction cells, 14.91 ± 1.64 ms – border cells, and 9.74 ± 0.34 ms – unknown cells (Fig. 18).

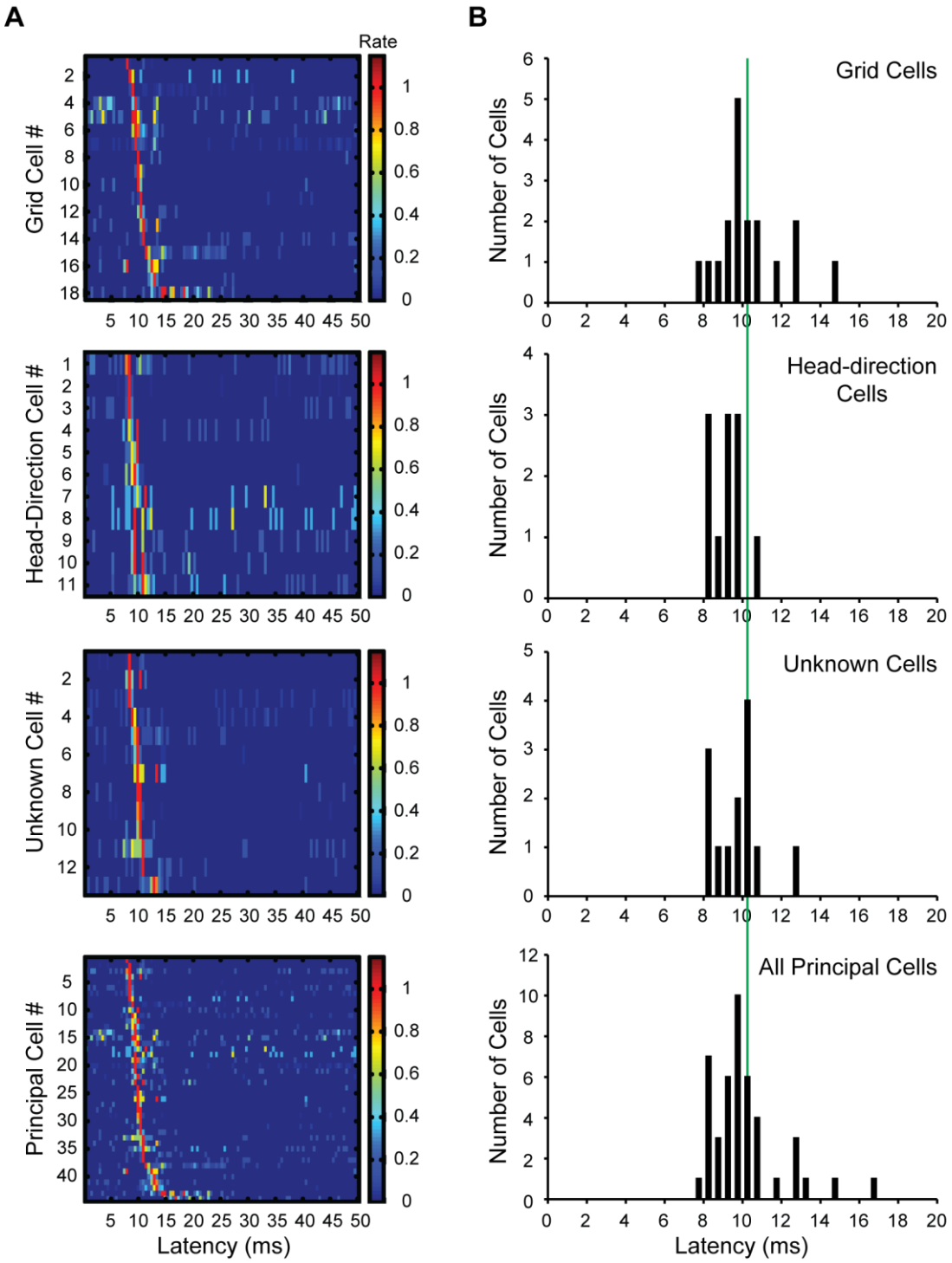


**Fig. 18.** The distribution of the firing latencies of all photoresponsive principal cells recorded in MEC. **(A)** The color-codded spike rasters of MEC recorded light-responsive principal neurons (from top to bottom: grid cells, head-direction cells, unknown cells, and all principal cells). The spike rasters show the color-coded firing rates of particular cells as the function of time after the laser stimulation. Each row in the spike raster corresponds to one cell and all the cells in one spike raster are ordered according to increasing peak response latencies; response latencies are divided into 0.5 ms time bins. Firing rates are normalized to a peak firing rate and the color scale is shown on the right. **(B)** Response latency histograms of MEC recorded light-responsive principal neurons (from top to bottom: grid cells, head-direction cells, unknown cells, and all principal cells). Each histogram shows the distribution of peak response latencies (in 0.5 ms time bins). The green line indicates average

response latency (10.06 ± 0.27 ms) for all principal cells. Spike raster and response latency histogram of responsive border cells are not shown due to small cell count (n = 2). Both from spike rasters and latency histogram it can be clearly seen that response latency shows minimal variation across different principal cell types.

Also it should be noted that short response latencies with single peak response dominated the acquired data, whereas delayed latencies and multiple peak responses were only observed in exceptional cases. Cases of multiple peak response (Fig. 19) are of special interest, as the shorter response latencies represented in some of these cases could correspond to the direct excitation and the remaining multiple response peaks could arise from synaptic activation.

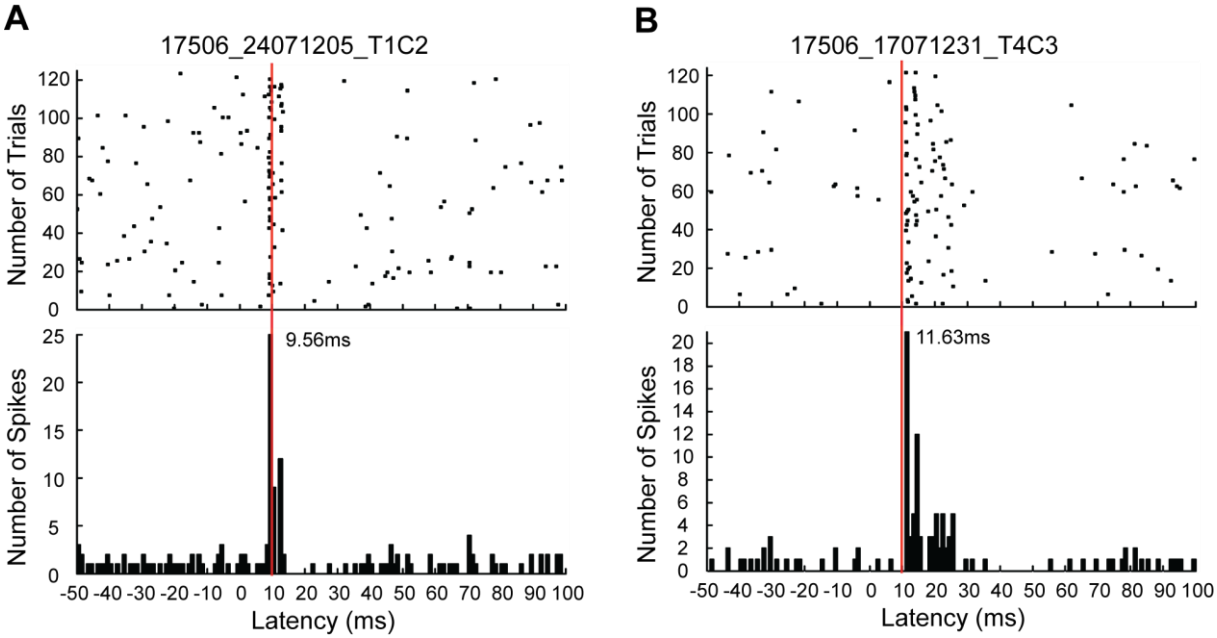


**Fig. 19.** Two examples of light-responsive principal cells with multiple peak responses. **(A)** Spike distribution of light-responsive grid cell with three peak response. The spike raster (top) and the spike histogram (bottom) are shown. In the spike histogram mean response latency is indicated and the red line corresponds to a 10 ms time stamp; laser light was shone from 0 to 3.5 ms. Three peaks are seen in the spike histogram. The first peak (~25 evoked spikes) could correspond to the direct excitation, whereas the next two (both ~10 evoked spikes) could arise from the synaptic activation. Figure layout is kept in (B). **(B)** The spike distribution of light-responsive grid cell with multiple peak response. Multiple peaks are seen in spike histogram. The first peak (~20 evoked spikes) could correspond to direct excitation, whereas the following ones (~12 and ~4 evoked spikes) could arise from synaptic activation.

To evaluate the similarity of short response latencies between different functional principal cell types, $10^{th}$, $20^{th}$, and $50^{th}$ percentile values were compared; these percentiles were chosen, as they contained latencies that could be considered short enough to be elicited by direct light stimulation. If a non-integer rank value was encountered during percentile

calculation, percentile was computed by linear interpolation between the two closest ranks; border cells were excluded from these calculations due to small sample size (n = 2). $10^{th}$, $20^{th}$, and $50^{th}$ percentiles for grid cells were 8.43 ms, 9.12 ms, and 9.91 ms, respectively; head-direction cells – 8.23 ms, 8.30 ms, 9.19 ms; unknown cells – 8.22 ms, 8.32 ms, 9.9 ms. Corresponding percentile values between different light-responsive functional cell types were similar; therefore, it could be concluded that directly activated cells were present in grid, head-direction, and unknown cell type populations. Also we looked at how symmetric was the latency distribution of individual cells from different functional cell type categories. Skewness values were calculated for every functional group: 0.16 ± 0.26 for grid cells, -0.24 ± 0.53 - head-direction cells, and -0.34 ± 0.41 – unknown cells. Then one sample *t* test was used to determine if the acquired data differed from symmetrical latency distribution (skewness value of 0). We observed no significant (chosen cut-off value used throughout the study for statistical significance was $P < 0.05$) difference between the acquired data and non-skewed distribution (grid cells – $t(17) = 0.62$, $P = 0.547$; head-direction cells - $t(10) = -0.46$, $P = 0.652$; unknown cells - $t(12) = -0.82$, $P = 0.428$). The lack of positive skew indicates that response times for all functional cell types were distributed around short response latencies and most of the cells showed only one peak latency and were probably activated directly. What is more, on the basis of the similarity of lower percentile response latencies between different groups, it could be suggested that all principal cell types (except border cells) in MEC have direct projections to hippocampus.

### 3.4.2 Direct vs. Indirect Photoexcitation of Interneurons

Then we looked into the response latencies which were acquired from putative interneurons. In total, there were 29 recorded interneurons and 20 of those were responsive to laser stimulation (Fig. 18). This was expected, as in a recent study it has been shown that in MEC there exist GABAergic neurons with projections to hippocampus (*104*). However, when looking at response latencies of light-responsive interneurons it is obvious that the data spread is wider compared to that of light-responsive putative principal cells (Fig. S5 and fig. 20).

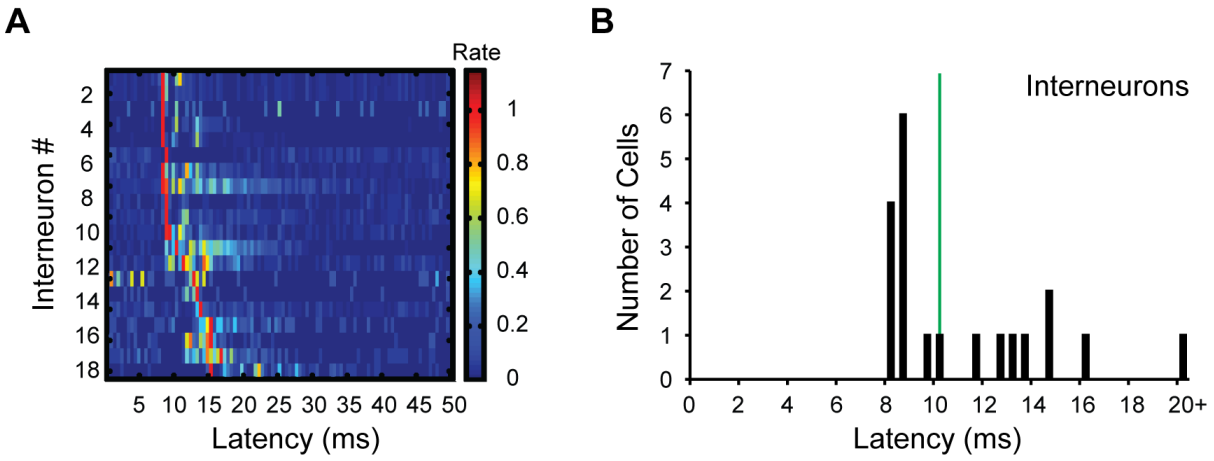


**Fig. 20.** The distribution of firing latencies of all photoresponsive interneurons recorded in the MEC. **(A)** The color-coded spike raster showing firing rates of particular cells as the function of time after the laser stimulation. Firing rates are normalized to a peak firing rate and color scale is shown on the right. **(B)** Response latency histogram showing distribution of peak response latencies. Green line indicates average response latency (10.06 ± 0.27 ms) for all principal cells in Fig. 18. Both from spike raster and latency histogram it can be clearly seen that response latency is positively skewed.

A peculiar property can be observed when looking at the firing latencies of interneurons – there is a 1 ms "step" in a somewhat gradual response latencies increase. This "step" exists between 10 ms and 11 ms responses (from 10.42 ms to 11.67 ms). After the 11 ms mark response latencies increase in a steeper fashion. The same thing can be also seen in principal cell response latency distribution (a "step" from 10.71 ms to 11.63 ms). This 11 ms limit can be looked upon as a putative diving line between direct / indirect excitation. More than half of interneurons (12 out of 20) still retained short firing latencies (<11 ms) similar to principal cells; nonetheless, 8 of recorded interneurons had mean firing latencies higher than 11 ms. Firing latency of interneurons was 11.26 ± 0.82 ms, whereas for principal cells it was 10.06 ± 0.27 ms; however, according to two sample *t* test there was no statistically significant difference between the firing latencies of interneurons and principal cells ($t(62) = -1.38$, $P = 0.180$). Furthermore, response latency distribution within individual interneurons showed significantly more pronounced skew (-0.42 ± 0.11; $t(19) = -3.91$, $P = 0.001$). This observable skew could be related to more frequently encountered multiple peak response latencies (Fig. 21).

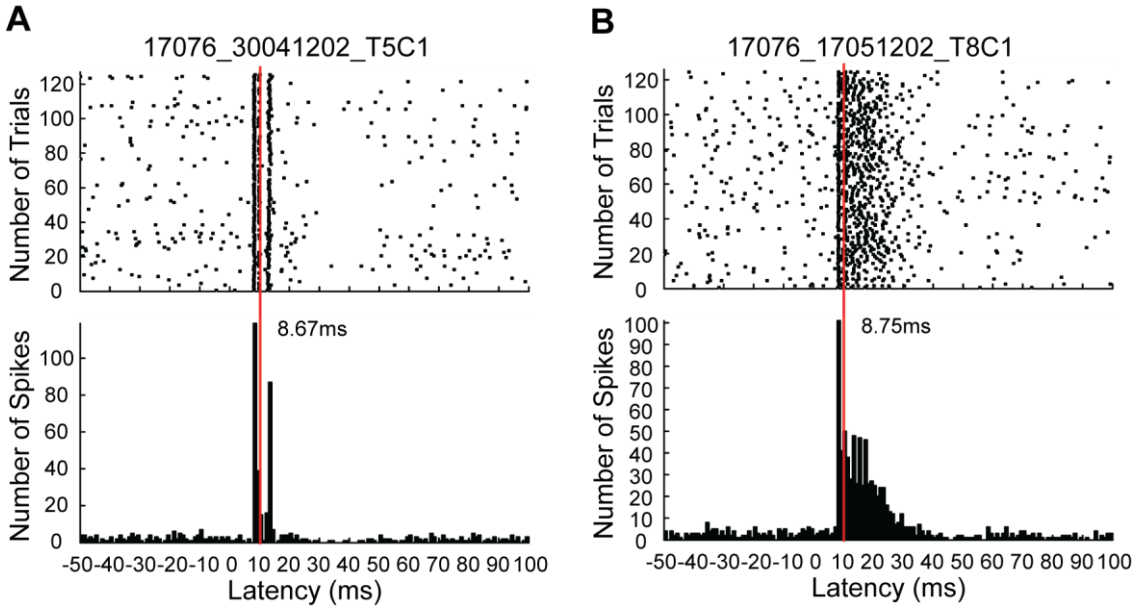


**Fig. 21.** Two examples of light-responsive interneurons multiple peak responses. **(A)** Spike distribution of light-responsive interneuron with double peak response. Spike raster (top) and spike histogram (bottom) are shown. In the spike histogram mean response latency is indicated and the red line corresponds to a 10 ms time stamp; laser light was shone from 0 to 3.5 ms. Two peaks are seen in spike histogram. First peak (~120 evoked spikes) could correspond to direct excitation, whereas next one (~80 evoked spikes) could arise from synaptic activation. Figure layout is kept in (B). **(B)** Spike distribution of light-responsive interneuron with multiple peak response. Multiple peaks are seen in spike histogram. First peak (~100 evoked spikes) could correspond to direct excitation, whereas next multiple ones (~50 and ~30 evoked spikes) could arise from synaptic activation.

Latter cases, in a similar manner to putative principal cells with multiple peak responses, could be seen as the arguments for distinguishing direct vs. indirect response latencies in putative interneurons. Altogether, these results indicate that recorded light-responsive interneuron population contained some cells with direct projections to hippocampus together with other neurons which were also photoexcited indirectly through excitatory connectivity within the MEC.

### 3.5 Probing the Difference between Direct and Indirect Photoexcitation

To evaluate differences in response latencies three different approaches were used: i. laser stimulation was carried out in the hippocampal CA1 area which holds projections to MEC; ii. laser stimulation was carried out in the hippocampal areas which hold axons of hippocampus projecting MEC neurons; iii. drug infusion in the recording area was carried out to block excitatory neurotransmission.

### 3.5.1 Laser Stimulation in the Dorsal CA1

As a control experiment to distinguish between direct and indirect response latencies we used laser stimulation in hippocampal CA1 area with direct projections to MEC. During the same surgical procedure for virus injection in hippocampus and optrode implantation in MEC, optical fiber was also implanted in the approximate area of ipsilateral pyramidal cell layer / stratum oriens / alveus of dorsal CA1. As the expression of virus payload was extensive throughout hippocampus, the laser stimulation in the aforementioned area of CA1 should evoke action potentials in the hippocampal neurons with excitatory direct projections to MEC (*105*). We reasoned that this should lead to excited neurons located in our recording area of MEC. However, expected firing latencies should be longer, as it would include synaptic transmission from hippocampus to MEC, and in turn would help us to make a more precise distinction between direct and indirect photoexcitation. The laser stimulation session for this control experiment was carried out in the same fashion as for MEC stimulation experiment (2 min session, 473 nm 3.5 ms light pulses at 1 Hz frequency), at the same time recording in MEC. In total, there were 7 CA1-stimulation responsive MEC cells (from 3 different animals), with 4 of those being putative principal cells and 3 being putative interneurons (Fig. 22 and fig. S6). Peak response latencies for these cells varied from 15.75 to 30.18 ms (21.11 ± 2.37 ms) – prominently longer compared to peak response latencies observed in MEC stimulations (putative principal cells - 10.06 ± 0.27 ms, putative interneurons - 11.25 ± 0.82 ms, altogether – 10.43 ± 0.32 ms) (Fig. 23). Two sample *t* test indicates that response latency differences between CA1 stimulations and MEC stimulations (principal cells and interneurons together) were highly significant ($t(69) = -4.46$, $P = 0.004$). Looking at the extended response latencies obtained from hippocampal CA1 stimulations these results are a good indicator to distinguish between synaptically induced (indirect) and direct light responses.

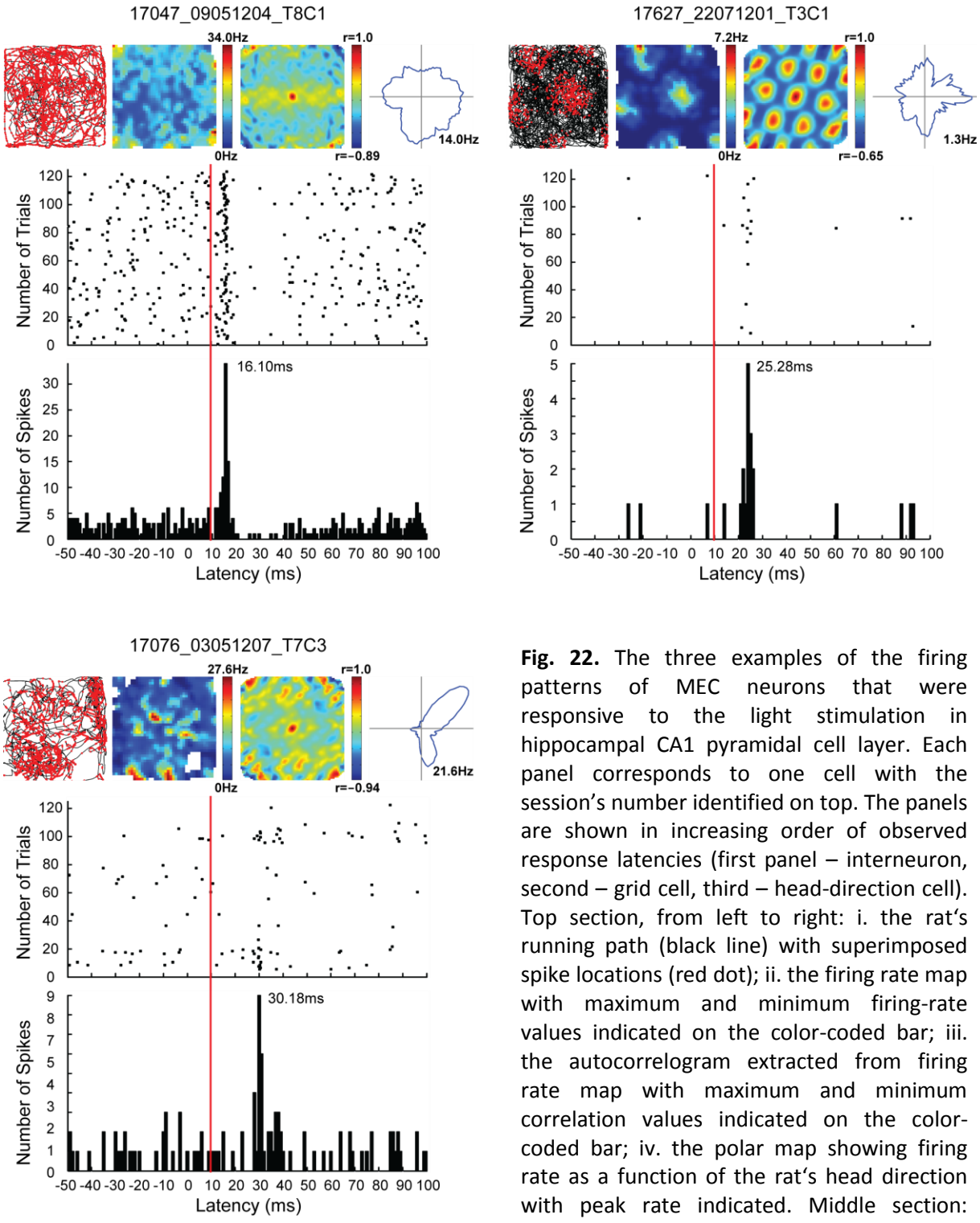


**Fig. 22.** The three examples of the firing patterns of MEC neurons that were responsive to the light stimulation in hippocampal CA1 pyramidal cell layer. Each panel corresponds to one cell with the session's number identified on top. The panels are shown in increasing order of observed response latencies (first panel – interneuron, second – grid cell, third – head-direction cell). Top section, from left to right: i. the rat's running path (black line) with superimposed spike locations (red dot); ii. the firing rate map with maximum and minimum firing-rate values indicated on the color-coded bar; iii. the autocorrelogram extracted from firing rate map with maximum and minimum correlation values indicated on the color-coded bar; iv. the polar map showing firing rate as a function of the rat's head direction with peak rate indicated. Middle section: spike raster showing spike distribution before and after laser stimulation. Bottom section: spike histogram corresponding to the spike raster with response latency indicated (red line corresponds to 10 ms time stamp). Please note consistently longer response latencies compared to the ones observed when the laser was shone in the MEC itself (Figs. 18,

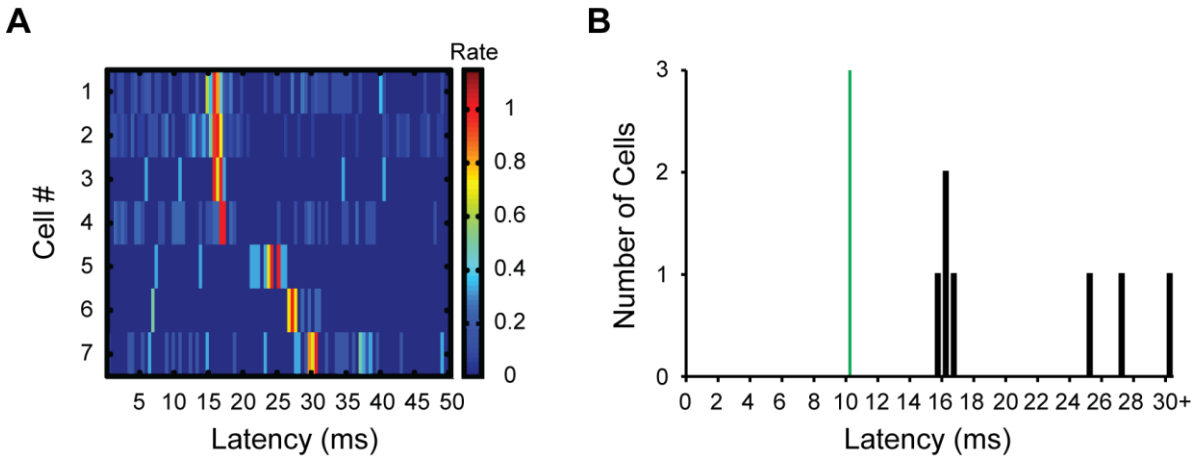


**Fig. 23.** The distribution of firing latencies of all MEC recorded neurons that were responsive to hippocampal CA1 stimulation. **(A)** The color-coded spike raster showing the firing rates of particular cells as a function of time after the laser stimulation. Firing rates are normalized to a peak firing rate and the color scale is shown on the right. **(B)** The response latency histogram showing distribution of peak response latencies. The green line indicates average response latency (10.06 ± 0.27 ms) for all principal cells in Fig. 18. Both from spike raster and latency histogram it can be clearly seen that response latencies were longer compared to the ones obtained from direct MEC stimulations (Fig. 18, 20).

### 3.5.2 Backfiring MEC Neurons

We also performed another set of hippocampal laser stimulations to further elucidate the response latencies of direct excitation. In comparison to previously described CA1 stimulations, here we applied optogenetic backfiring approach recently described by Tye *et al.* (*106*). With the backfiring approach we were aiming to shine laser light on hippocampal areas where axons of hippocampus projecting MEC neurons should be located while still recording in MEC. In this way if such axon would be expressing ChR2, an action potential would be evoked and back propagated to the soma of MEC neuron leading to a recorded action potential in the recording area. However, in such cases observed response latencies should be skewed to the right as the back propagation of action potential along the axon should take more time compared to what is required to evoke action potential when the laser light is shone on the soma itself instead of projecting axon. During the same surgical procedure for virus injection in a hippocampus and optrode implantation in MEC, two additional optical fibers were implanted in hippocampal regions which should hold incoming MEC axons: i. the perforant pathway termination zone within the hippocampus; ii. the angular bundle region where the incoming axons from MEC should be passing through (please see "Materials and Methods" section for the stereotactic coordinates). Laser stimulations were carried as previously described (2 min session, 473 nm 3.5 ms light pulses at 1 Hz frequency) while

recording in MEC. We observed 12 neurons (from 4 different animals) in MEC that showed response to stimulations in the aforementioned hippocampal areas, 10 neurons were responsive to laser stimulation in the angular bundle and 2 neurons – in the perforant path termination zone (Fig. 24 and fig. S7). 9 of those neurons were principal cells (4 grid cells, 1 border cell, and 4 unknown cells) and 3 putative interneurons.

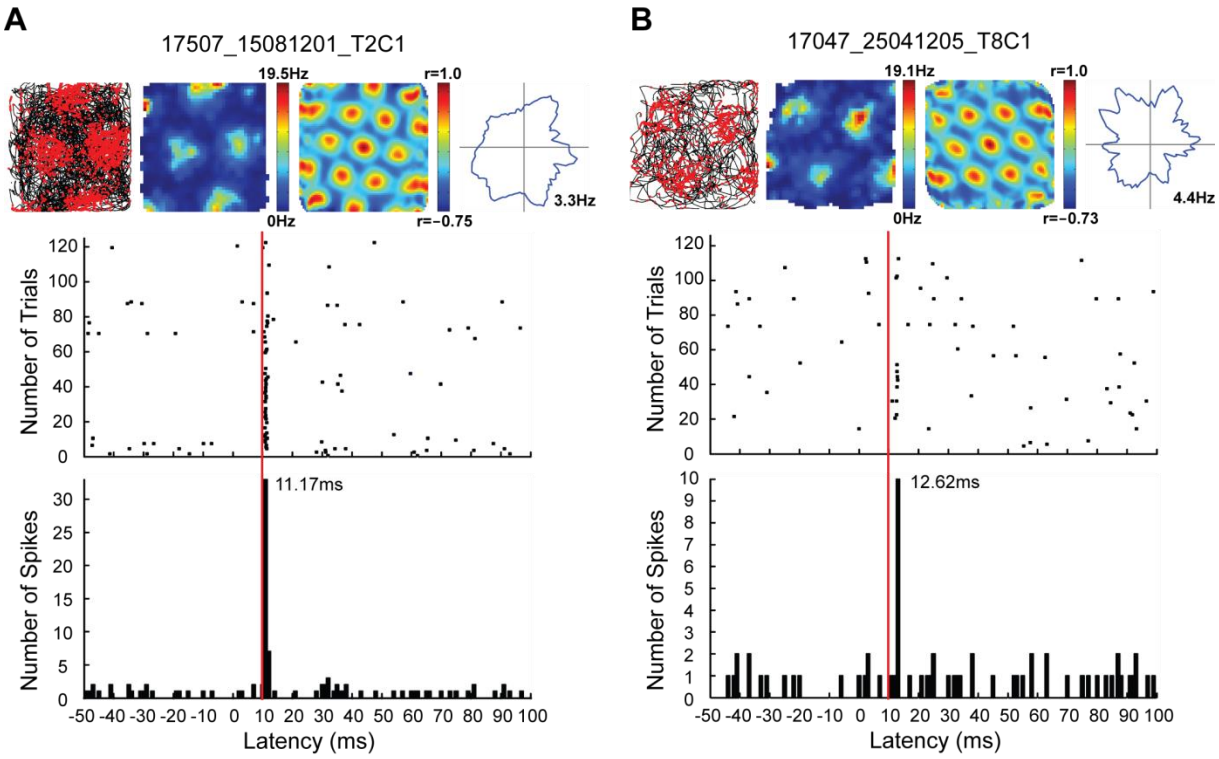


**Fig. 24.** The two examples of firing patterns of MEC recorded neurons that were responsive to laser stimulation in the angular bundle (A) or the perforant path termination zone (B). **(A)** The firing patterns of a grid cell that was responsive to laser stimulation in the angular bundle. Session number is identified on top. Top section, from left to right: i. the rat's running path (black line) with the superimposed spike locations (red dot); ii. the firing rate map with maximum and minimum firing-rate values indicated on the color-coded bar; iii. the autocorrelogram extracted from firing rate map with maximum and minimum correlation values indicated on the color-coded bar; iv. the polar map showing firing rate as a function of the rat's head direction with peak rate indicated. Middle section: spike raster showing spike distribution before and after laser stimulation. Bottom section: spike histogram corresponding to the spike raster with response latency indicated (the red line corresponds to 10 ms time stamp). **(B)** The firing patterns of a grid cell that was responsive to laser stimulation in the perforant path termination zone.

Response latencies did not show much variation (11.78 ± 0.14 ms), the minimum being 11.17 ms and the maximum being 12.62 ms (Fig. 25). Furthermore, the mean response latency acquired from the perforant path termination zone stimulations was 12.61 ± 0.02 ms, whereas angular bundle region stimulations gave the latency of 11.62 ± 0.10 ms. By using two sample *t* test we see that latter latencies are significantly shorter ($t(10) = -4.30$, P =

0.002). This result could be expected as the axons located in the angular bundle are closer to soma of MEC neurons than the ones in the perforant path termination zone and backpropagation of action potential through the projecting axon from the former one should take less time. After comparing response latencies acquired from the backfiring approach (11.78 ± 0.14 ms) with the ones from MEC stimulations (10.43 ± 0.32 ms) using two sample *t* test, we see that the former ones are significantly longer ($t(74) = 3.88$, $P < 0.001$). These results do not only illustrate the differences of response latencies between direct excitation on the soma and the axon, but also give further evidence of different MEC functional cell types projecting to hippocampus.

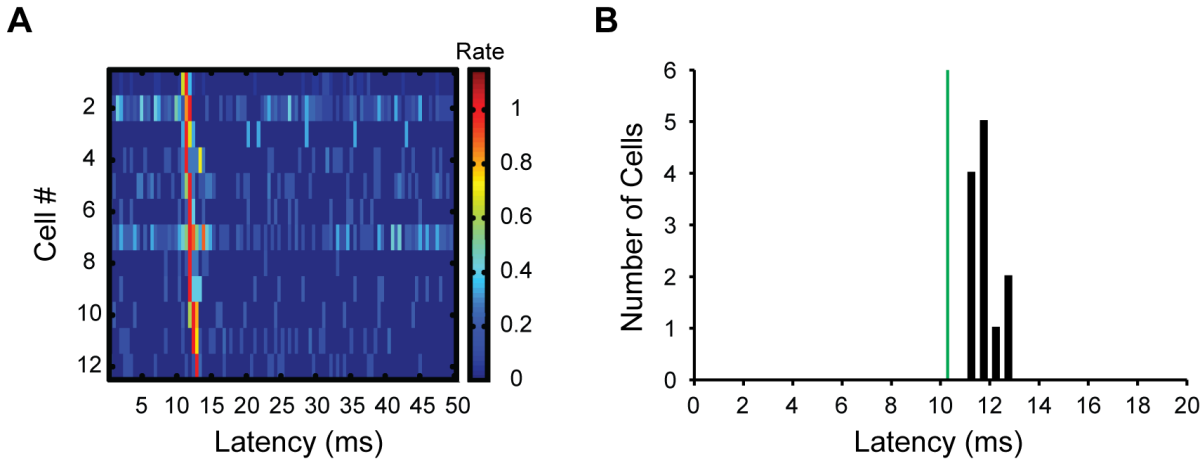


**Fig. 25.** The distribution of firing latencies of all MEC recorded neurons that were responsive to laser stimulation either in angular bundle or perforant path termination zone. **(A)** The distribution of firing latencies of all MEC recorded neurons that were responsive to laser stimulation in the angular bundle (cells from #1 to #10) and the perforant path termination zone (cells #11 and #12). Color-coded spike raster showing firing rates of particular cells as a function of time after the laser stimulation. Firing rates are normalized to a peak firing rate and the color scale is shown on the right. **(B)** Response latency histogram showing distribution of peak response latencies. Green line indicates average response latency (10.06 ± 0.27 ms) for all principal cells in Fig. 18. From spike raster and latency histogram it can be clearly seen that response latencies were longer compared to the ones obtained from direct MEC stimulations (10.06 ± 0.27 ms, for putative principal cells) and shorter compared to the ones obtained from hippocampal CA1 stimulations (21.11 ± 2.37 ms).

### 3.5.3 Blocking Excitatory Neurotransmission

Drug infusion in the recording area was carried out to block excitatory neurotransmission to verify that neurons were excited directly by light and not by excitatory connectivity with other neurons. Also we reasoned that following a successful drug infusion multiple peak firing, corresponding to the firing evoked by indirect excitation, should diminish and only a peak with minimum response latency would remain, the latter indicating direct excitation. During the surgical procedure, guide cannula was implanted near the optrode in MEC. If during the 2

min laser stimulation session MEC cells with multiple peak responses were identified, a drug cocktail was infused to the recording location. Cocktail consisted of nitroquinoxaline-2,3-dione (CNQX) and D-2-amino-5-phosphonopentanoic acid (AP-5), which are competitive AMPA / kainate and NMDA receptor antagonists, respectively, and should interrupt glutamatergic neurotransmission. The effect of CNQX / AP-5 cocktail was monitored closely following the infusion by 2 min laser stimulation sessions which were carried out right after the infusion, 5 min after the infusion, and later every 10 min until the cell's firing returned to "before" state (passive washout of the drug cocktail). In total there were 5 cells that showed clear changes in their laser-excited firing patterns after the drug infusion (Fig. 26). In all 5 cases we observed substantially reduced spontaneous firing. Furthermore, multiple peak latencies "disappeared" and the only remaining peak latency was with the minimum response time. In some of the cases CNQX / AP-5 infusion also caused a decrease in the directly evoked activity which can be clearly seen by comparing spike numbers of minimum response latencies before and after the drug infusion (e.g. Fig. 26, 17076_17051203_T8C1). Late after the drug infusion multiple peak responses "returned" in 4 of the cases (in 17076_10051206_T7C1 it did not); those multiple peaks can be interpreted as arising from indirect excitation which became plausible again after the CNQX / AP-5 cocktail was passively washed out and the glutamatergic neurotransmission made available. All in all, this experiment further strengthens the claim that the majority of neurons activated by laser stimulations in MEC were excited directly, and therefore possessed projections terminating in hippocampus.

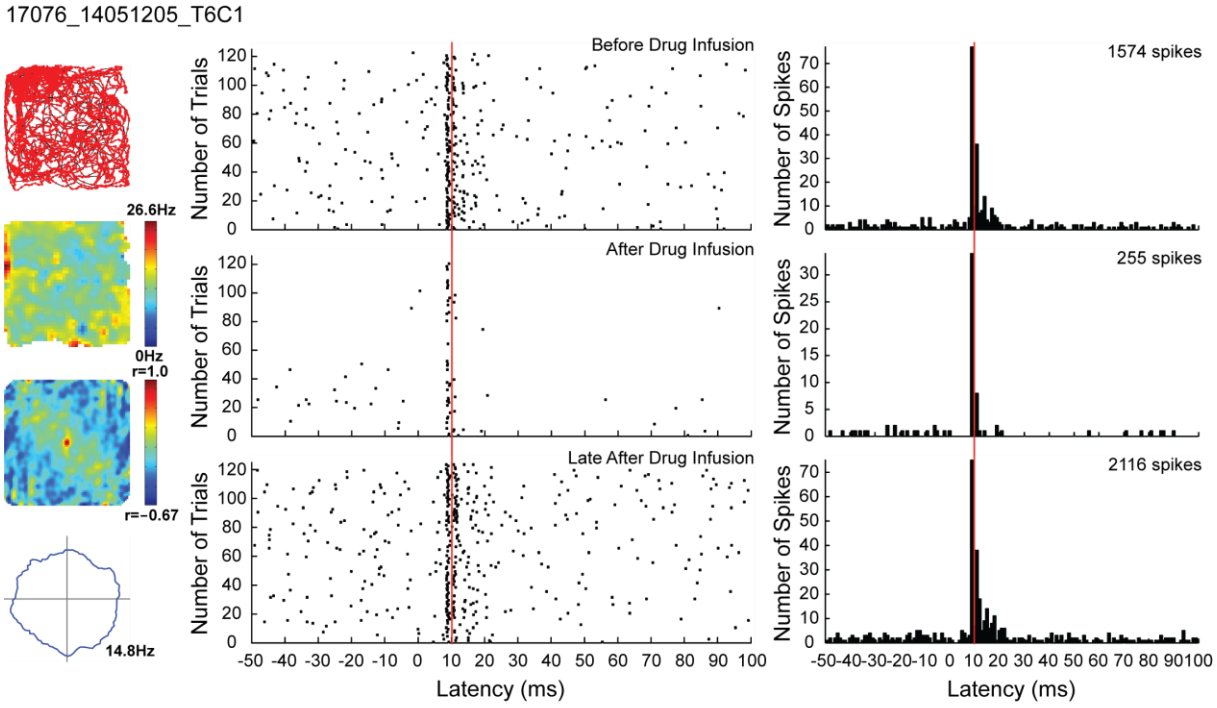
17076_14051205_T6C1
26.6Hz
0Hz
r=1.0
r=−0.67
14.8Hz
Before Drug Infusion
After Drug Infusion
Late After Drug Infusion
Number of Trials
Latency (ms)
1574 spikes
255 spikes
2116 spikes
Number of Spikes

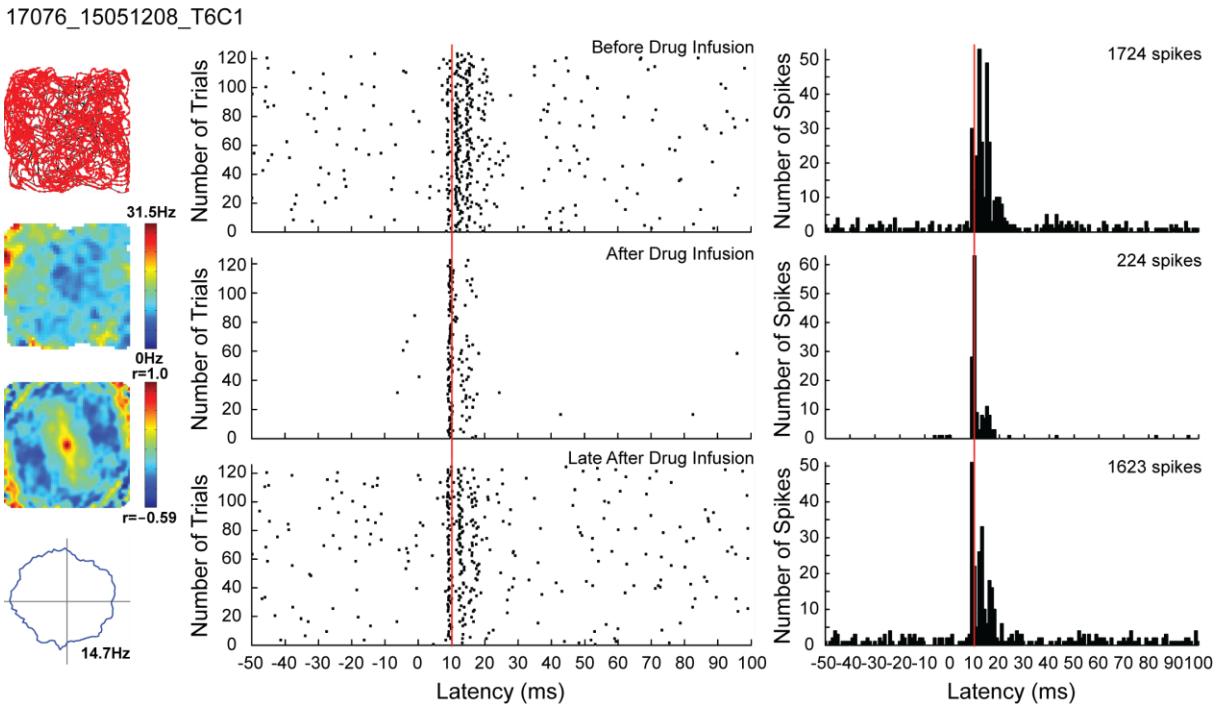
17076_15051208_T6C1
31.5Hz
0Hz
r=1.0
r=−0.59
14.7Hz
Before Drug Infusion
After Drug Infusion
Late After Drug Infusion
Number of Trials
Latency (ms)
1724 spikes
224 spikes
1623 spikes
Number of Spikes

17076_17051203_T8C1

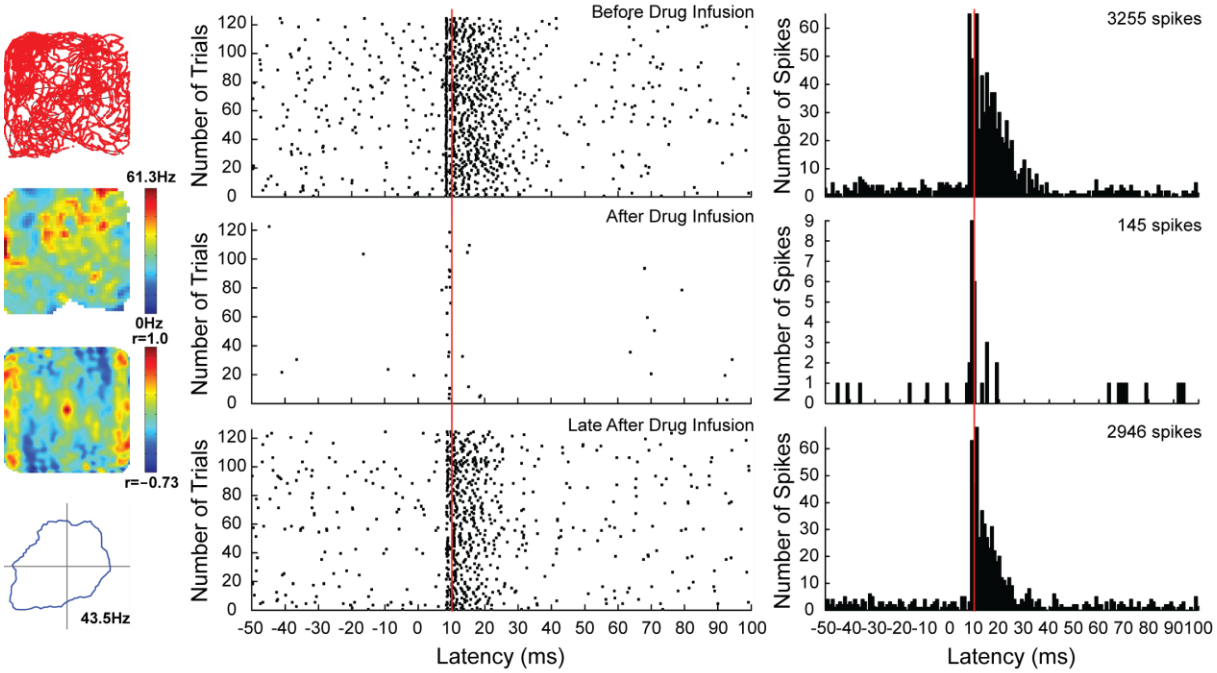


17622_04081201_T2C1

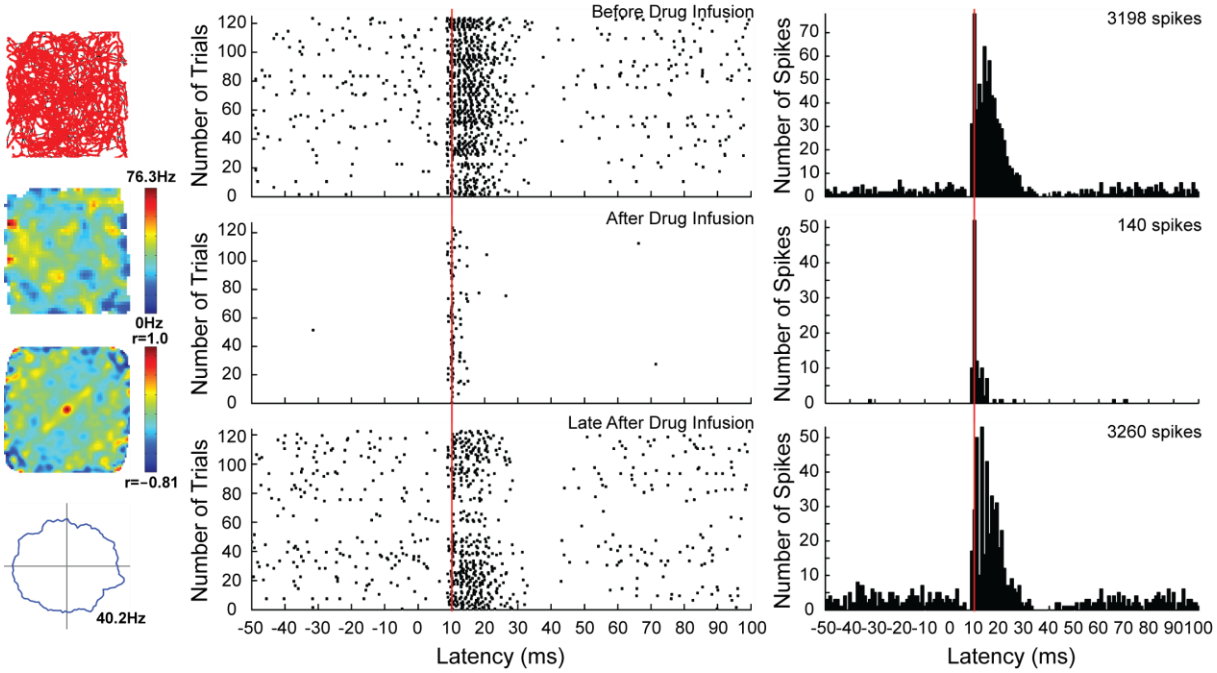

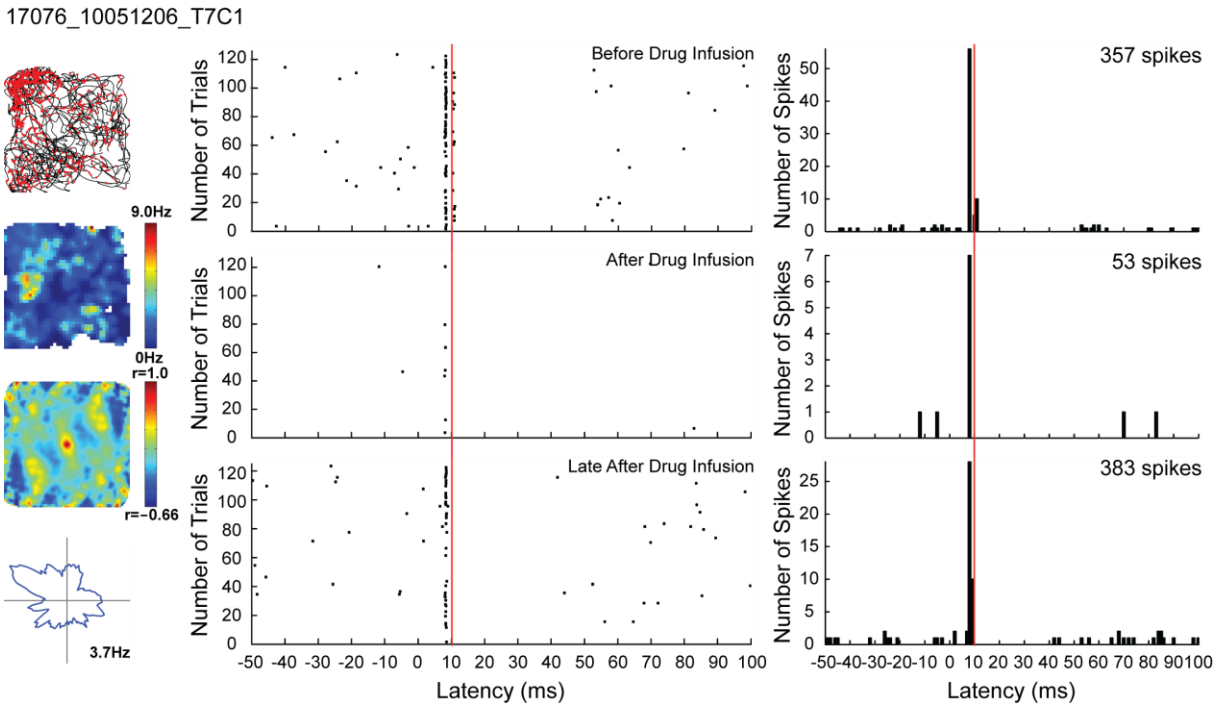


**Fig. 26.** The firing patterns of MEC recorded neurons that showed response to the CNQX / AP-5 cocktail infusion to the recording area. Each panel corresponds to one cell with the first session's number identified on top. Left section, from top to bottom: i. the rat's running path (black line) with the superimposed spike locations (red dot); ii. the firing rate map with maximum and minimum firing-rate values indicated on the color-coded bar; iii. the autocorrelogram extracted from firing rate map with maximum and minimum correlation values indicated on the color-coded bar; iv. polar map showing firing rate as a function of the rat's head direction with peak rate indicated. Middle section, from top to bottom: i. spike raster before drug infusion showing spike distribution before and after laser stimulation; ii. the spike raster after drug infusion; iii. the spike raster late after drug infusion. Right section: spike histograms corresponding to the spike rasters in the middle section (red line corresponds to 10 ms time stamp).

# 4. DISCUSSION

To identify hippocampus projecting MEC neurons we applied retrograde gene delivery strategy combined with optogenetics. A different approach could have been antidromic stimulation in the hippocampus while at the same time recording in MEC. However, this technique has been disregarded as it would probably only allow identifying small fraction of whole population of MEC neurons with projections to hippocampus, because antidromic stimulations in a single location in the hippocampus would evoke action potentials in only those MEC axons that are in close proximity of stimulating electrode. AAV2/1 viral vector has been chosen to deliver optogenetic payload due its low toxicity, high infectivity, long-term gene expression, and serotype specific higher diffusion and expression in CA1-CA3 regions (*91*, *103*). rAAV2/1 carried a plasmid coding ChR2-FLAG construct gene; additional modifications (please see method section) were made to improve transgene transcription, expression, and plasma membrane localization. ChR2 was used as an optogenetic tool to identify infected neurons in the MEC, whereas FLAG was exploited as a tag for immunohistology. The rAAV2/1 was injected stereotactically into the dorsal hippocampus of 8 rats. After the rats were transcardially perfused ChR2-FLAG expression was observed around the injection site as well as throughout various hippocampal subregions (dentate gyrus, CA1, CA2, and CA3). What is more, immunohistochemical staining showed that ChR2-FLAG was widely expressed in superficial layers of MEC (mostly layer II and III); however, it was almost absent from the deep layers of MEC, which eliminates the possibility of passive diffusion of rAAV2/1 (Fig. 15). These results correspond with what is known about the circuitry between MEC and the hippocampus – that the prominent projections to the hippocampus arise from layers II and III in the entorhinal cortex (*17*). Also from Nissl stained sections it can be seen that electrodes were located in MEC layers expressing ChR2-FLAG (Fig. 15). Altogether, these results suggest that our chosen approach to tag hippocampus projecting MEC neurons by retrograde gene delivery was successful and at the same time it introduced optogenetic control over transduced cells.

To elucidate the functional identity of infected neurons electrophysiological *in vivo* recordings together with optogenetic excitation protocol were carried out. Behavioral data was collected while the animals ran in 1 $m^2$ square enclosure at the same time recording neuronal activity in the MEC. To introduce objectivity to our cell type classification specific criteria were devised and according to them all MEC recorded cells were classified into five categories: grid cells, head-direction cells, border cells, unknown principal cells, and

interneurons. After all experimental recordings were carried out, behavioral data for each recorded cell was shuffled 100 times (leading to 13600 permutations) and that shuffled data was used to generate grid, head-direction, and border score distributions. Also the aforementioned spatial scores were calculated for each cell with the real behavioral data. For a cell to be classified as grid, head-direction or border cell, its respective score should exceed the 99$^{th}$ percentile value of respective shuffled score distribution (Figs. 10A, 11A, 12A). If a cell did not pass the 99$^{th}$ percentile criterion, it was defined as unknown principal cell. Cells with high firing rate (>5 Hz), narrow spike form (peak-to-trough width <0.3 ms), and no apparent spatial or directional firing were counted as interneurons (Fig. 13A). Even though the 99$^{th}$ percentile criterion should be a strong cut off value, still some of the cells that ended up in their respective cell categories did not have spatial firing properties that were obvious just by inspecting the spatial firing maps "by eye" (e.g. putative grid cells in Fig. S1 – 17076_16051208_T6C1, 17622_09081201_T2C1; putative border cell in Fig. S3 – 17622_09081206_T2C1). On the other hand, some of the cells did not pass the 99$^{th}$ criterion but still had spatial firing resembling that of grid cells (e.g. Fig. S4 - 17506_26071203_T4C1, 17506_30071208_T1C2). The latter cases could arise due to the fact that those cells have been recorded quite dorsally and had the firing fields with a big spacing which did not "fit" to the environment available to the animal; therefore, the six-fold symmetry was also not represented in the autocorrelograms. However, this problem could be avoided if, for example, 2.25 m$^2$ (1.5 m walls) square enclosure would be used instead of 1 m$^2$. Concerning criteria for interneurons, there were two cells that had peak-to-trough width >0.3 ms (0.34 ms and 0.41 ms) but were still counted as interneurons. The main reason for that was they had fairly high firing rates (10.82 Hz and 12.51 Hz, respectively) and were looked upon as "exception cases" for our peak-to-trough criterion (please bear in mind that the criterion we used for interneurons was stricter than the one used by Loren et al. (*102*), which was <0.4 ms). Nonetheless, except for the few aforementioned cases the majority of the cells judging by their spatial firing properties as well as spike waveforms responded well to the cell classification criteria and ended in the expected cell type categories. In total there were 136 neurons recorded in superficial layers of MEC. 107 of those neurons were classified as putative principal cells and 29 as putative interneurons. Putative principal cells were further sorted out as 34 grid cells, 27 head-direction cells, 12 border cells, and 34 unknown cells. Also 7 cells in the border cells category also passed the criterion for head-direction cells; therefore, they can be counted as conjunctive border × head-direction cells.

To identify which cells of the recorded MEC neuron population had projections terminating on hippocampus laser stimulations were carried out in the recording area of MEC. Laser stimulations consisted of 3.5 ms 473 nm light pulses of ~10 mW light power (at the fiber tip) delivered at 1 Hz frequency for 2 min. Spike times around the light stimulus (with the interval of ± 100 ms) were shuffled 10000 times and a 3 ms bin with the highest number of spikes was identified each time. Spike numbers from that 3 ms bin in each shuffled data set were used to generate spike number distribution. A particular cell was counted as a responsive one if the number of spikes in the 3 ms bin of that cell exceeded the $99.9^{th}$ percentile value of the shuffled data. In total 64 cells of all MEC recorded neuron pupulation (47.1%) passed the criterion and were counted as photoresponsive cells. This result could indicate two things:

i. action potentials in those cells were evoked directly, i.e. ChR2 expressed in the plasma membrane of neuron of interest was activated by laser light;

ii. action potentials in those cells were evoked indirectly, i.e. by ChR2-expressing MEC neurons with excitatory synaptic connections to the cell of interest.

Direct laser excitation would indicate that the cell has projections to hippocampus as it has been retrogradely infected by rAAV1/2-ChR2-FLAG and expresses the ChR2 in its plasma membrane. Indirect laser excitation would not eliminate the possibility (however, it would be considerably less likely in this case) that the neuron still has axons terminating in hippocampus as various factors can influence retrograde infection (will be discussed later in this chapter) and the neuron with terminal hippocampal projections simply may have not received rAAV2/1. However, the latter option does not allow to infer that those MEC cells have the aforementioned projections. Therefore, we were more interested in the cases of direct excitation. In order to make a distinction between direct / indirect excitation, we looked at response to laser stimulation latency variation. We speculated that minimal and stable response latencies would suggest direct excitation, whereas longer and varied response latencies could correspond to indirect excitation as it requires synaptic transmission step.

In the population of 64 light responsive cells 44 were principal cells and 20 were interneurons. Response latency distributions between these two groups showed some variation. Response latencies for principal cells varied minimally (10.06 ± 0.27 ms) and short latencies predominated within and between cell types and different animals (Fig. 18). The only exception to this is responsive border cell group, which contained only two members with 13.27 ms and 16.55 ms (this point will be discussed later). Response latencies for interneurons were a bit longer and also possessed slightly higher variation (11.26 ± 0.82 ms)

(Fig. 20). Also more prolonged response latencies were observed with the interneuron group as well as firing with multiple peak latencies (e.g. Fig. 21) was encountered in interneurons more frequently than in principal cells. We hypothesized that in these multiple peak latency cases both direct and indirect excitations can be observed, as the minimal latency would correspond to a direct excitation and all the remaining peaks could be related indirect excitation arising through excitatory synapses. The reason why this phenomenon is more frequently observed in interneurons instead of principal cells could be that the majority of excitatory connections within MEC layers II and III innervate inhibitory cells, which in our study probably correspond to interneuron category (*107*). Furthermore, we observed peculiar property concerning the gradual response latencies increase both within principal neuron and interneuron groups. There exists a 1 ms "step" between 10 ms and 11 ms response latencies (from 10.71 ms to 11.63 ms for principal cells and from 10.42 ms to 11.67 ms for interneurons). Before the 11 ms value response latencies do not show much variation (9.27 ± 0.11 ms) and increase in somewhat gradual fashion, whereas after 11 ms response latencies start increasing in a steeper fashion and show much more variation (14.21 ± 0.69 ms). Whether 11 ms is a cut off value dividing direct and indirect excitations, we cannot prove, nonetheless, it could be used as a fairly good indicator. Actually, 7 out of 44 (15.9%) responsive principal cells had response latencies higher than 11 ms, whereas for interneurons this number was 8 out of 20 (40.0%), which again strengthens the claim that indirect excitation was more frequent in responsive interneuron population. All in all, these results suggest that both responsive cell type categories contained cases of direct and indirect excitation, with former one being in majority. This in turn lets us imply that both principal neurons and interneurons have projections terminating on hippocampus.

To help us further differentiate between direct and indirect excitation latencies we also did three different control experiments: i. laser stimulations in the dorsal CA1; ii. laser stimulations in the angular bundle or the perforant path projection zone (backfiring approach); iii. infusion of CNQX / AP-5 drug cocktail in the MEC to block excitatory glutamatergic neurotransmission followed by laser stimulation. First of all, by shinning laser in the dorsal CA1 we hoped to excite CA1 neurons expressing ChR2 with projections to MEC which in turn would stimulate MEC neurons in the recording area. We were able to detect 7 MEC cells (4 principal cells and 3 interneurons) that responded to dorsal CA1 laser stimulations. Response latencies in this sample varied from 15.75 to 30.18 ms (21.11 ± 2.37 ms) which is significantly ($t(69) = -4.46$, $P = 0.004$) longer compared to latencies acquired from MEC

stimulations (10.43 ± 0.32 ms) (Fig. 23). This was expected as additional time is required for neurotransmission along the CA1 axon and throughout the synapse terminating on the recorded MEC neuron. Second, with the backfiring approach we were hoping to shine laser light on the axons of hippocampus projecting MEC neurons which were retrogradely infected by rAAV2/1. Two locations were chosen for this experiment: angular bundle and perforant path projection zone, as both of them should hold passing MEC axons. We identified 12 neurons that showed response to these stimulations (4 grid cells, 1 border, 4 unknown cells, and 3 interneurons). Response latencies varied from 11.17 ms to 12.62 ms (11.78 ± 0.14 ms) and were significantly ($t(74) = 3.88$, $P < 0.001$) longer compared to ones from local MEC stimulations (10.43 ± 0.32 ms) (Fig. 25). This was also expected, because the addition of several milliseconds to the response latency arises due to the backpropagation of the action potential. Comparing mean response latencies between angular bundle and perforant path projection zone stimulations (11.62 ± 0.10 ms vs. 12.61 ± 0.02 ms, respectively), we see that targeting angular bundle gives shorter results as it is closer to the MEC and backpropagation of an action potential to the soma of the recorded neuron is faster. Finally, CNQX / AP-5 cocktail was infused in the recording area to block excitatory glutamatergic neurotransmission. We had 5 cases (in 2 animals) that showed response to the drug infusion (Fig. 26). Straight after the drug infusion in all 5 cases multiple response peaks were abolished with only minimal response latency remaining and later on after the passive drug washout multiple peak firing returned in 4 of the cases. We postulate that after excitatory neurotransmission was blocked indirect excitation was made unavailable also; therefore, multiple peaks arising from indirect excitation were not visible shortly after the drug infusion. The only remaining peak corresponded to direct excitation as it was the only plausible way to evoke action potentials in the recorded cells using laser light. After the drug washout the cell returned to its "normal" responsive state, where both direct and indirect excitations are available and observable again. Altogether, these control experiments provide compelling confirmation that the majority of MEC neurons that showed response to local MEC stimulations are directly activated as their response latencies were constant and minimal. Moreover, backfiring approach provided direct evidence that both grid cells and border cells have hippocampal projections.

We also looked at what fraction of MEC recorded neuron population was responsive to laser stimulations as it could loosely indicate what type of MEC signals and to what extent they are relayed to hippocampus. The first striking feature is that almost half (64 out of 136,

47.1%) of MEC recorded neurons were responsive to local laser stimulations. Of course, we cannot expect that all of those responsive neurons were excited directly; nonetheless, it stands as a solid indicator that the MEC output to hippocampus if fairly extensive. This proportion is also in line with the results which were seen by Varga et al. (*108*). Larger part of responsive cell population was comprised of principal cells (44 out of 64, 68.8%), whereas only ~1/3 of laser activated cells were interneurons (20 out of 64, 31.2%); please bear in mind that we argued that the proportion of indirectly excited cells in the interneuron population is also larger. The result that both cell populations have hippocampal projections was expected as it is well documented in literature (*22*, *104*). A substantial portion of responsive principal cells were grid cells (18 out of 44, 40.9%), with unknown principal cells (13 out of 44, 29.5%) and head-direction cells (11 out of 44, 25%) not that much behind, whereas borders cells being a minority of the population (2 out of 44, 4.5%). What is more, we believe that both of those border cells were activated indirectly (response latencies of 13.27 ms and 16.55 ms); however, in the backfiring experiment we detected one border cell with axonal projection to hippocampus and thus did not reject the notion that border cells also possess hippocampal projections [the proof of hippocampus projecting border cells was also provided by Zhang *et al*. (*109*)]. Nevertheless, it may not be feasible to infer the exact proportions of input each functional cell type class provide to hippocampus and all the aforementioned numbers should be looked upon with caution, as acquired numbers for different responsive cell types heavily depend on various factors. First of all, a sample size of recorded cells plays a major role; for instance, it could be that with increased sample size border cells with direct excitation would be observed. Differences in terminal distribution of projecting neurons could result in certain cell types being infected by virus more profoundly because their axons reach areas of virus injection, whereas some projections could be left out due to absence of virus in their terminal distribution in hippocampus. Myelination could also be a prominent factor as it was reported that myelination decreases the efficiency of retrograde AAV transduction (*110*). Hindered light propagation in brain tissue (*78*) could lead to cases where MEC neurons actually express ChR2 but because of obstructed light delivery in brain tissue or reaching light power being too low to activate ChR2 those neurons would simply not be counted as light responsive cells and therefore be looked upon as without hippocampus projecting axons. It should be also kept in mind that moving tetrode in dorsal-ventral axis of superficial layers of MEC record only a portion of cells present there because its unit isolation radius is fairly limited (*101*).

To sum up, we found that MEC provides a strong input to hippocampus formation. Our results suggest that all functional cell types in MEC have hippocampus targeting projections, be it spatial cells, like grid cells, head-direction cells, and border cells, or principal neurons without any obvious spatial firing properties and interneurons. The observation that grid cells project to hippocampus was anticipated, as it stands as a cornerstone in many different grid-to-place field transformation models (*10, 13, 14, 60*). However, in recent studies it has been shown that place field form earlier than grid fields in young animals (*15, 16*); also Koenig *et al.* demonstrated that with reduced theta activity place cell firing persisted, whereas grid cell firing vanished (*62*). This suggests that grid cells are not the critical component in place field formation and other entorhinal-hippocampal space circuit inputs may be involved. Our study confirmed the notion that place cells can be provided with landmark and boundary related information by MEC border cells (*4, 63*). Considering the MEC located interneurons that provide input to hippocampus, their existence has been also confirmed in another study. What is interesting, these hippocampus projecting interneurons target local interneuron population in hippocampus and were hypothesized to be responsible for highly synchronized theta activity within the interconnected areas (*104*). Furthermore, we also saw the large part of MEC output is carried by head-direction cells and principal cells with unknown spatial firing properties. This introduces new questions: if these cells target principal cell or interneuron population in hippocampus (or both) and what are they role in grid-to-place field transformation. And how place cells deal with such a vast array of cortical information and how it distinguishes between spatial and non-spatial components to generate a single spatial output? Lee *et al.* suggests that by gating of MEC inputs, basically most silent principal hippocampus neuron can be “turned into” an active place cell (*111*). All in all, from our work it is obvious that hippocampus receives broad functional variety of entorhinal outputs which in turn makes the navigation through a specific environment possible.

# 5. CONCLUSION

The work done during my master's thesis revealed functional complexity of hippocampus-entorhinal cortex space circuit. Using retrograde gene delivery strategy we were able to tag hippocampus projecting MEC neurons. Furthermore, by combining optogenetics with electrophysiological recordings *in vivo,* we determined the functional identity of MEC neurons that had projections to hippocampus. Our results indicate that all MEC cell types have hippocampus targeting axons. We found that the larger part of input to hippocampus was provided by grid cells, with other spatial cells, like head-direction cells and border cells, and non-spatial cells, like principal unknown cells and interneurons, also providing their output to hippocampus.

These findings are consistent with the proposed models for place signal formation, which involve deriving metric properties from grid cells and boundary related information from border cells. This combined input could also explain recent findings that place cell firing still persists with reduced theta activity which destabilize grid cell firing or that during ontogenesis place field formation precedes the formation of grid patterns. However, the presence of the considerably large MEC output generated by head-direction cells and principal non-spatial cells introduces new components into the grid-to-place field transformation puzzle. The convergent input from broad range of MEC cell types introduces the freedom for hippocampus to represent the extensive variety of available environmental situations. Altogether, my master's thesis project was a successful one as it provided the first empirical evidence of different functional cells types interconnecting the two mapping systems of hippocampus and entorhinal cortex.

# SUPPLEMENTARY FIGURES

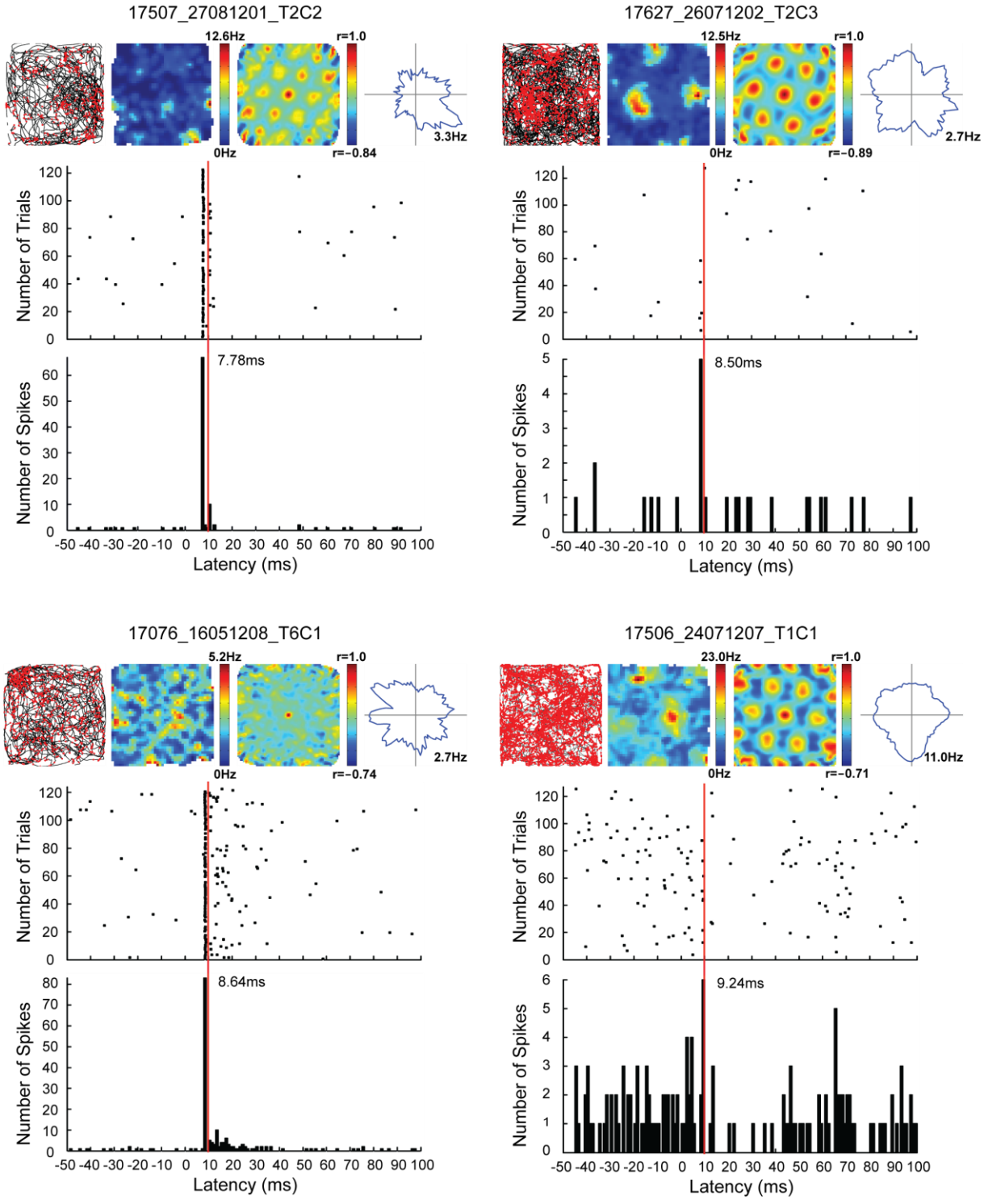

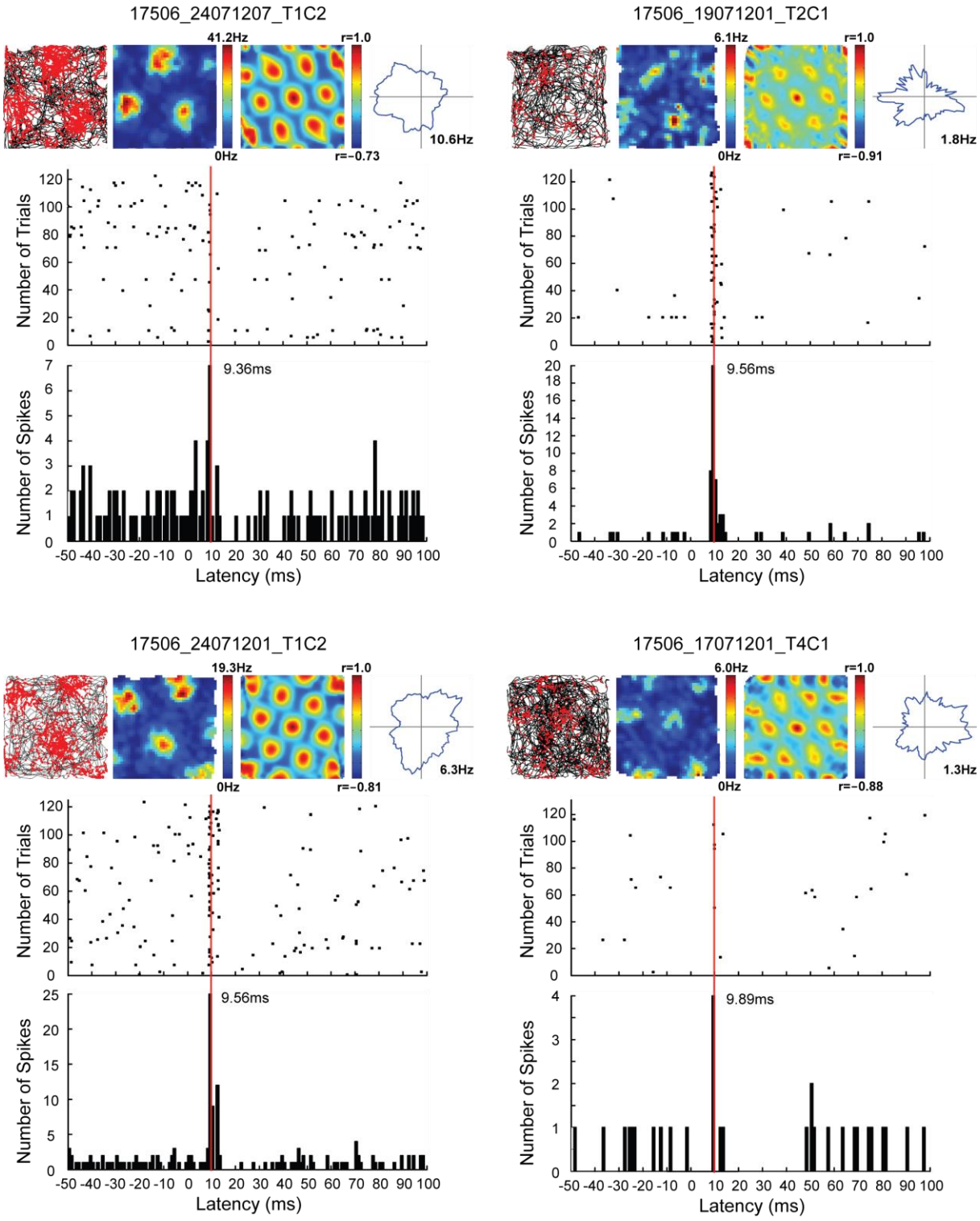
17506_24071207_T1C2
41.2Hz
r=1.0
0Hz
r=−0.73
10.6Hz
Number of Trials
Number of Spikes
9.36ms
Latency (ms)
17506_19071201_T2C1
6.1Hz
r=1.0
0Hz
r=−0.91
1.8Hz
Number of Trials
Number of Spikes
9.56ms
Latency (ms)
17506_24071201_T1C2
19.3Hz
r=1.0
0Hz
r=−0.81
6.3Hz
Number of Trials
Number of Spikes
9.56ms
Latency (ms)
17506_17071201_T4C1
6.0Hz
r=1.0
0Hz
r=−0.88
1.3Hz
Number of Trials
Number of Spikes
9.89ms
Latency (ms)

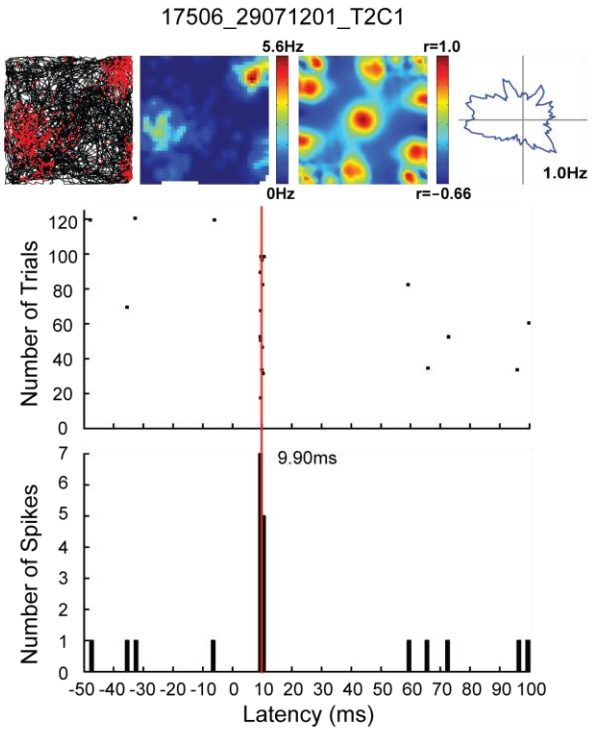
17506_29071201_T2C1
5.6Hz
r=1.0
0Hz
r=−0.66
1.0Hz
Number of Trials
Number of Spikes
9.90ms
Latency (ms)

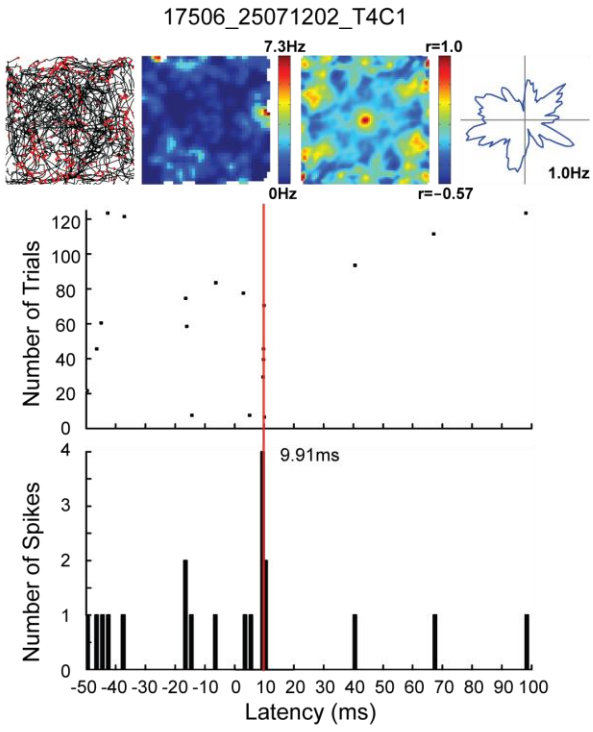
17506_25071202_T4C1
7.3Hz
r=1.0
0Hz
r=−0.57
1.0Hz
Number of Trials
Number of Spikes
9.91ms
Latency (ms)

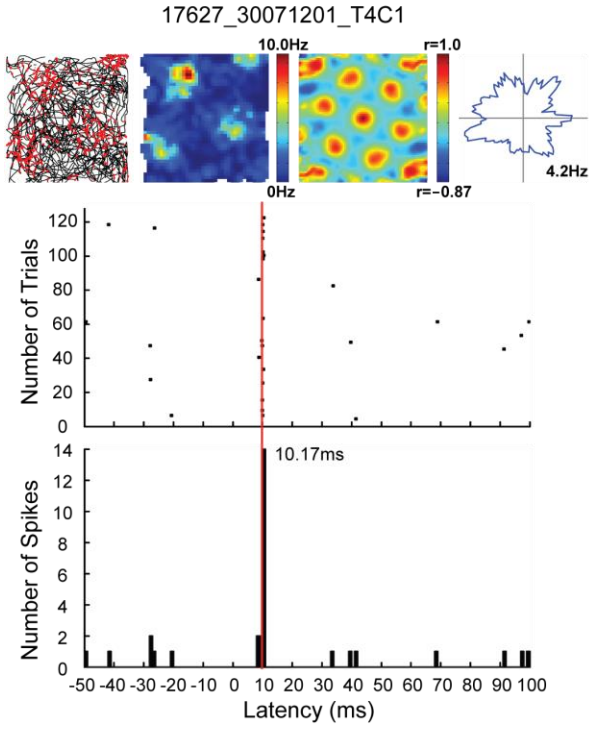
17627_30071201_T4C1
10.0Hz
r=1.0
0Hz
r=−0.87
4.2Hz
Number of Trials
Number of Spikes
10.17ms
Latency (ms)

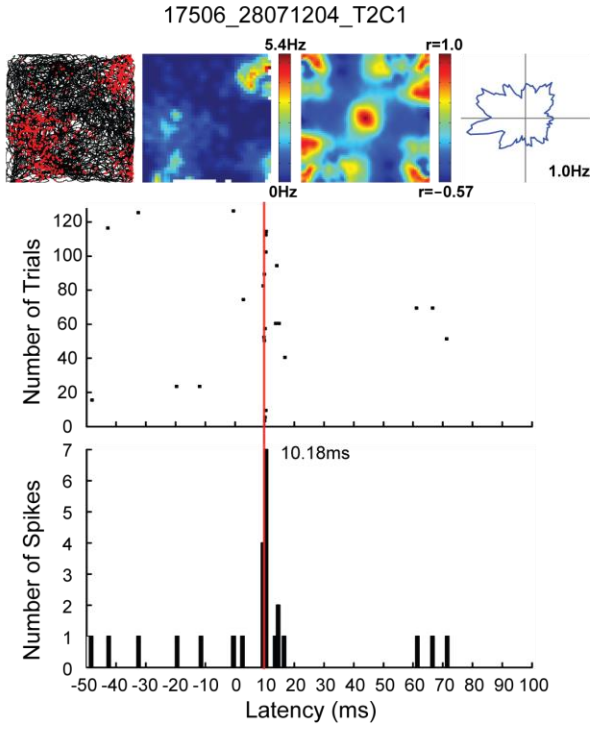
17506_28071204_T2C1
5.4Hz
r=1.0
0Hz
r=−0.57
1.0Hz
Number of Trials
Number of Spikes
10.18ms
Latency (ms)

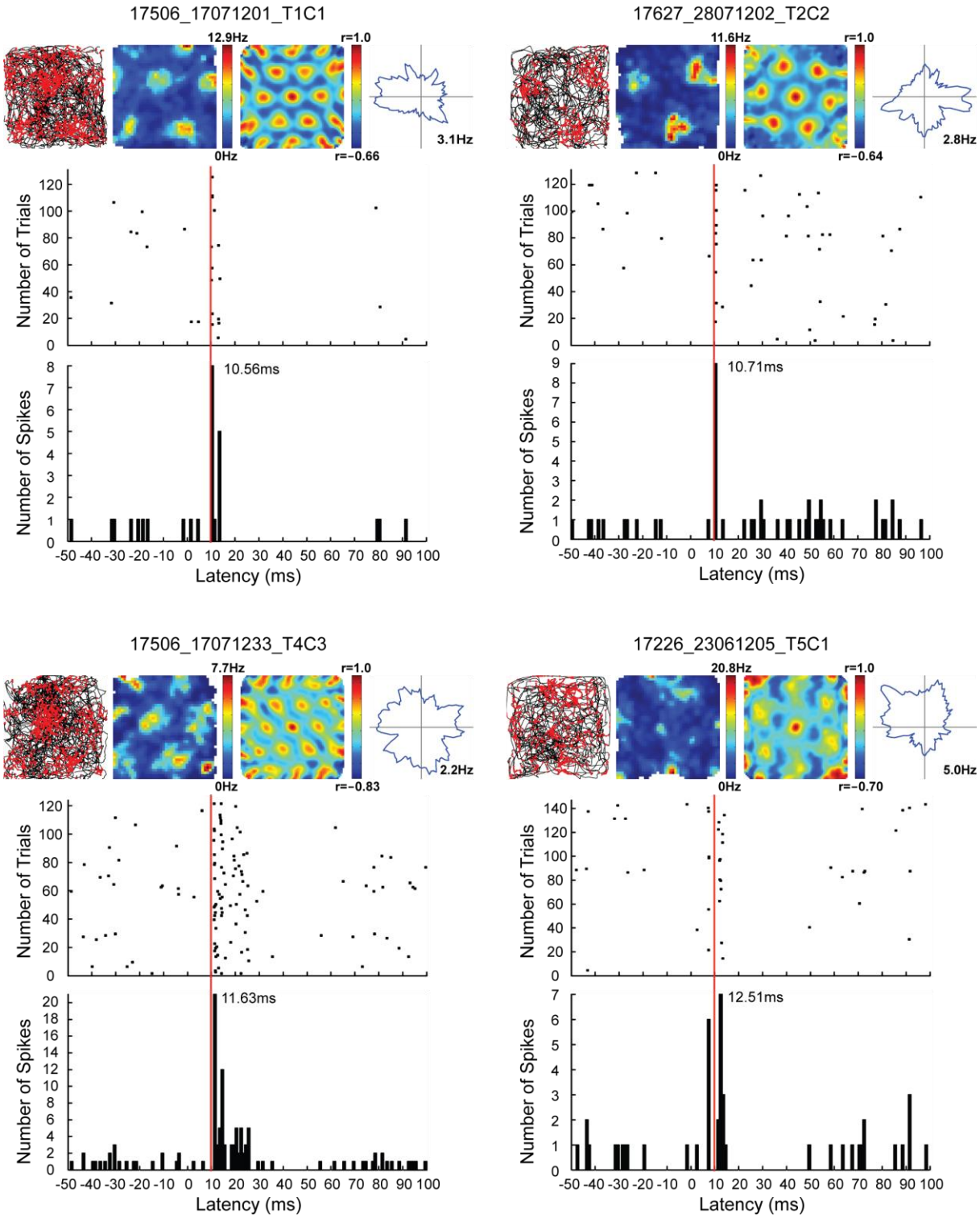
17506_17071201_T1C1
12.9Hz
r=1.0
0Hz
r=−0.66
3.1Hz
Number of Trials
Number of Spikes
10.56ms
Latency (ms)
17627_28071202_T2C2
11.6Hz
r=1.0
0Hz
r=−0.64
2.8Hz
Number of Trials
Number of Spikes
10.71ms
Latency (ms)
17506_17071233_T4C3
7.7Hz
r=1.0
0Hz
r=−0.83
2.2Hz
Number of Trials
Number of Spikes
11.63ms
Latency (ms)
17226_23061205_T5C1
20.8Hz
r=1.0
0Hz
r=−0.70
5.0Hz
Number of Trials
Number of Spikes
12.51ms
Latency (ms)

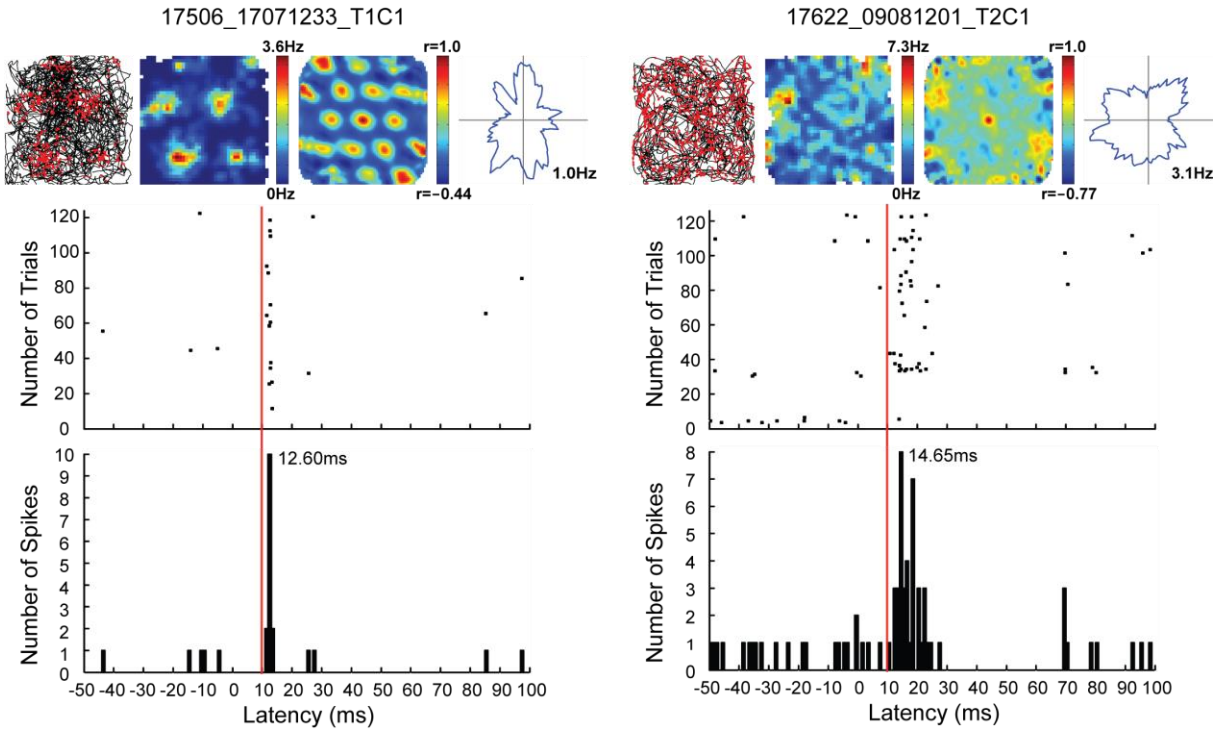


**Fig. S1.** Firing patterns of all light-responsive grid cells recorded in the MEC. Each panel corresponds to one cell with the session's number identified on top. Panels are shown in increasing order of observed response latencies. Top section, from left to right: i. rat's running path (black line) with superimposed spike locations (red dot); ii. firing rate map with maximum and minimum firing-rate values indicated on the color-coded bar; iii. autocorrelogram extracted from firing rate map with maximum and minimum correlation values indicated on the color-coded bar; iv. polar map showing firing rate as a function of rat's head direction with peak rate indicated. Middle section: spike raster showing spike distribution before and after laser stimulation. Bottom section: spike histogram corresponding to the spike raster with response latency indicated (red line corresponds to 10 ms time stamp).

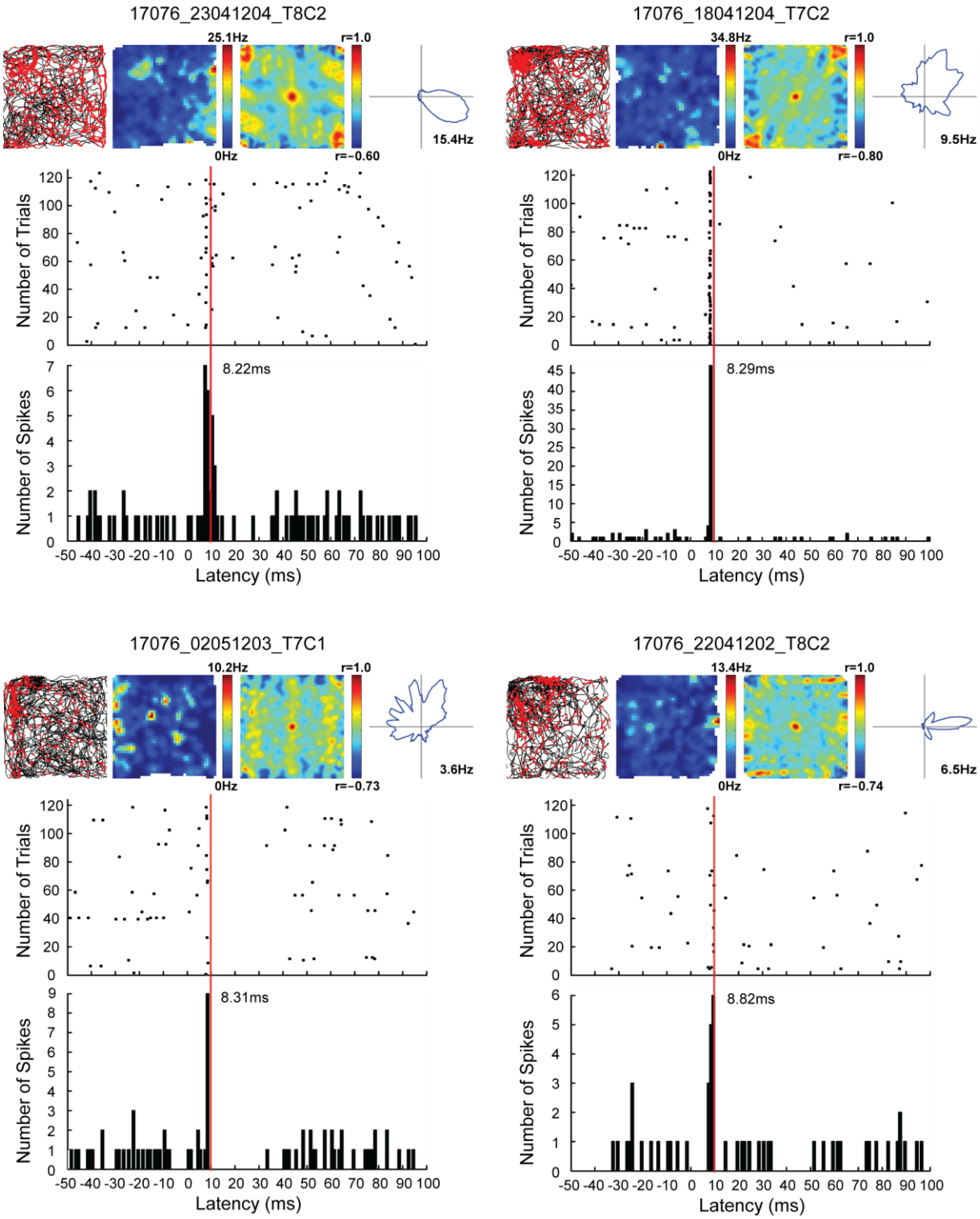
17076_23041204_T8C2
25.1Hz
r=1.0
0Hz
r=−0.60
15.4Hz
Number of Trials
Number of Spikes
8.22ms
Latency (ms)
17076_18041204_T7C2
34.8Hz
r=1.0
0Hz
r=−0.80
9.5Hz
Number of Trials
Number of Spikes
8.29ms
Latency (ms)
17076_02051203_T7C1
10.2Hz
r=1.0
0Hz
r=−0.73
3.6Hz
Number of Trials
Number of Spikes
8.31ms
Latency (ms)
17076_22041202_T8C2
13.4Hz
r=1.0
0Hz
r=−0.74
6.5Hz
Number of Trials
Number of Spikes
8.82ms
Latency (ms)

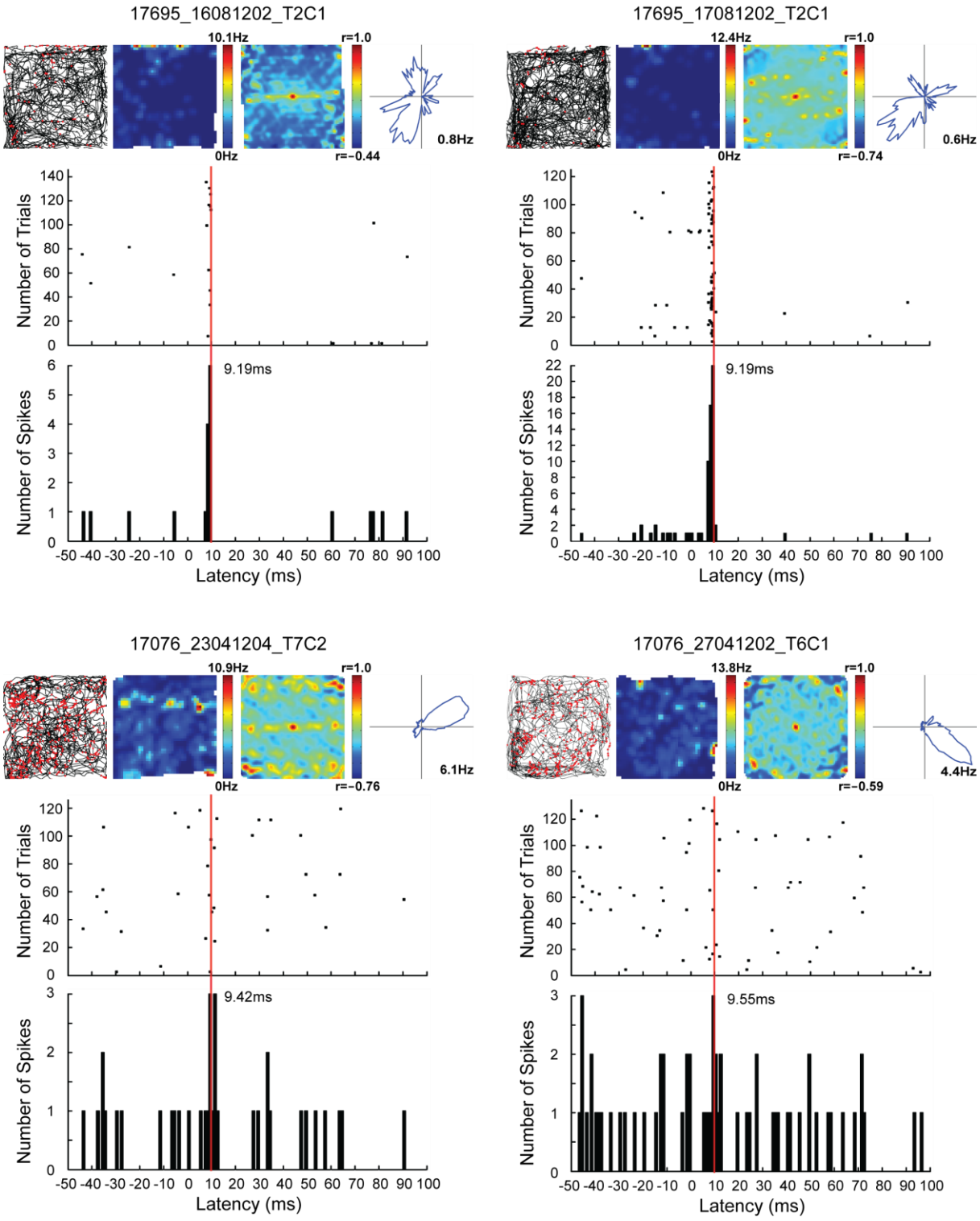
17695_16081202_T2C1
10.1Hz
r=1.0
0Hz
r=−0.44
0.8Hz
Number of Trials
Number of Spikes
9.19ms
Latency (ms)
17695_17081202_T2C1
12.4Hz
r=1.0
0Hz
r=−0.74
0.6Hz
Number of Trials
Number of Spikes
9.19ms
Latency (ms)
17076_23041204_T7C2
10.9Hz
r=1.0
0Hz
r=−0.76
6.1Hz
Number of Trials
Number of Spikes
9.42ms
Latency (ms)
17076_27041202_T6C1
13.8Hz
r=1.0
0Hz
r=−0.59
4.4Hz
Number of Trials
Number of Spikes
9.55ms
Latency (ms)

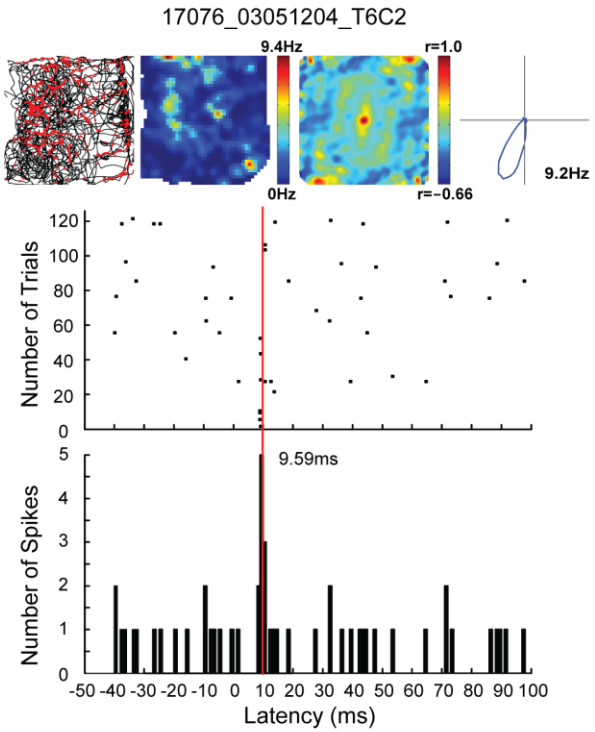


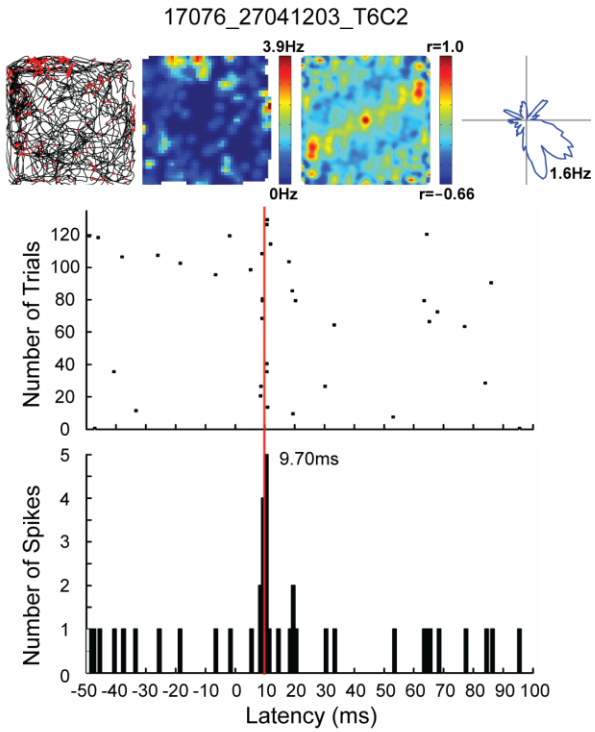


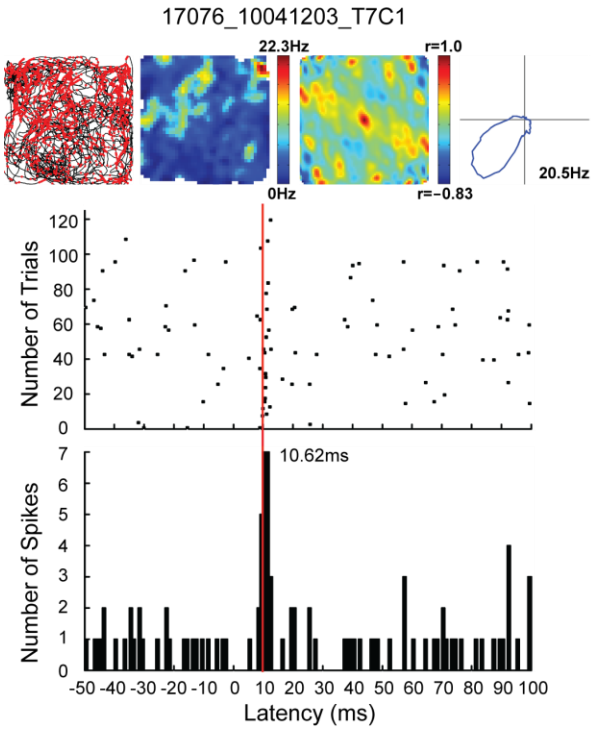


**Fig. S2.** Firing patterns of all light-responsive head-direction cells recorded in the MEC. Each panel corresponds to one cell with the session's number identified on top. Panels are shown in increasing order of observed response latencies. Top section, from left to right: i. rat's running path (black line) with superimposed spike locations (red dot); ii. firing rate map with maximum and minimum firing-rate values indicated on the color-coded bar; iii. autocorrelogram extracted from firing rate map with maximum and minimum correlation values indicated on the color-coded bar; iv. polar map showing firing rate as a function of rat's head direction with peak rate indicated. Middle section: spike raster showing spike distribution before and after laser stimulation. Bottom section: spike histogram corresponding to the spike raster with response latency indicated (red line corresponds to 10 ms time stamp).

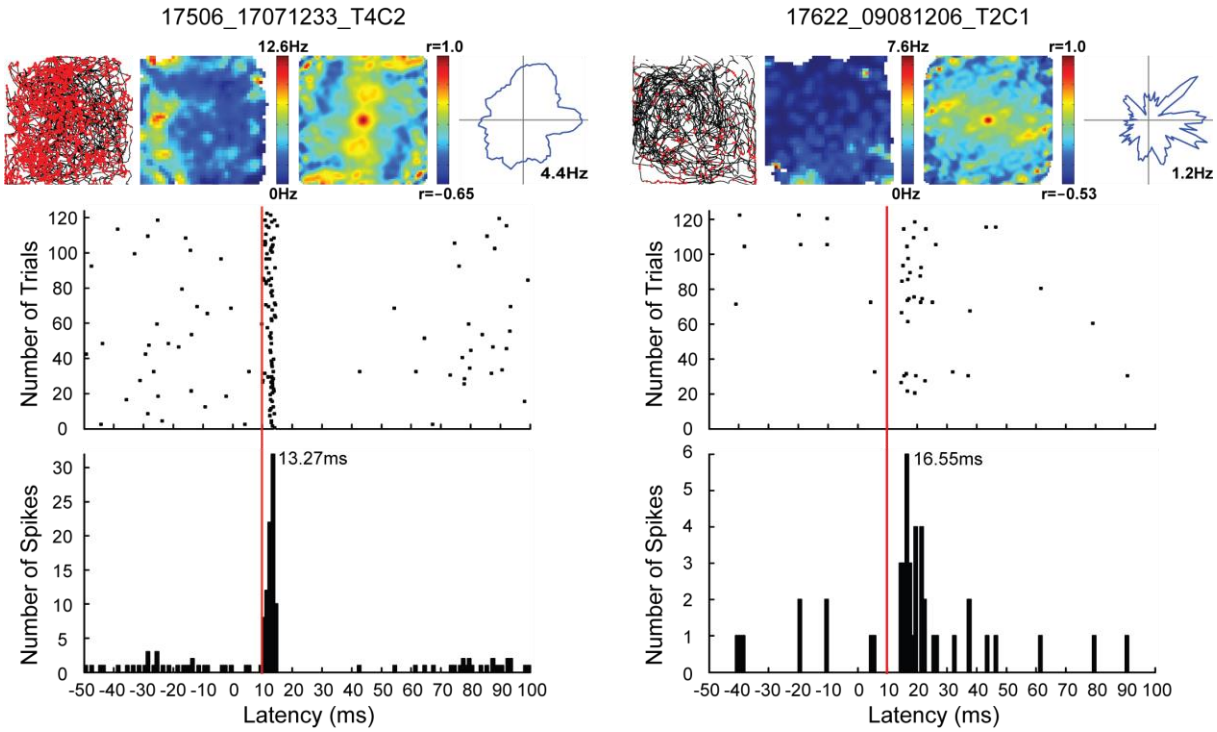


**Fig. S3.** Firing patterns of all light-responsive border cells recorded in the MEC. Each panel corresponds to one cell with the session's number identified on top. Panels are shown in increasing order of observed response latencies. Top section, from left to right: i. rat's running path (black line) with superimposed spike locations (red dot); ii. firing rate map with maximum and minimum firing-rate values indicated on the color-coded bar; iii. autocorrelogram extracted from firing rate map with maximum and minimum correlation values indicated on the color-coded bar; iv. polar map showing firing rate as a function of rat's head direction with peak rate indicated. Middle section: spike raster showing spike distribution before and after laser stimulation. Bottom section: spike histogram corresponding to the spike raster with response latency indicated (red line corresponds to 10 ms time stamp).

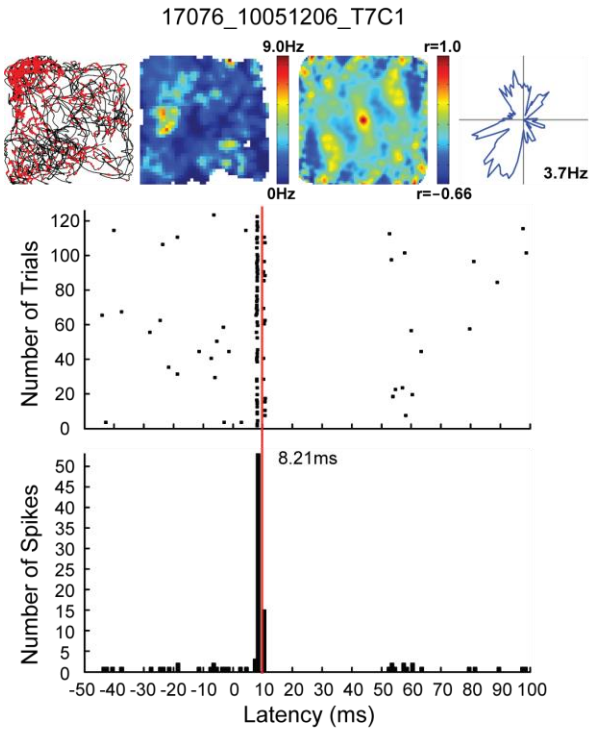
17076_10051206_T7C1
9.0Hz
r=1.0
0Hz
r=−0.66
3.7Hz
Number of Trials
Number of Spikes
8.21ms
Latency (ms)

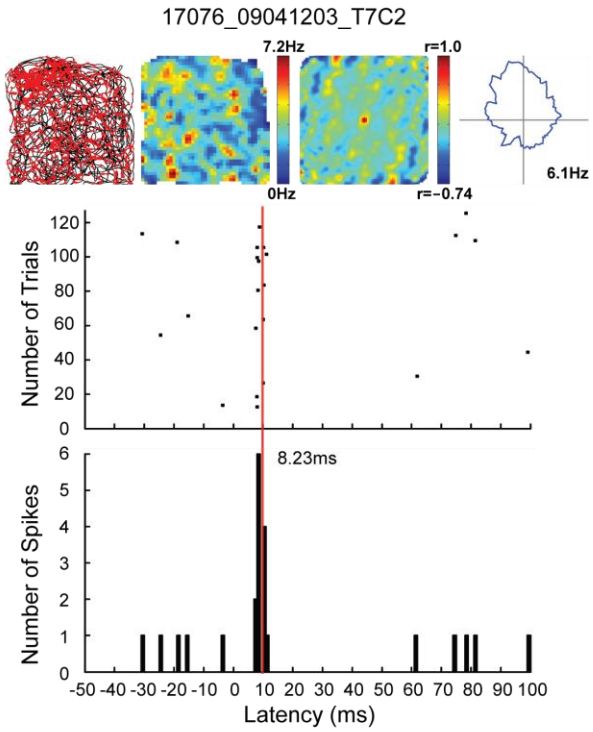
17076_09041203_T7C2
7.2Hz
r=1.0
0Hz
r=−0.74
6.1Hz
Number of Trials
Number of Spikes
8.23ms
Latency (ms)

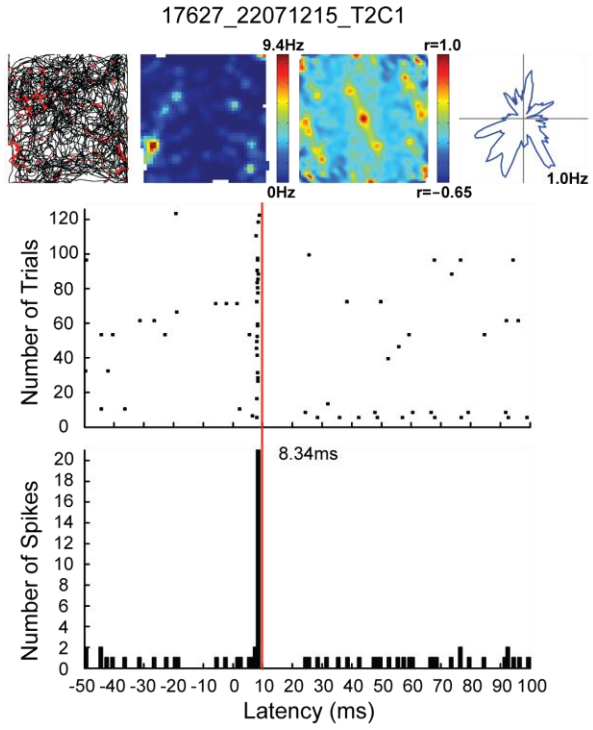
17627_22071215_T2C1
9.4Hz
r=1.0
0Hz
r=−0.65
1.0Hz
Number of Trials
Number of Spikes
8.34ms
Latency (ms)

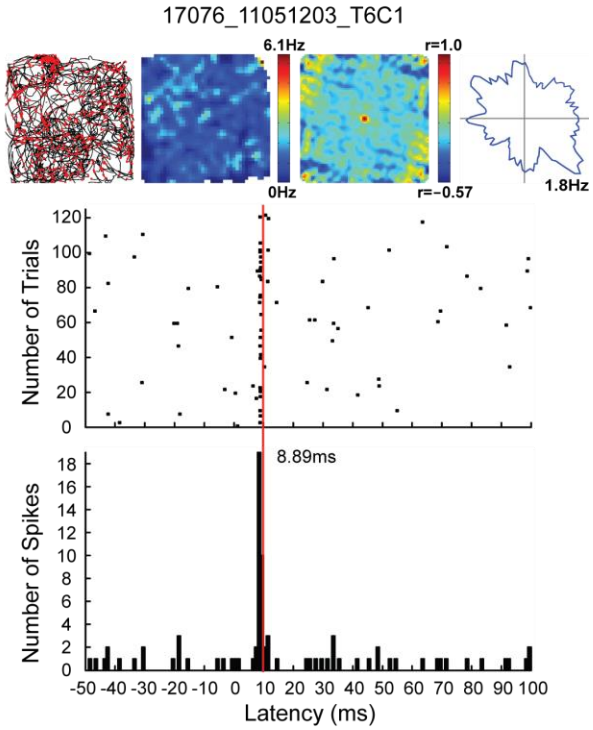
17076_11051203_T6C1
6.1Hz
r=1.0
0Hz
r=−0.57
1.8Hz
Number of Trials
Number of Spikes
8.89ms
Latency (ms)

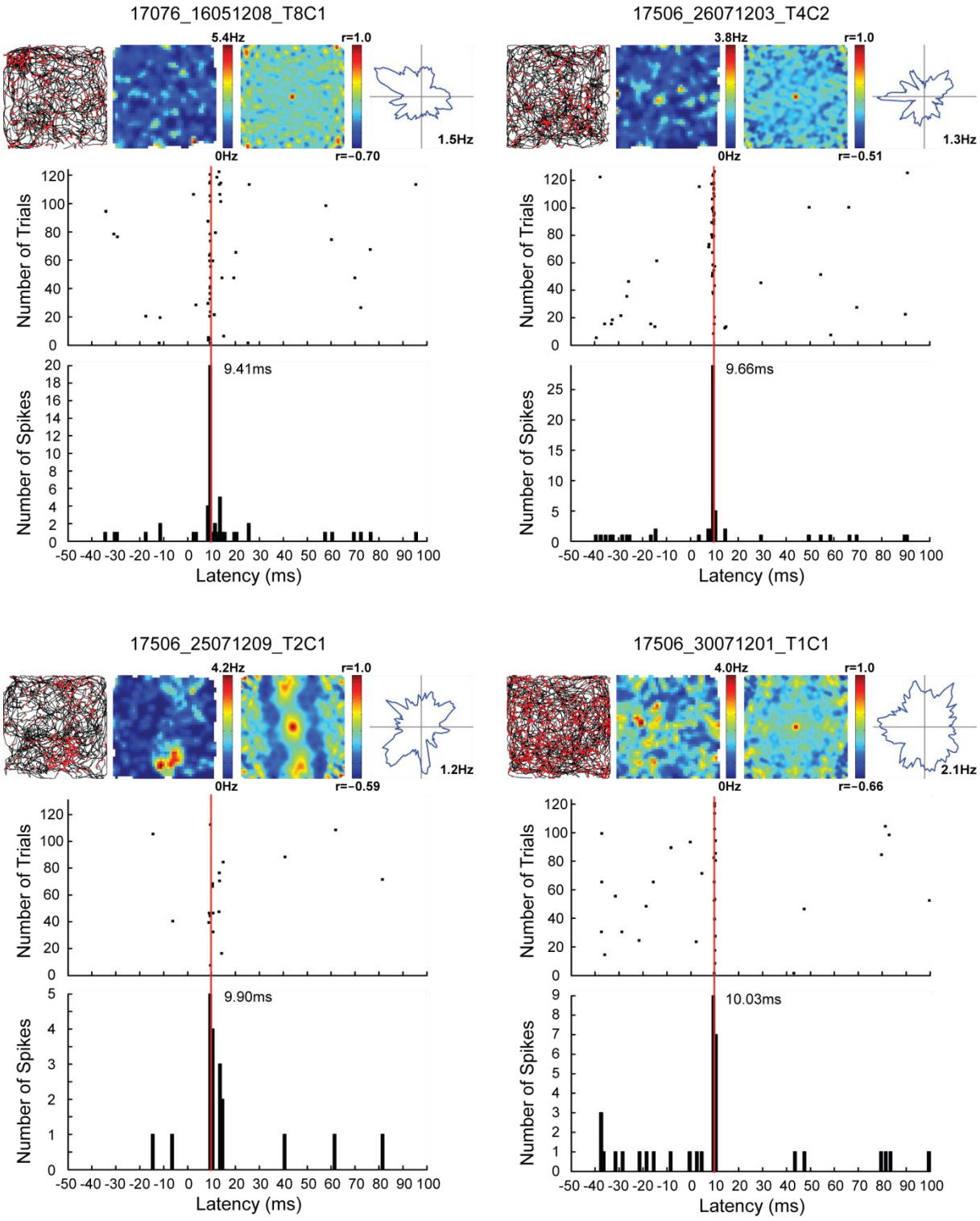
17076_16051208_T8C1
5.4Hz
r=1.0
0Hz
r=−0.70
1.5Hz
Number of Trials
Number of Spikes
9.41ms
Latency (ms)
17506_26071203_T4C2
3.8Hz
r=1.0
0Hz
r=−0.51
1.3Hz
Number of Trials
Number of Spikes
9.66ms
Latency (ms)
17506_25071209_T2C1
4.2Hz
r=1.0
0Hz
r=−0.59
1.2Hz
Number of Trials
Number of Spikes
9.90ms
Latency (ms)
17506_30071201_T1C1
4.0Hz
r=1.0
0Hz
r=−0.66
2.1Hz
Number of Trials
Number of Spikes
10.03ms
Latency (ms)

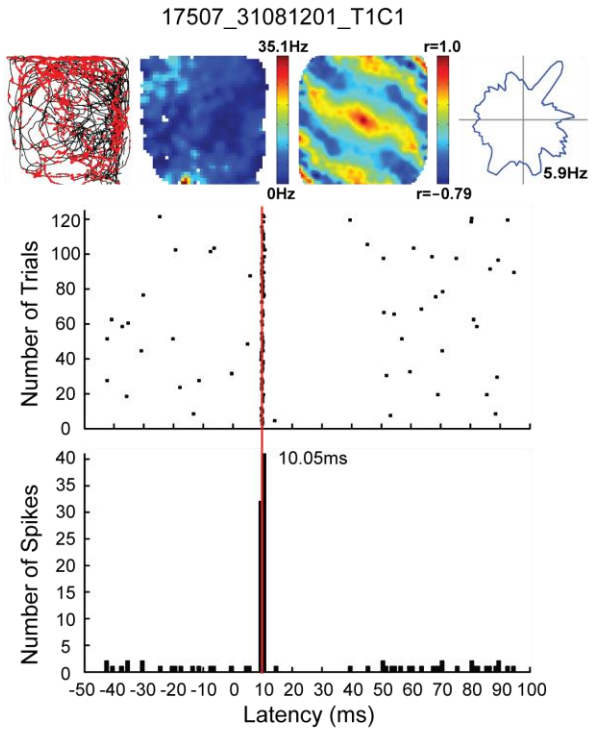
17507_31081201_T1C1
35.1Hz
r=1.0
0Hz
r=−0.79
5.9Hz
Number of Trials
Number of Spikes
10.05ms
Latency (ms)

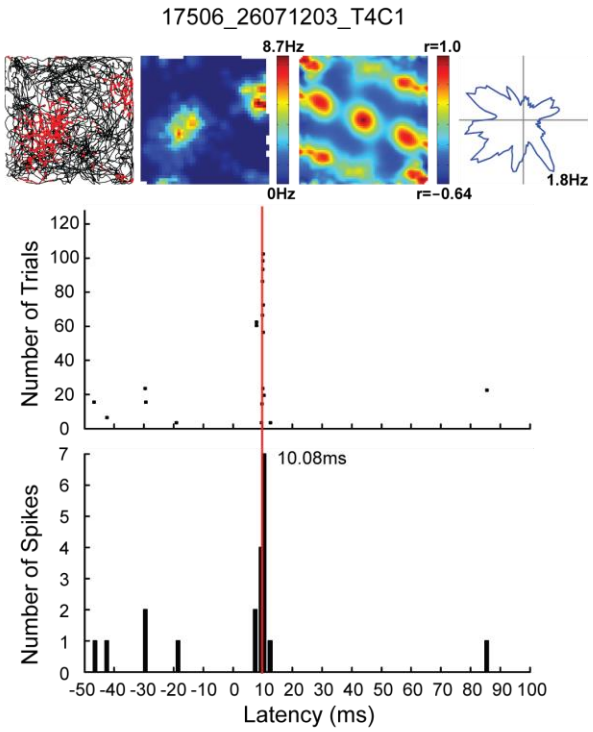
17506_26071203_T4C1
8.7Hz
r=1.0
0Hz
r=−0.64
1.8Hz
Number of Trials
Number of Spikes
10.08ms
Latency (ms)

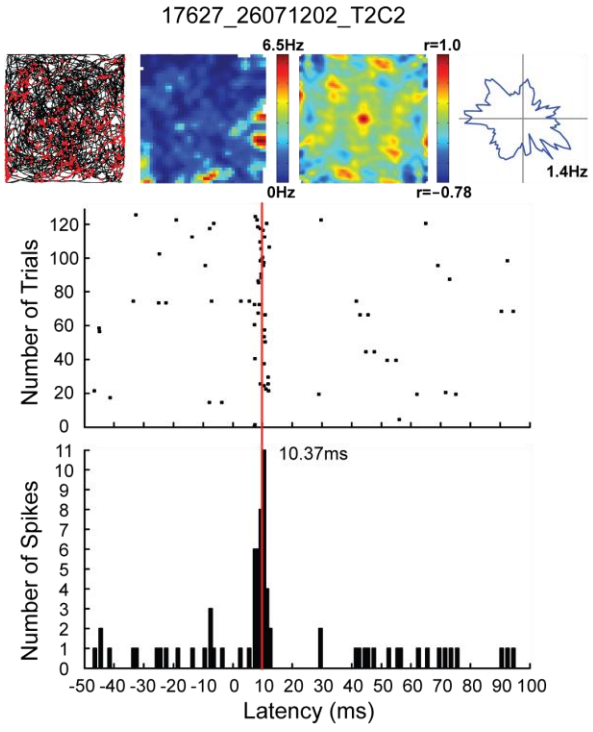
17627_26071202_T2C2
6.5Hz
r=1.0
0Hz
r=−0.78
1.4Hz
Number of Trials
Number of Spikes
10.37ms
Latency (ms)

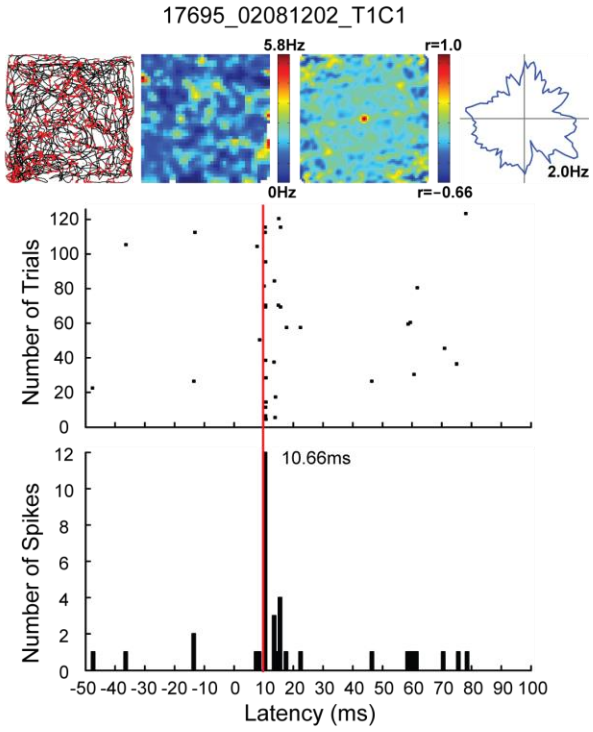
17695_02081202_T1C1
5.8Hz
r=1.0
0Hz
r=−0.66
2.0Hz
Number of Trials
Number of Spikes
10.66ms
Latency (ms)

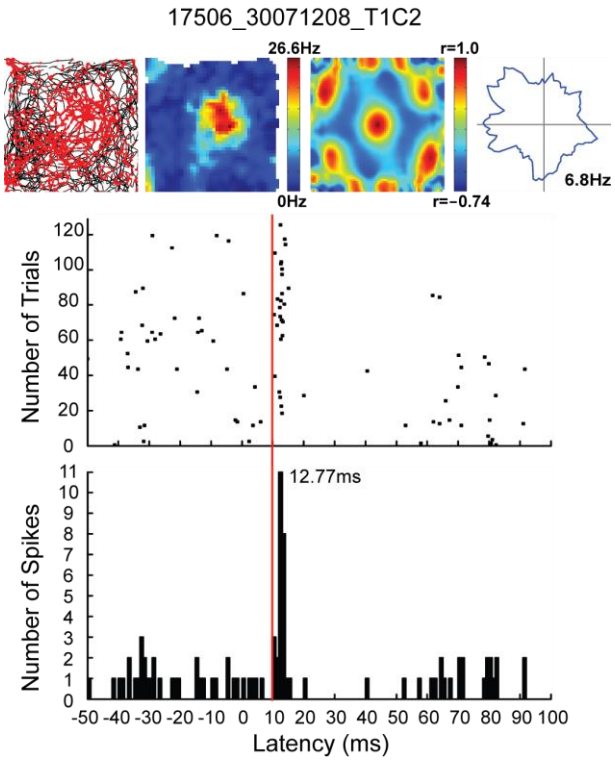


**Fig. S4.** Firing patterns of all light-responsive unknown cells recorded in the MEC. Each panel corresponds to one cell with the session's number identified on top. Panels are shown in increasing order of observed response latencies. Top section, from left to right: i. rat's running path (black line) with superimposed spike locations (red dot); ii. firing rate map with maximum and minimum firing-rate values indicated on the color-coded bar; iii. autocorrelogram extracted from firing rate map with maximum and minimum correlation values indicated on the color-coded bar; iv. polar map showing firing rate as a function of rat's head direction with peak rate indicated. Middle section: spike raster showing spike distribution before and after laser stimulation. Bottom section: spike histogram corresponding to the spike raster with response latency indicated (red line corresponds to 10 ms time stamp).

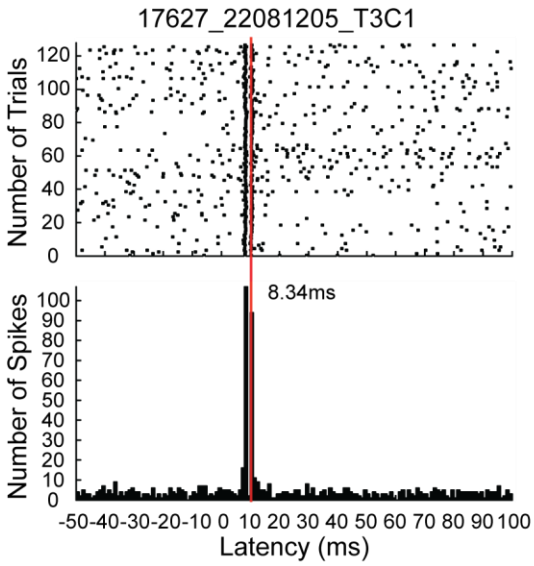
17627_22081205_T3C1
Number of Trials
Number of Spikes
8.34ms
Latency (ms)

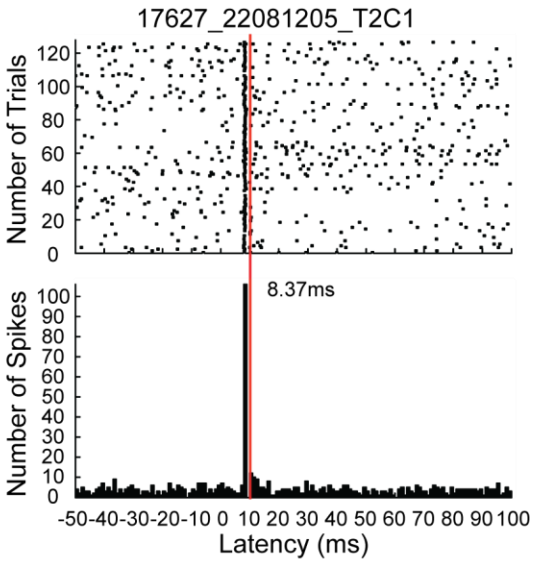
17627_22081205_T2C1
Number of Trials
Number of Spikes
8.37ms
Latency (ms)

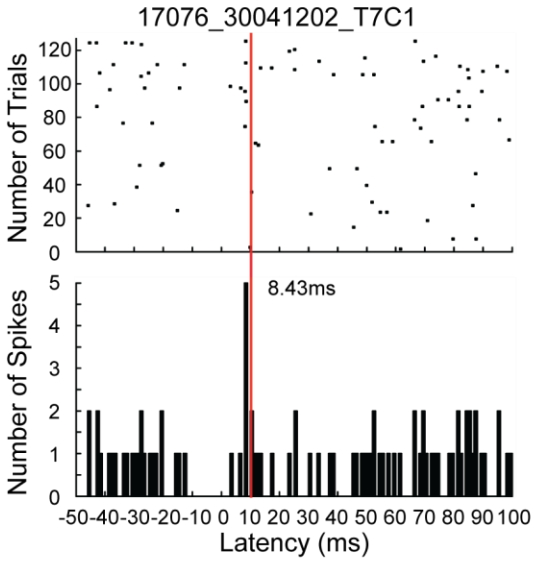
17076_30041202_T7C1
Number of Trials
Number of Spikes
8.43ms
Latency (ms)

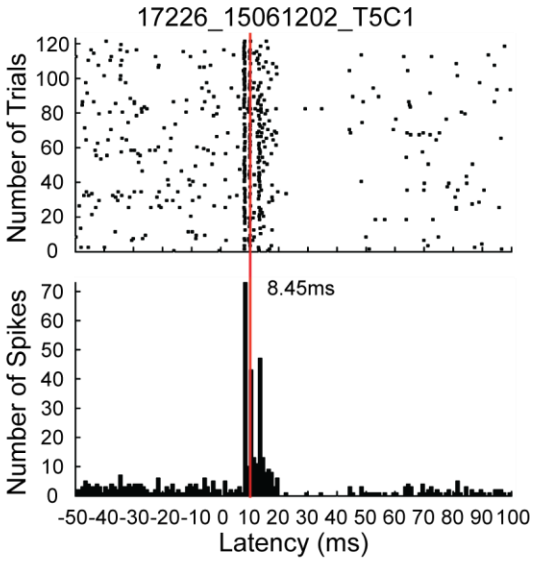
17226_15061202_T5C1
Number of Trials
Number of Spikes
8.45ms
Latency (ms)

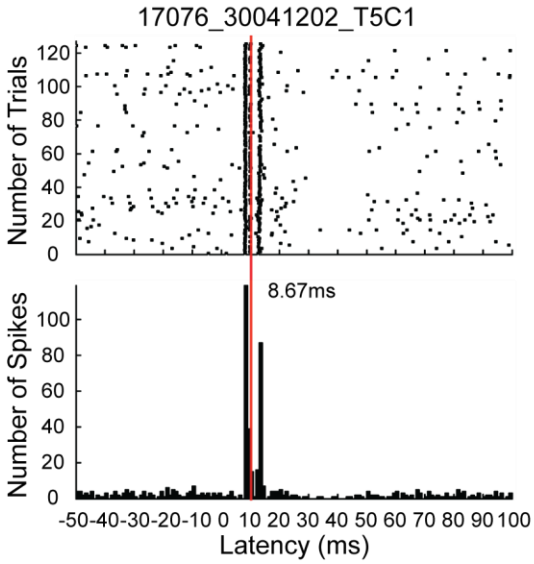
17076_30041202_T5C1
Number of Trials
Number of Spikes
8.67ms
Latency (ms)

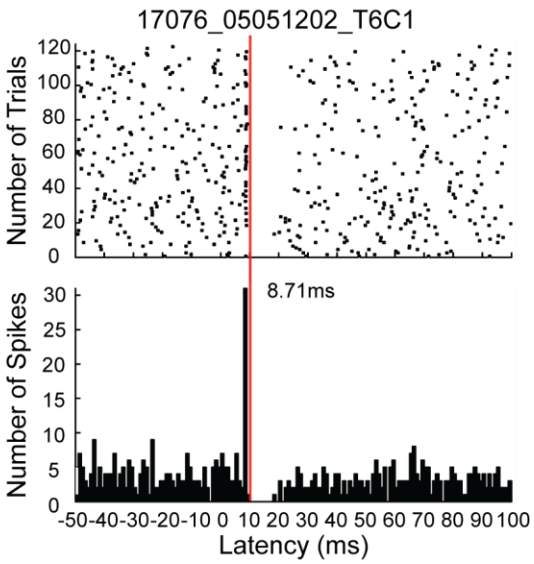
17076_05051202_T6C1
Number of Trials
Number of Spikes
8.71ms
Latency (ms)

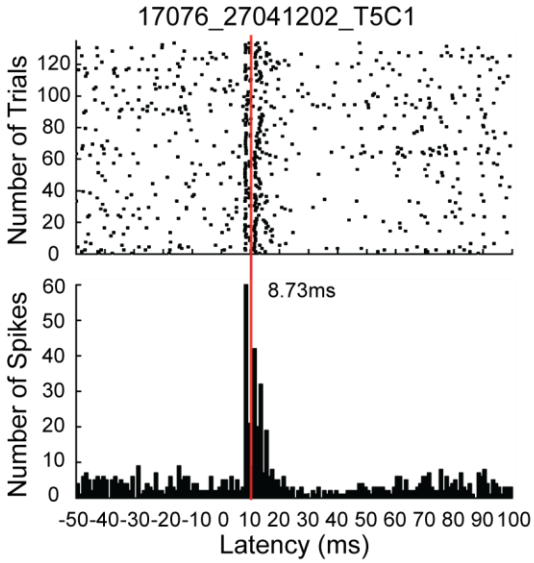
17076_27041202_T5C1
Number of Trials
Number of Spikes
8.73ms
Latency (ms)

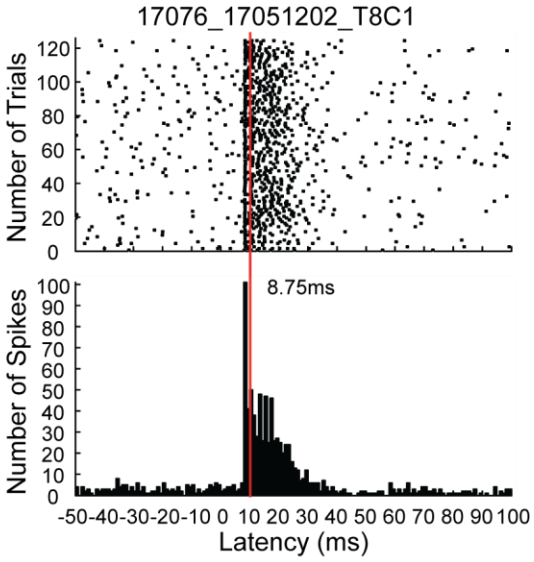
17076_17051202_T8C1
Number of Trials
Number of Spikes
8.75ms
Latency (ms)

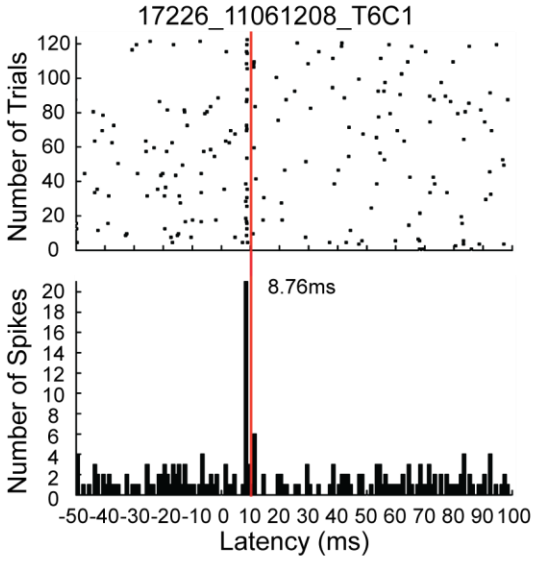
17226_11061208_T6C1
Number of Trials
Number of Spikes
8.76ms
Latency (ms)

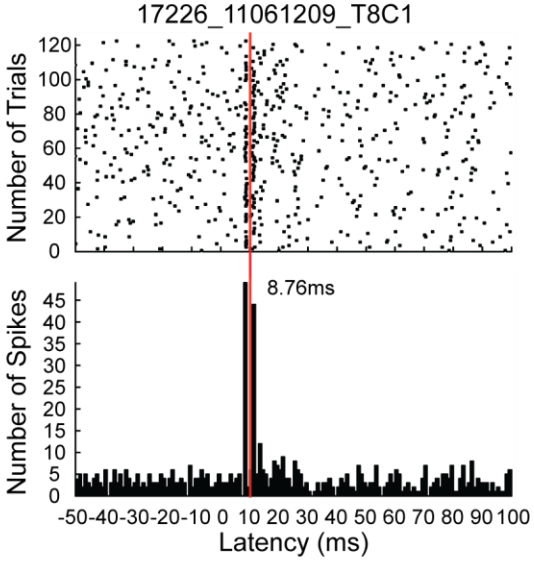
17226_11061209_T8C1
Number of Trials
Number of Spikes
8.76ms
Latency (ms)

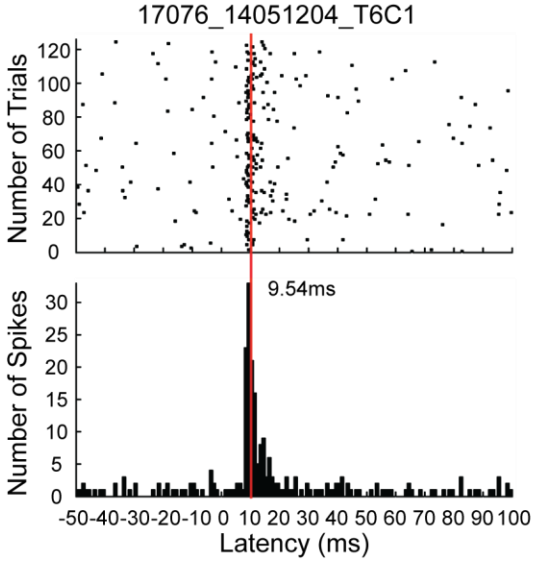
17076_14051204_T6C1
Number of Trials
Number of Spikes
9.54ms
Latency (ms)

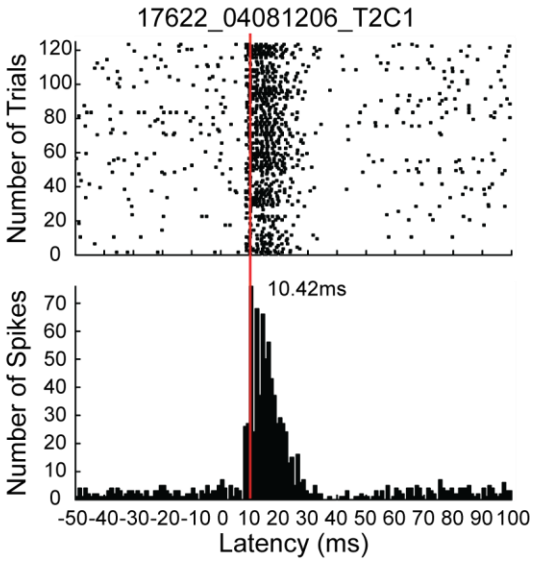
17622_04081206_T2C1
Number of Trials
Number of Spikes
10.42ms
Latency (ms)

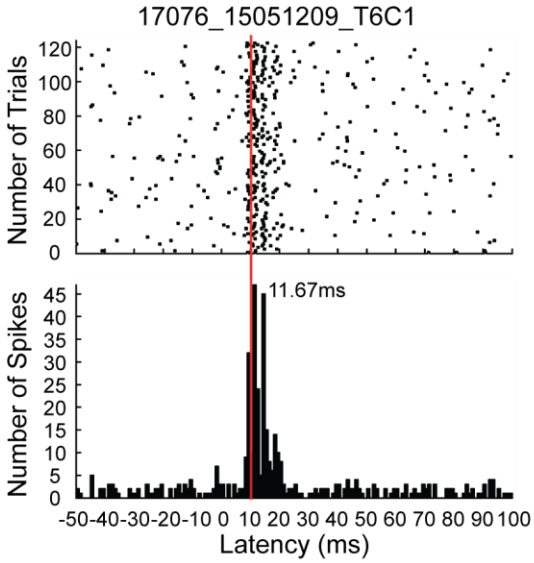
17076_15051209_T6C1
Number of Trials
Number of Spikes
11.67ms
Latency (ms)

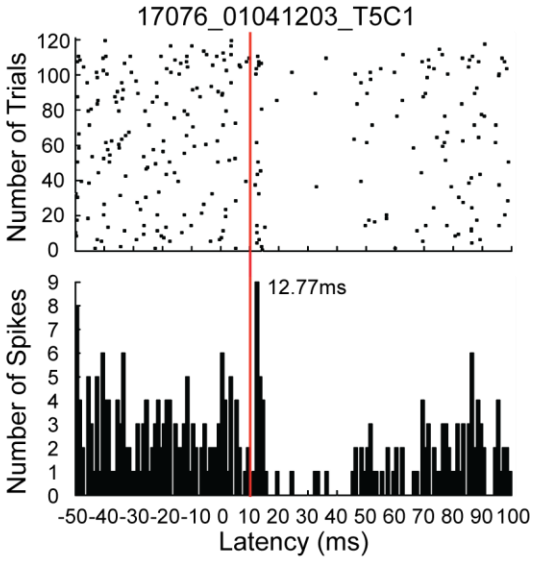
17076_01041203_T5C1
Number of Trials
Number of Spikes
12.77ms
Latency (ms)

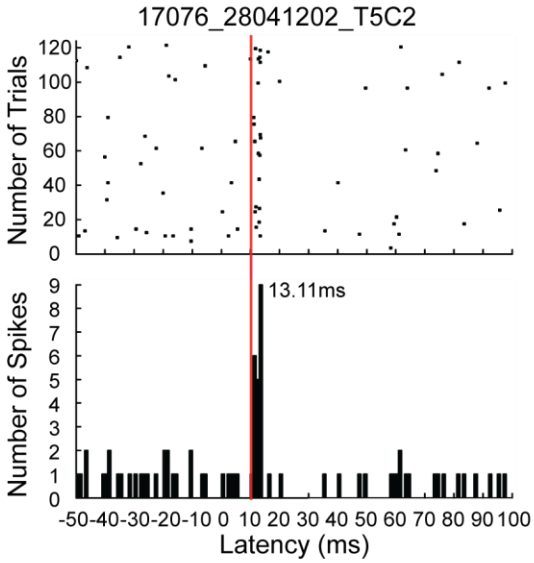
17076_28041202_T5C2
Number of Trials
Number of Spikes
13.11ms
Latency (ms)

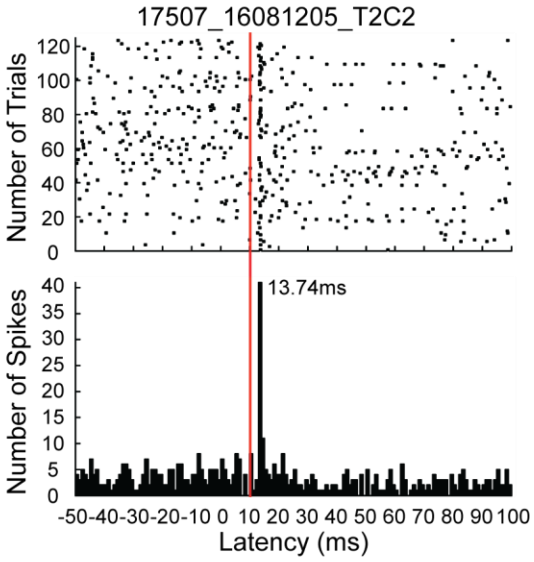
17507_16081205_T2C2
Number of Trials
Number of Spikes
13.74ms
Latency (ms)

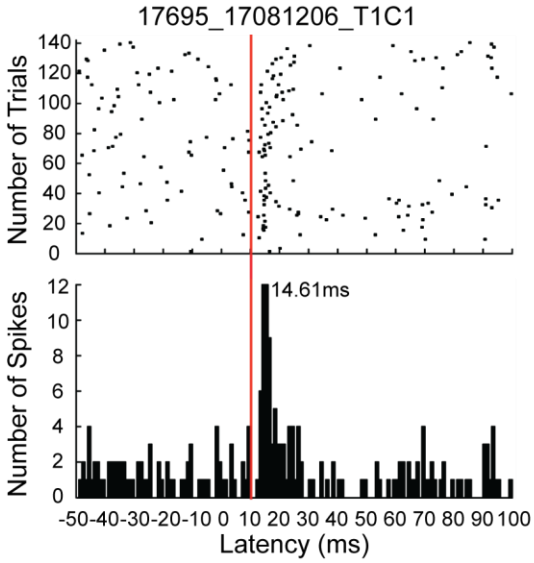
17695_17081206_T1C1
Number of Trials
Number of Spikes
14.61ms
Latency (ms)

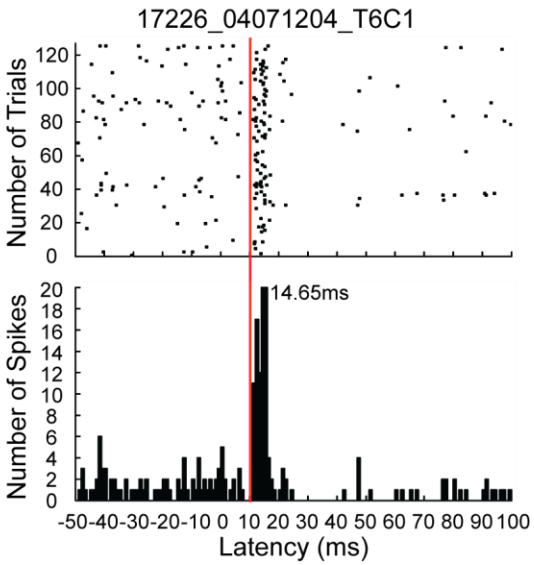
17226_04071204_T6C1
Number of Trials
Number of Spikes
14.65ms
Latency (ms)

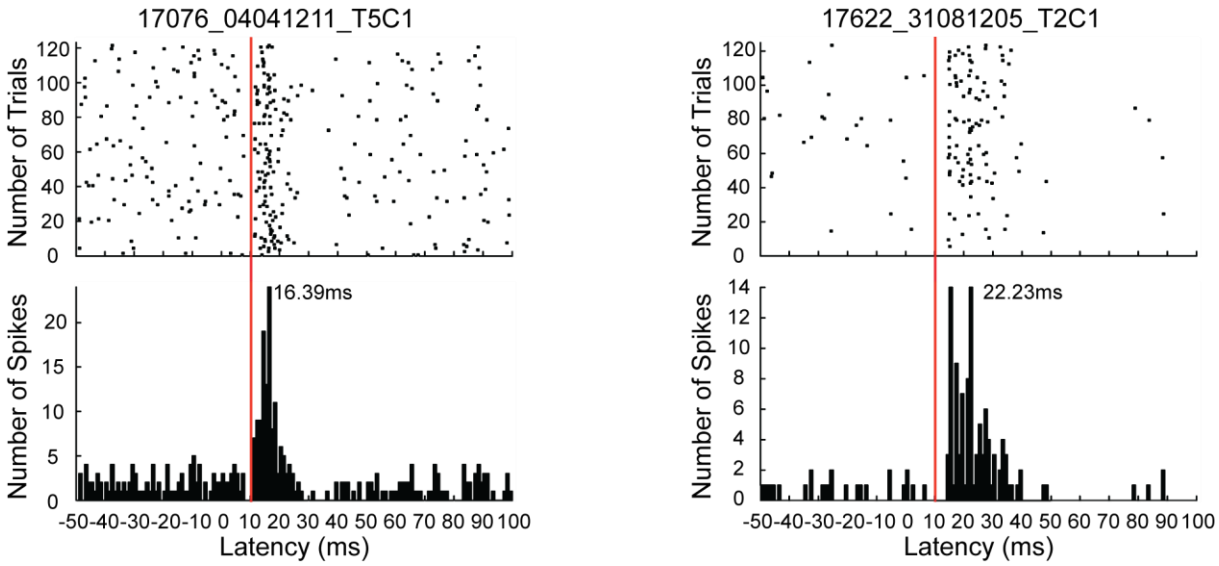


**Fig. S5.** Spike distributions of all photoresponsive interneurons recorded in the MEC. Each panel corresponds to one cell with the session's number identified on top. Panels are shown in increasing order of observed response latencies. Spike raster (top) and spike histogram (bottom) are shown, whereas figures indicating spatial firing patterns (rat's running path, firing rate map, autocorrelogram, and polar map) during the behavioral task are omitted, as they would only indicate lack of spatial and directional modulation. In the spike histogram mean response latency is indicated and the red line corresponds to a 10 ms time stamp.

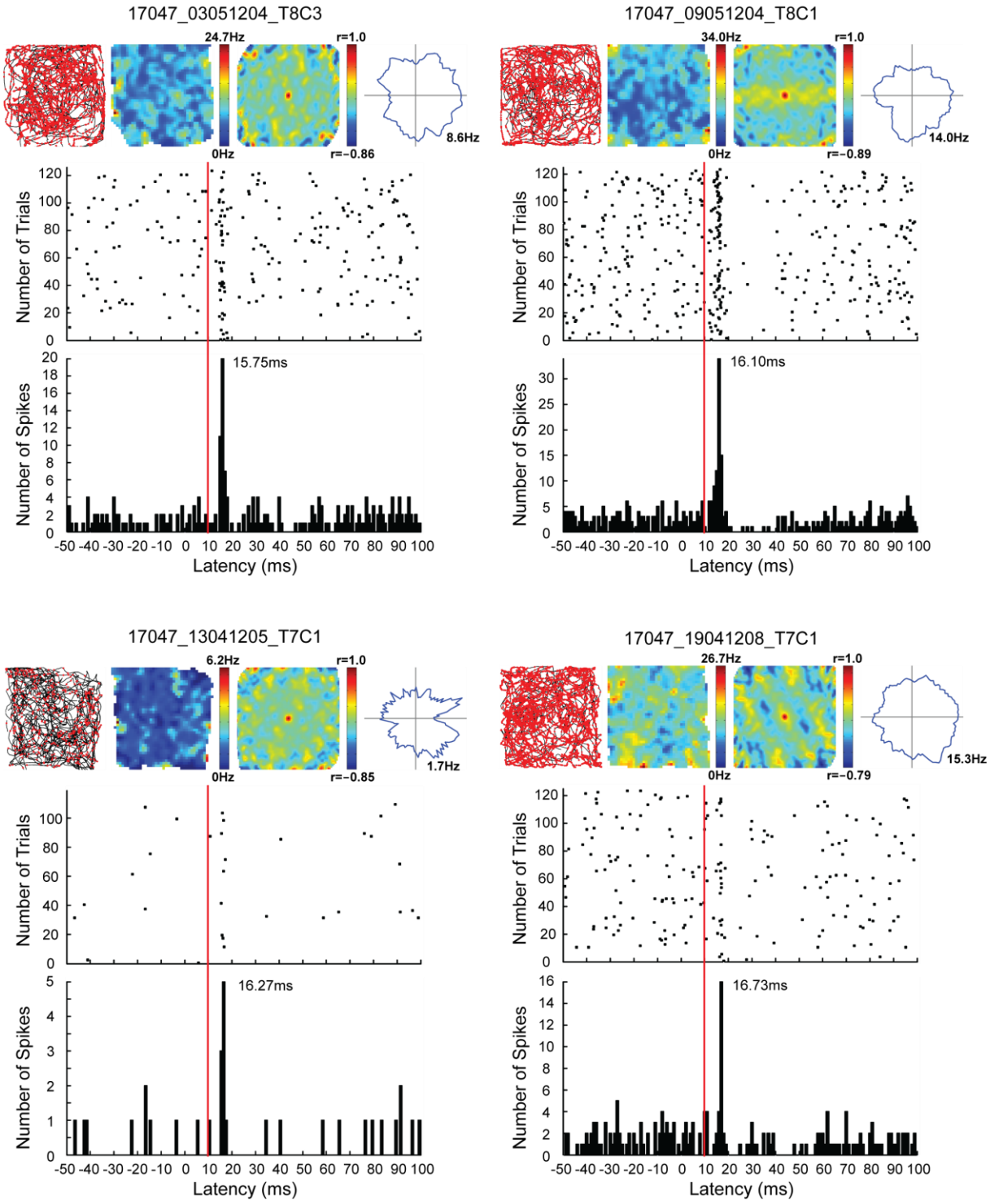
17047_03051204_T8C3
24.7Hz
r=1.0
0Hz
r=−0.86
8.6Hz
Number of Trials
Number of Spikes
15.75ms
Latency (ms)
17047_09051204_T8C1
34.0Hz
r=1.0
0Hz
r=−0.89
14.0Hz
Number of Trials
Number of Spikes
16.10ms
Latency (ms)
17047_13041205_T7C1
6.2Hz
r=1.0
0Hz
r=−0.85
1.7Hz
Number of Trials
Number of Spikes
16.27ms
Latency (ms)
17047_19041208_T7C1
26.7Hz
r=1.0
0Hz
r=−0.79
15.3Hz
Number of Trials
Number of Spikes
16.73ms
Latency (ms)

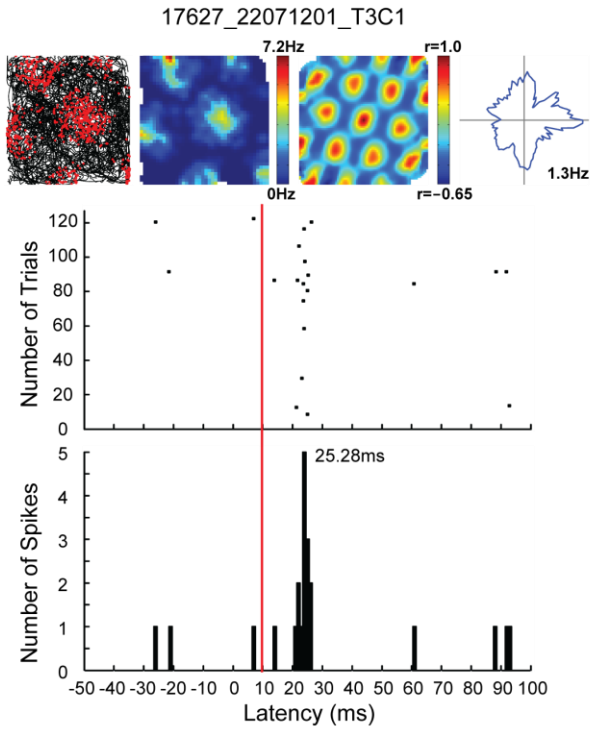


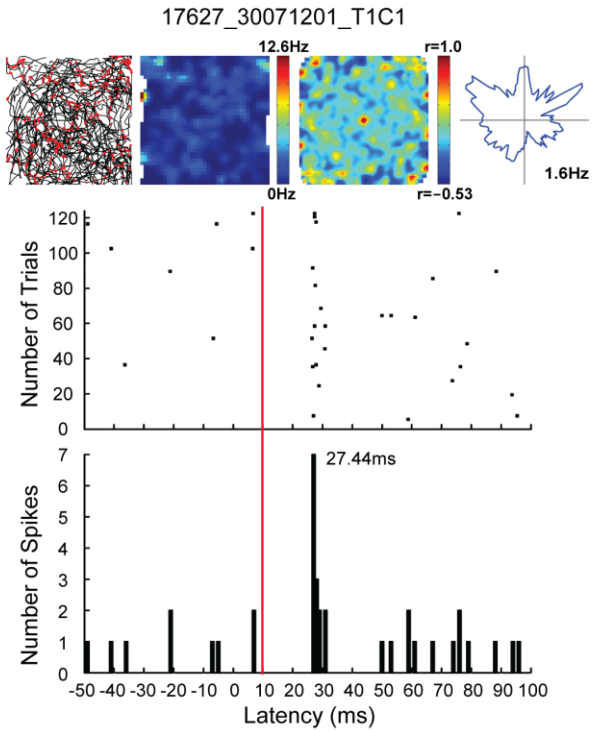


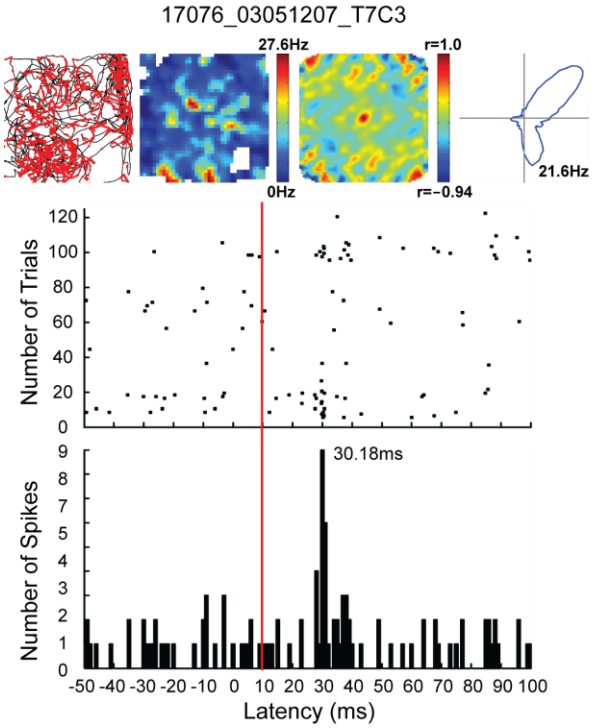


**Fig. S6.** Firing patterns of all MEC neurons that were responsive to light stimulation in hippocampal CA1 pyramidal cell layer. Each panel corresponds to one cell with the session's number identified on top. Panels are shown in increasing order of observed response latencies. Top section, from left to right: i. rat's running path (black line) with superimposed spike locations (red dot); ii. firing rate map with maximum and minimum firing-rate values indicated on the color-coded bar; iii. autocorrelogram extracted from firing rate map with maximum and minimum correlation values indicated on the color-coded bar; iv. polar map showing firing rate as a function of rat's head direction with peak rate indicated. Middle section: spike raster showing spike distribution before and after laser stimulation. Bottom section: spike histogram corresponding to the spike raster with response latency indicated (red line corresponds to 10 ms time stamp). Please note consistently longer response latencies compared to the ones observed when the laser was shone in the MEC itself (Figs. 18, 20).

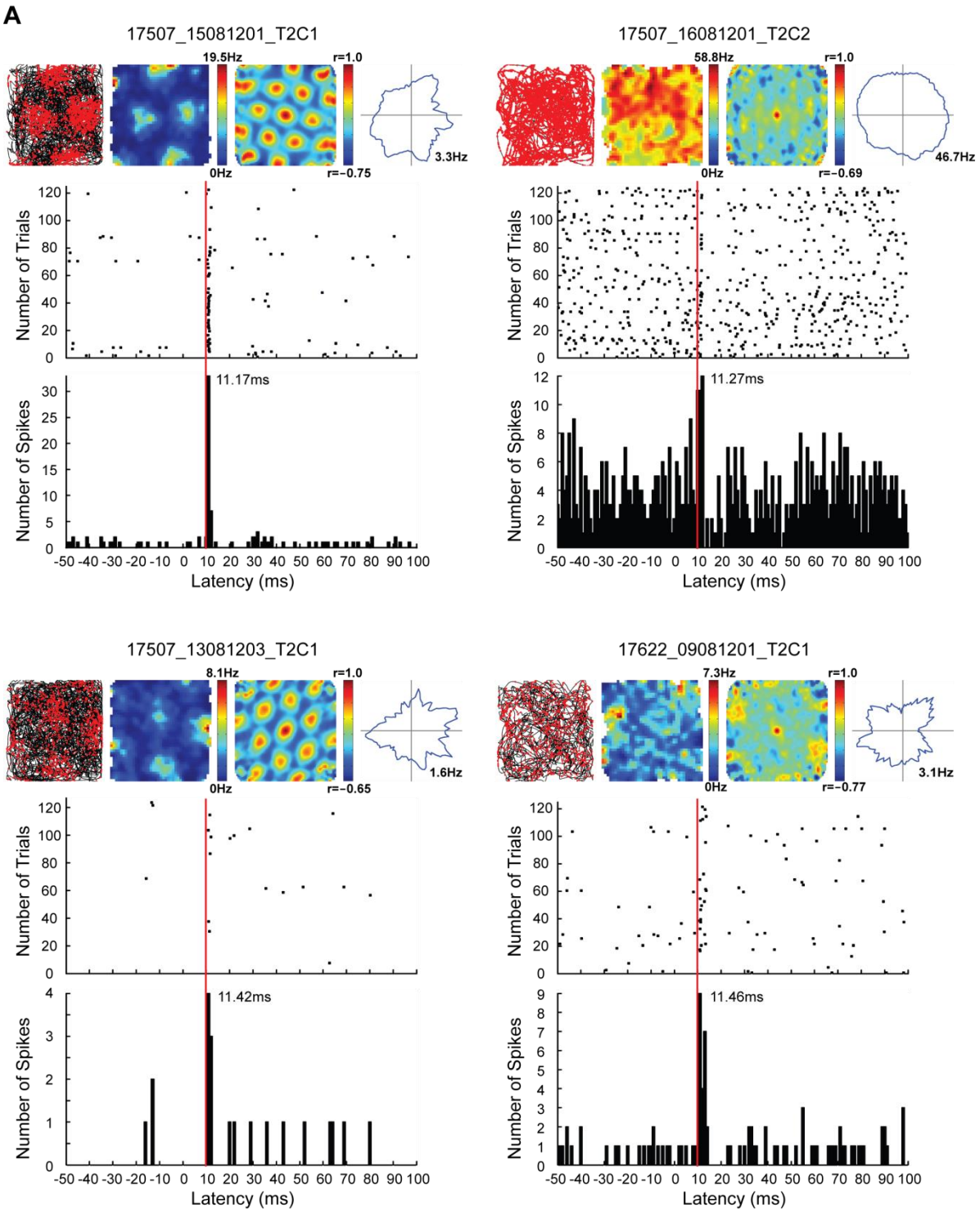
A
17507_15081201_T2C1
19.5Hz
r=1.0
0Hz
r=−0.75
3.3Hz
Number of Trials
Number of Spikes
11.17ms
Latency (ms)
17507_16081201_T2C2
58.8Hz
r=1.0
0Hz
r=−0.69
46.7Hz
Number of Trials
Number of Spikes
11.27ms
Latency (ms)
17507_13081203_T2C1
8.1Hz
r=1.0
0Hz
r=−0.65
1.6Hz
Number of Trials
Number of Spikes
11.42ms
Latency (ms)
17622_09081201_T2C1
7.3Hz
r=1.0
0Hz
r=−0.77
3.1Hz
Number of Trials
Number of Spikes
11.46ms
Latency (ms)

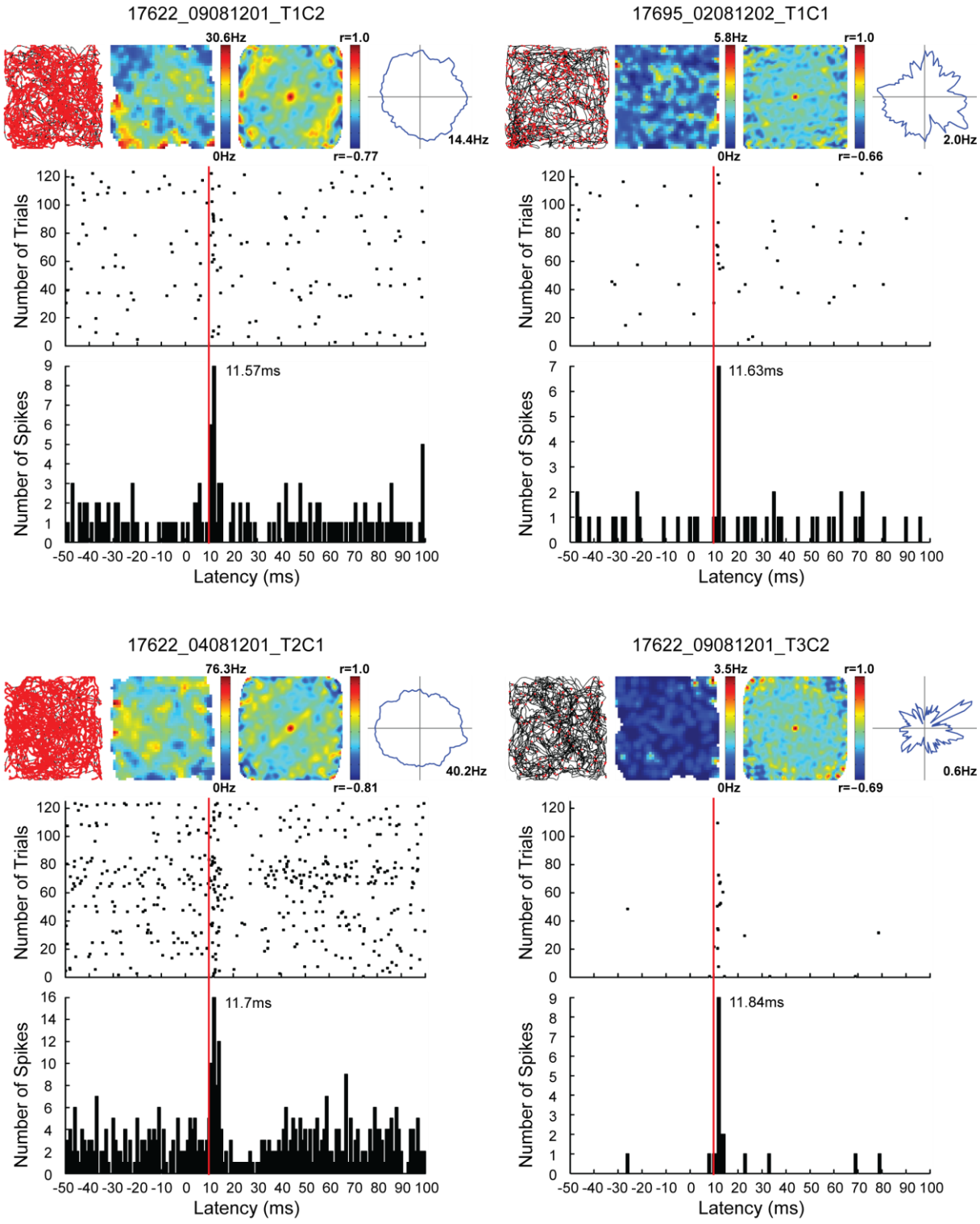
17622_09081201_T1C2
30.6Hz
r=1.0
0Hz
r=−0.77
14.4Hz
Number of Trials
Number of Spikes
11.57ms
Latency (ms)
17695_02081202_T1C1
5.8Hz
r=1.0
0Hz
r=−0.66
2.0Hz
Number of Trials
Number of Spikes
11.63ms
Latency (ms)
17622_04081201_T2C1
76.3Hz
r=1.0
0Hz
r=−0.81
40.2Hz
Number of Trials
Number of Spikes
11.7ms
Latency (ms)
17622_09081201_T3C2
3.5Hz
r=1.0
0Hz
r=−0.69
0.6Hz
Number of Trials
Number of Spikes
11.84ms
Latency (ms)

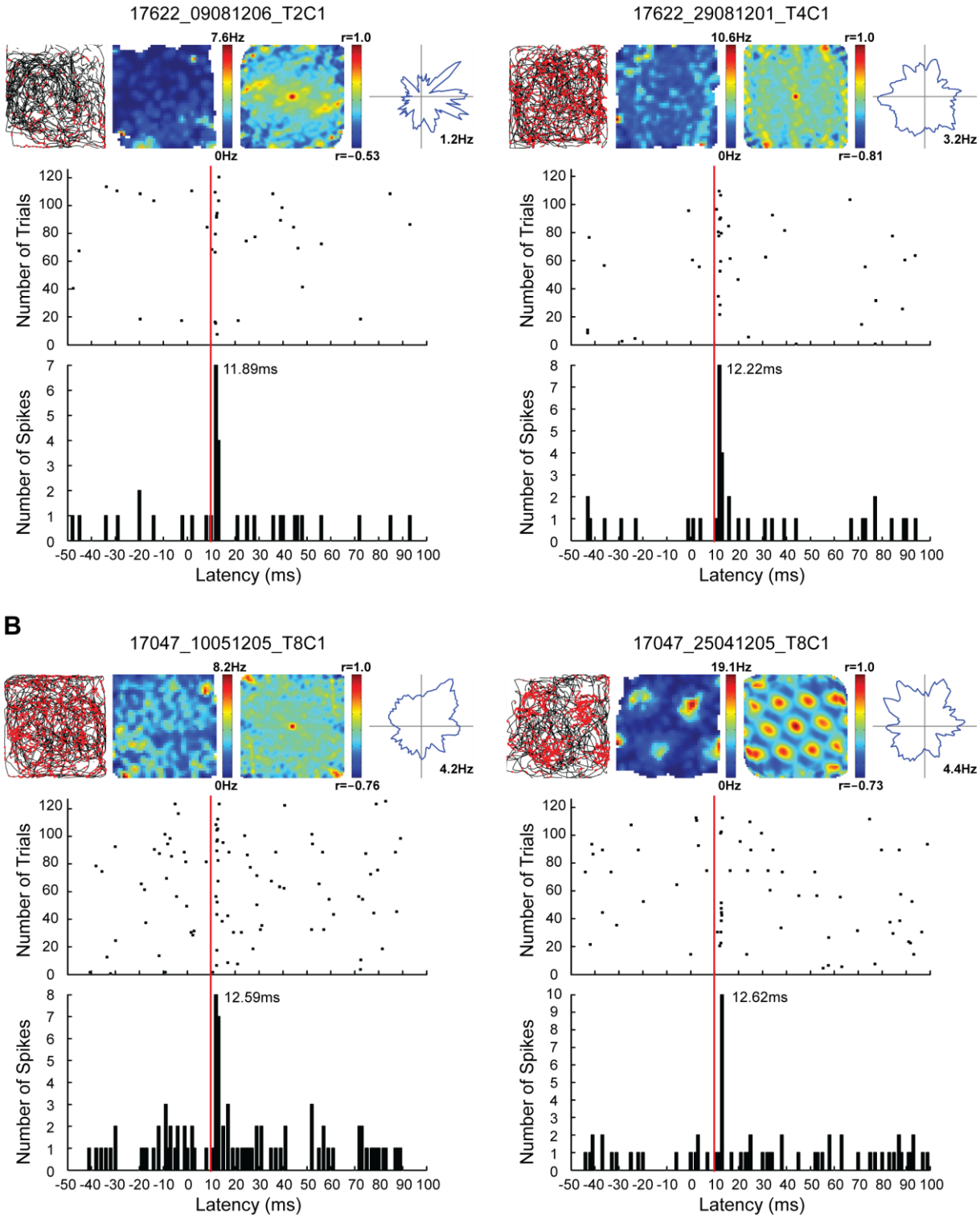


**Fig. S7.** Firing patterns of all MEC recorded neurons that were responsive to laser stimulation in the angular bundle (A) or the perforant path termination zone (B). **(A)** Firing patterns of MEC neurons that were responsive to laser stimulation in the angular bundle. Each panel corresponds to one cell with the session's number identified on top. Panels are shown in increasing order of observed response latencies. Top section, from left to right: i. rat's running path (black line) with superimposed spike locations (red dot); ii. firing rate map with maximum and minimum firing-rate values indicated on the color-coded bar; iii. autocorrelogram extracted from firing rate map with maximum and minimum correlation values indicated on the color-coded bar; iv. polar map showing firing rate as a function of rat's head direction with peak rate indicated. Middle section: spike raster showing spike

distribution before and after laser stimulation. Bottom section: spike histogram corresponding to the spike raster with response latency indicated (red line corresponds to 10 ms time stamp). **(B)** Firing patterns of MEC neurons that were responsive to laser stimulation in the angular bundle. Ordering and organization of the panels is identical to one used in (A).

# REFERENCES


1. J. O'Keefe, J. Dostrovsky, The hippocampus as a spatial map. Preliminary evidence from unit activity in the freely-moving rat. *Brain Res.* **34**, 171 (1971).
2. M. Fyhn, S. Molden, M. P. Witter, E. I. Moser, M.-B. Moser, Spatial representation in the entorhinal cortex. *Science* **305**, 1258 (2004).
3. F. Sargolini *et al.*, Conjunctive representation of position, direction, and velocity in entorhinal cortex. *Science* **312**, 758 (2006).
4. T. Solstad, C. N. Boccara, E. Kropff, M.-B. Moser, E. I. Moser, Representation of geometric borders in the entorhinal cortex. *Science* **322**, 1865 (2008).
5. J. O'Keefe, Place units in the hippocampus of the freely moving rat. *Exp. Neurol.* **51**, 78 (1976).
6. T. Hafting, M. Fyhn, S. Molden, M.-B. Moser, E. I. Moser, Microstructure of a spatial map in the entorhinal cortex. *Nature* **436**, 801 (2005).
7. J. Taube, R. Muller, J. Ranck, Head-direction cells recorded from the postsubiculum in freely moving rats. I. Description and quantitative analysis. *The Journal of Neuroscience* **10**, 420 (1990).
8. J. S. Taube, H. L. Burton, Head direction cell activity monitored in a novel environment and during a cue conflict situation. *J. Neurophysiol.* **74**, 1953 (1995).
9. R. Muller, J. Kubie, The effects of changes in the environment on the spatial firing of hippocampal complex-spike cells. *The Journal of Neuroscience* **7**, 1951 (1987).
10. B. L. McNaughton, F. P. Battaglia, O. Jensen, E. I. Moser, M.-B. Moser, Path integration and the neural basis of the 'cognitive map'. *Nat Rev Neurosci* **7**, 663 (2006).
11. J. O'Keefe, N. Burgess, Dual phase and rate coding in hippocampal place cells: theoretical significance and relationship to entorhinal grid cells. *Hippocampus* **15**, 853 (2005).
12. E. I. Moser, M.-B. Moser, A metric for space. *Hippocampus* **18**, 1142 (2008).
13. E. T. Rolls, S. M. Stringer, T. Elliot, Entorhinal cortex grid cells can map to hippocampal place cells by competitive learning. *Network: Computation in Neural Systems* **17**, 447 (2006).
14. J. D. Monaco, L. F. Abbott, Modular realignment of entorhinal grid cell activity as a basis for hippocampal remapping. *The Journal of Neuroscience* **31**, 9414 (2011).
15. R. F. Langston *et al.*, Development of the spatial representation system in the rat. *Science* **328**, 1576 (2010).
16. T. J. Wills, F. Cacucci, N. Burgess, J. O'Keefe, Development of the hippocampal cognitive map in preweanling rats. *Science* **328**, 1573 (2010).
17. N. M. van Strien, N. L. M. Cappaert, M. P. Witter, The anatomy of memory: an interactive overview of the parahippocampal-hippocampal network. *Nat Rev Neurosci* **10**, 272 (2009).
18. V. H. Brun *et al.*, Place cells and place recognition maintained by direct entorhinal-hippocampal circuitry. *Science* **296**, 2243 (2002).
19. V. H. Brun *et al.*, Impaired spatial representation in CA1 after lesion of direct input from entorhinal cortex. *Neuron* **57**, 290 (2008).
20. T. Van Cauter, B. Poucet, E. Save, Unstable CA1 place cell representation in rats with entorhinal cortex lesions. *Eur. J. Neurosci.* **27**, 1933 (2008).
21. J. K. Leutgeb, S. Leutgeb, M.-B. Moser, E. I. Moser, Pattern separation in the dentate gyrus and CA3 of the hippocampus. *Science* **315**, 961 (2007).
22. C. B. Canto, F. G. Wouterlood, M. P. Witter, What does the anatomical organization of the entorhinal cortex tell us? *Neural Plas.* **2008**, Article ID 381243 (2008).
23. M. Witter, in *The Mouse Nervous System,* W. Charles, P. George, L. Puelles, Eds. (Academic Press, San Diego, 2012), pp. 112-139.
24. T. Klausberger, P. Somogyi, Neuronal diversity and temporal dynamics: the unity of hippocampal circuit operations. *Science* **321**, 53 (2008).

25. K. M. Kerr, K. L. Agster, S. C. Furtak, R. D. Burwell, Functional neuroanatomy of the parahippocampal region: the lateral and medial entorhinal areas. *Hippocampus* **17**, 697 (2007).
26. E. I. Moser, M. P. Witter, M.-B. Moser, in *Hanbook of Brain Microcircuits,* G. Shepherd, S. Grillner, Eds. (Oxford University Press, USA, 2010), pp. 175 - 189.
27. R. Klink, A. Alonso, Morphological characteristics of layer II projection neurons in the rat medial entorhinal cortex. *Hippocampus* **7**, 571 (1997).
28. B. Tahvildari, A. Alonso, Morphological and electrophysiological properties of lateral entorhinal cortex layers II and III principal neurons. *The Journal of Comparative Neurology* **491**, 123 (2005).
29. B. N. Hamam, D. G. Amaral, A. A. Alonso, Morphological and electrophysiological characteristics of layer V neurons of the rat lateral entorhinal cortex. *The Journal of Comparative Neurology* **451**, 45 (2002).
30. B. N. Hamam, T. E. Kennedy, A. Alonso, D. G. Amaral, Morphological and electrophysiological characteristics of layer V neurons of the rat medial entorhinal cortex. *The Journal of Comparative Neurology* **418**, 457 (2000).
31. E. C. Tolman, Cognitive maps in rats and men. *Psychol. Rev.* **55**, 189 (1948).
32. K. B. Kjelstrup *et al.*, Finite scale of spatial representation in the hippocampus. *Science* **321**, 140 (2008).
33. J. O'Keefe, J. Dostrovsky, *Hippocampus as a cognitive map*. (Clarendon Press, Oxford, 1978).
34. L. L. Colgin, E. I. Moser, M.-B. Moser, Understanding memory through hippocampal remapping. *Trends Neurosci.* **31**, 469 (2008).
35. M. Wilson, B. McNaughton, Dynamics of the hippocampal ensemble code for space. *Science* **261**, 1055 (1993).
36. A. D. Redish *et al.*, Independence of firing correlates of anatomically proximate hippocampal pyramidal cells. *The Journal of Neuroscience* **21**, RC134 (2001).
37. D. Derdikman, E. I. Moser, A manifold of spatial maps in the brain. *Trends in Cognitive Sciences* **14**, 561 (2010).
38. B. L. McNaughton, C. A. Barnes, J. Meltzer, R. J. Sutherland, Hippocampal granule cells are necessary for normal spatial learning but not for spatially-selective pyramidal cell discharge. *Exp. Brain Res.* **76**, 485 (1989).
39. L. M. Frank, E. N. Brown, M. Wilson, Trajectory encoding in the hippocampus and entorhinal cortex. *Neuron* **27**, 169 (2000).
40. C. Barry, D. Bush, From A to Z: a potential role for grid cells in spatial navigation. *Neural Systems & Circuits* **2**, 6 (2012).
41. C. N. Boccara *et al.*, Grid cells in pre- and parasubiculum. *Nat. Neurosci.* **13**, 987 (2010).
42. H. Stensola *et al.*, The entorhinal grid map is discretized. *Nature* **492**, 72 (2012).
43. J. B. Ranck, Head-direction cells in the deep cell layers of dorsal presubiculum in freely moving rats. *Society for Neuroscience Abstracts* **10**, (1984).
44. J. S. Taube, The head direction signal: origins and sensory-motor integration. *Annu. Rev. Neurosci.* **30**, 181 (2007).
45. P. A. Naber, M. Caballero-Bleda, B. Jorritsma-Byham, M. P. Witter, Parallel input to the hippocampal memory system through peri- and postrhinal cortices. *Neuroreport* **8**, 2617 (1997).
46. R. D. Burwell, D. G. Amaral, Perirhinal and postrhinal cortices of the rat: interconnectivity and connections with the entorhinal cortex. *The Journal of Comparative Neurology* **391**, 293 (1998).
47. S. C. Furtak, S.-M. Wei, K. L. Agster, R. D. Burwell, Functional neuroanatomy of the parahippocampal region in the rat: the perirhinal and postrhinal cortices. *Hippocampus* **17**, 709 (2007).
48. C. L. Dolorfo, D. G. Amaral, Entorhinal cortex of the rat: organization of intrinsic connections. *The Journal of Comparative Neurology* **398**, 49 (1998).

49. N. Ishizuka, J. Weber, D. G. Amaral, Organization of intrahippocampal projections originating from CA3 pyramidal cells in the rat. *The Journal of Comparative Neurology* **295**, 580 (1990).
50. D. G. Amaral, C. Dolorfo, P. Alvarez-Royo, Organization of CA1 projections to the subiculum: a PHA-L analysis in the rat. *Hippocampus* **1**, 415 (1991).
51. X. G. Li, P. Somogyi, A. Ylinen, G. Buzsáki, The hippocampal CA3 network: an in vivo intracellular labeling study. *The Journal of Comparative Neurology* **339**, 181 (1994).
52. P. A. Naber, F. H. Lopes da Silva, M. P. Witter, Reciprocal connections between the entorhinal cortex and hippocampal fields CA1 and the subiculum are in register with the projections from CA1 to the subiculum. *Hippocampus* **11**, 99 (2001).
53. G. Neves, S. F. Cooke, T. V. P. Bliss, Synaptic plasticity, memory and the hippocampus: a neural network approach to causality. *Nat Rev Neurosci* **9**, 65 (2008).
54. A. S. Etienne, K. J. Jeffery, Path integration in mammals. *Hippocampus* **14**, 180 (2004).
55. M. L. Mittelstaedt, H. Mittelstaedt, Homing by path integration in a mammal. *Naturwissenschaften* **67**, 566 (1980).
56. C. Parron, E. Save, Evidence for entorhinal and parietal cortices involvement in path integration in the rat. *Exp. Brain Res.* **159**, 349 (2004).
57. M. Fyhn, T. Hafting, A. Treves, M.-B. Moser, E. I. Moser, Hippocampal remapping and grid realignment in entorhinal cortex. *Nature* **446**, 190 (2007).
58. C. Barry, R. Hayman, N. Burgess, K. J. Jeffery, Experience-dependent rescaling of entorhinal grids. *Nat. Neurosci.* **10**, 682 (2007).
59. T. Hafting, M. Fyhn, T. Bonnevie, M.-B. Moser, E. I. Moser, Hippocampus-independent phase precession in entorhinal grid cells. *Nature* **453**, 1248 (2008).
60. T. Solstad, E. I. Moser, G. T. Einevoll, From grid cells to place cells: a mathematical model. *Hippocampus* **16**, 1026 (2006).
61. C. Kentros *et al.*, Abolition of long-term stability of new hippocampal place cell maps by NMDA receptor blockade. *Science* **280**, 2121 (1998).
62. J. Koenig, A. N. Linder, J. K. Leutgeb, S. Leutgeb, The spatial periodicity of grid cells is not sustained during reduced theta oscillations. *Science* **332**, 592 (2011).
63. T. Hartley, N. Burgess, C. Lever, F. Cacucci, J. O'Keefe, Modeling place fields in terms of the cortical inputs to the hippocampus. *Hippocampus* **10**, 369 (2000).
64. F. H. Crick, Thinking about the brain. *Sci. Am.* **241**, 219 (1979).
65. F. Crick, The impact of molecular biology on neuroscience. *Philos. Trans. R. Soc. Lond. B. Biol. Sci.* **354**, 2021 (1999).
66. D. Oesterhelt, W. Stoeckenius, Rhodopsin-like protein from the purple membrane of Halobacterium halobium. *Nature New Biology* **233**, 149 (1971).
67. D. Oesterhelt, W. Stoeckenius, Functions of a new photoreceptor membrane. *Proc. Natl. Acad. Sci. U. S. A.* **70**, 2853 (1973).
68. A. Matsuno-Yagi, Y. Mukohata, Two possible roles of bacteriorhodopsin; a comparative study of strains of Halobacterium halobium differing in pigmentation. *Biochem. Biophys. Res. Commun.* **78**, 237 (1977).
69. G. Nagel *et al.*, Channelrhodopsin-1: a light-gated proton channel in green algae. *Science* **296**, 2395 (2002).
70. K. Deisseroth, Optogenetics. *Nat Meth* **8**, 26 (2011).
71. E. S. Boyden, F. Zhang, E. Bamberg, G. Nagel, K. Deisseroth, Millisecond-timescale, genetically targeted optical control of neural activity. *Nat. Neurosci.* **8**, 1263 (2005).
72. J. L. Spudich, C.-S. Yang, K.-H. Jung, E. N. Spudich, Retinylidene proteins: structures and functions from archaea to humans. *Annu. Rev. Cell Dev. Biol.* **16**, 365 (2000).
73. F. Zhang *et al.*, The microbial opsin family of optogenetic tools. *Cell* **147**, 1446 (2011).
74. O. Yizhar, L. Fenno, F. Zhang, P. Hegemann, K. Diesseroth, Microbial opsins: a family of single-component tools for optical control of neural activity. *Cold Spring Harbor Protocols* **3**, 273 (2011).

75. J. Klare, I. Chizhov, M. Engelhard, in *Bioenergetics,* G. Schäfer, H. Penefsky, Eds. (Springer Berlin / Heidelberg, 2008), vol. 45, pp. 73-122.
76. L. Fenno, O. Yizhar, K. Deisseroth, The development and application of optogenetics. *Annu. Rev. Neurosci.* **34**, 389 (2011).
77. F. Zhang *et al.*, Multimodal fast optical interrogation of neural circuitry. *Nature* **446**, 633 (2007).
78. O. Yizhar, Lief E. Fenno, Thomas J. Davidson, M. Mogri, K. Deisseroth, Optogenetics in neural systems. *Neuron* **71**, 9 (2011).
79. V. Gradinaru, K. Thompson, K. Deisseroth, eNpHR: a Natronomonas halorhodopsin enhanced for optogenetic applications. *Brain Cell Biology* **36**, 129 (2008).
80. V. Gradinaru *et al.*, Molecular and cellular approaches for diversifying and extending optogenetics. *Cell* **141**, 154 (2010).
81. I. B. Witten *et al.*, Cholinergic interneurons control local circuit activity and cocaine conditioning. *Science* **330**, 1677 (2010).
82. B. Y. Chow *et al.*, High-performance genetically targetable optical neural silencing by light-driven proton pumps. *Nature* **463**, 98 (2010).
83. G. Nagel *et al.*, Channelrhodopsin-2, a directly light-gated cation-selective membrane channel. *Proceedings of the National Academy of Sciences* **100**, 13940 (2003).
84. A. Berndt, O. Yizhar, L. A. Gunaydin, P. Hegemann, K. Deisseroth, Bi-stable neural state switches. *Nat. Neurosci.* **12**, 229 (2009).
85. O. Yizhar *et al.*, Neocortical excitation/inhibition balance in information processing and social dysfunction. *Nature* **477**, 171 (2011).
86. L. A. Gunaydin *et al.*, Ultrafast optogenetic control. *Nat. Neurosci.* **13**, 387 (2010).
87. F. Zhang *et al.*, Red-shifted optogenetic excitation: a tool for fast neural control derived from Volvox carteri. *Nat. Neurosci.* **11**, 631 (2008).
88. Y. Mei, F. Zhang, Molecular tools and approaches for optogenetics. *Biol. Psychiatry* **71**, 1033 (2012).
89. F. Zhang *et al.*, Optogenetic interrogation of neural circuits: technology for probing mammalian brain structures. *Nat. Protocols* **5**, 439 (2010).
90. M. Rein, J. Deussing, The optogenetic (r)evolution. *Molecular Genetics and Genomics* **287**, 95 (2012).
91. C. Burger *et al.*, Recombinant AAV viral vectors pseudotyped with viral capsids from serotypes 1, 2, and 5 display differential efficiency and cell tropism after delivery to different regions of the central nervous system. *Mol Ther* **10**, 302 (2004).
92. F. Zhang, L.-P. Wang, E. S. Boyden, K. Deisseroth, Channelrhodopsin-2 and optical control of excitable cells. *Nat Meth* **3**, 785 (2006).
93. I. Diester *et al.*, An optogenetic toolbox designed for primates. *Nat. Neurosci.* **14**, 387 (2011).
94. M. Brenner, W. Kisseberth, Y. Su, F. Besnard, A. Messing, GFAP promoter directs astrocyte-specific expression in transgenic mice. *The Journal of Neuroscience* **14**, 1030 (1994).
95. T. Dittgen *et al.*, Lentivirus-based genetic manipulations of cortical neurons and their optical and electrophysiological monitoring in vivo. *Proceedings of the National Academy of Sciences* **101**, 18206 (2004).
96. B. R. Arenkiel *et al.*, In vivo light-induced activation of neural circuitry in transgenic mice expressing channelrhodopsin-2. *Neuron* **54**, 205 (2007).
97. M. Hagglund, L. Borgius, K. J. Dougherty, O. Kiehn, Activation of groups of excitatory neurons in the mammalian spinal cord or hindbrain evokes locomotion. *Nat. Neurosci.* **13**, 246 (2010).
98. G. P. Dugué, W. Akemann, T. Knöpfel, in *Prog. Brain Res.,* K. Thomas, S. B. Edward, Eds. (Elsevier, 2012), vol. 196, pp. 1-28.
99. T. L. Lewis, T. Mao, K. Svoboda, D. B. Arnold, Myosin-dependent targeting of transmembrane proteins to neuronal dendrites. *Nat. Neurosci.* **12**, 568 (2009).
100. T. L. Lewis, Jr., T. Mao, D. B. Arnold, A role for myosin VI in the localization of axonal proteins. *PLoS Biol* **9**, e1001021 (2011).

101. G. Buzsaki, Large-scale recording of neuronal ensembles. *Nat. Neurosci.* **7**, 446 (2004).
102. L. M. Frank, E. N. Brown, M. A. Wilson, A comparison of the firing properties of putative excitatory and inhibitory neurons from CA1 and the entorhinal cortex. *J. Neurophysiol.* **86**, 2029 (2001).
103. B. K. Kaspar *et al.*, Targeted retrograde gene delivery for neuronal protection. *Mol Ther* **5**, 50 (2002).
104. S. Melzer *et al.*, Long-range–projecting GABAergic neurons modulate inhibition in hippocampus and entorhinal cortex. *Science* **335**, 1506 (2012).
105. L. A. Cenquizca, L. W. Swanson, Spatial organization of direct hippocampal field CA1 axonal projections to the rest of the cerebral cortex. *Brain Research Reviews* **56**, 1 (2007).
106. K. M. Tye *et al.*, Amygdala circuitry mediating reversible and bidirectional control of anxiety. *Nature* **471**, 358 (2011).
107. J. J. Couey *et al.*, Recurrent inhibitory circuitry as a mechanism for grid formation. *Nat. Neurosci.* **16**, 318 (2013).
108. C. Varga, S. Y. Lee, I. Soltesz, Target-selective GABAergic control of entorhinal cortex output. *Nat. Neurosci.* **13**, 822 (2010).
109. S.-J. Zhang *et al.*, Optogenetic dissection of entorhinal-hippocampal functional connectivity. *Science* **340**, (2013).
110. E. R. Hollis *et al.*, Transient demyelination increases the efficiency of retrograde AAV transduction. *Mol Ther* **18**, 1496 (2010).
111. D. Lee, B.-J. Lin, A. K. Lee, Hippocampal place fields emerge upon single-cell manipulation of excitability during behavior. *Science* **337**, 849 (2012).

RESEARCH ARTICLE SUMMARY

# Optogenetic Dissection of Entorhinal-Hippocampal Functional Connectivity

Sheng-Jia Zhang,*† Jing Ye,* Chenglin Miao, Albert Tsao, Ignas Cerniauskas, Debora Ledergerber, May-Britt Moser, Edvard I. Moser†

READ THE FULL ARTICLE ONLINE
http://dx.doi.org/10.1126/science.1232627

Cite this article as S.-J. Zhang *et al.*, *Science* **340**, 1232627 (2013). DOI: 10.1126/science.1232627

**Introduction:** The mammalian space circuit contains several functionally specialized cell types, such as place cells in the hippocampus and grid cells, head-direction cells, and border cells in the medial entorhinal cortex (MEC). The interaction between entorhinal cell types and hippocampal place cells is poorly understood. Hippocampal place fields are thought to be generated by transformation of spatial signals from the MEC, but which cell types contribute to this process remains elusive.

**Methods:** We used a combined optogenetic-electrophysiological strategy to determine functional identity of entorhinal cells with output to place cells in the rat hippocampus. Channelrhodopsin-2 (ChR2) was expressed selectively in the hippocampus-targeting subset of entorhinal projection neurons by injecting retrogradely transportable ChR2-coding recombinant adeno-associated virus (rAAV) into the hippocampus. Hippocampus-projecting MEC cells could then be identified, after expression of ChR2 transgenes, as neurons that responded reliably, at a minimal latency, to photostimulation of either cell bodies in the MEC or axons of MEC cells in or near the hippocampus.

**Results:** Many light-responsive MEC cells were grid cells, but short-latency firing could also be induced in border cells and head-direction cells, as well as neurons with irregular firing fields or no fields at all. In each cell group, the majority of neurons discharged at minimal response latencies, suggesting that they had direct projections to the hippocampus. The same cells could also be backfired, at slightly longer latencies, by photostimulation of the cells' axons in the hippocampus. MEC cells could also be activated by photostimulation in the hippocampal CA1 subfield, but response latencies were more than 150% longer than with somatic or axonal stimulation, suggesting the activation was now synaptic.

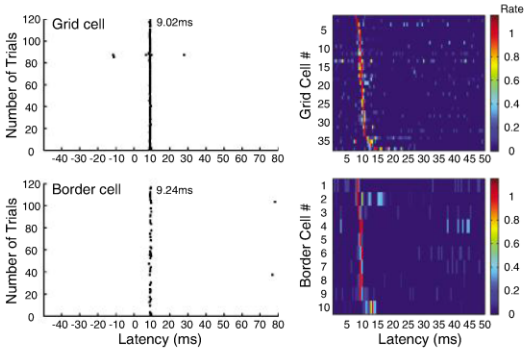


**Grid cells and border cells fire at similar latencies in response to local photostimulation. (Left)** Spike rasters showing discharge in response to successive 3.5-ms light pulses for a grid cell and a border cell. Dots indicate spike times. **(Right)** Spike rasters showing color-coded normalized firing rate 0 to 50 ms after the light pulse for all grid cells and border cells.

**Discussion:** These findings suggest that place signals are generated by convergence of signals from a variety of entorhinal functional cell types, of which grid cells are the most abundant spatial cell type. A dual spatial input from grid cells and border cells is consistent with the idea that place cells have access to both self-motion and landmark-based information and raises the possibility that the spatial metric of the place-cell population originates from grid cells, whereas boundary- and landmark-induced firing is derived directly from border cells. The dual nature of the spatial input may explain the observation that place cells precede mature grid cells during ontogenesis of the spatial representation system and that place cells can maintain location specificity under conditions that reduce grid-cell periodicity in adult rats. Convergent input from a broad spectrum of entorhinal cell types may also enable individual place cells to respond dynamically, so that different types of input are favored in different behavioral states or circumstances.

Kavli Institute for Systems Neuroscience and Centre for Neural Computation, Norwegian University of Science and Technology, Olav Kyrres gate 9, Norwegian Brain Center, 7491 Trondheim, Norway.

*These authors contributed equally to this work.

†Corresponding author. E-mail: sheng-jia.zhang@ntnu.no (S.-J.Z.); edvard.moser@ntnu.no (E.I.M.)

## FIGURES IN THE FULL-TEXT VERSION



## SUPPLEMENTARY MATERIALS

http://www.sciencemag.org/content/340/6128/1232627/suppl/DC1

Figs. S1 to S21
Full References

## RELATED ITEMS IN *SCIENCE*

**Perspective**
B. Poucet, F. Sargolini, A trace of your place. *Science* **340**, 35 (2013).
DOI: 10.1126/science.1237567